JUSTUS-LIEBIG-
UNIVERSITÄT
GIESSEN

Mass spectrometric analysis of particulate matter in remote regions and highly polluted Chinese and Iranian megacities

Cumulative Dissertation for the Degree of Doctor rerum naturalium
(Dr. rer. nat.)

prepared at the

Institute of Inorganic and Analytical Chemistry

by

Christof Barth

JUSTUS LIEBIG UNIVERSITY, GIESSEN, 2025

Table of contents

List of Abbreviations

Abbreviation	Explanation
AAS	atomic absorption spectroscopy
ALRI	acute diseases of the lower respiratory tract
AMS	aerosol mass spectrometry
AP	atmospheric pressure
BVOC	biogenic volatile organic compounds
CCN	cloud condensation nuclei
COPD	chronic obstructive pulmonary disease
DC	direct current
DE	delayed ion extraction
DNA	deoxyribonucleic acid
EC	elemental carbon
ESI	electrospray ionization
FT-ICR	Fourier-transform ion cyclotron resonance (mass spectrometer)
FWHM	full width at half maximum
GC	gas chromatography
IC	ion chromatography
ICP-(MS)	inductively coupled plasma (mass spectrometry)
IHD	ischemic heart disease
IR	infrared
IT	ion trap
IUPAC	international union of pure and applied chemistry
LAMMS	laser microprobe mass spectrometry
LAMPAS	laser mass analyzer for particles in the airborne state
LC	liquid chromatography
LDI	laser desorption/ionization
m/z	mass-to-charge-number ratio
MALDI	matrix-assisted laser desorption/ionization
MPMS	multiple particle aerosol mass spectrometry
MS	mass spectrometry
MS^2	tandem mass spectrometry
NO_x	NO and NO_2
NPF	new-particle formation
OC	organic carbon
PAH	polyaromatic hydrocarbon
PI	photoionization
PIXE	proton-induced X-ray emission
PM_{10}	particles with an aerodynamic diameter of less than 10 µm
$PM_{2.5}$	particles with an aerodynamic diameter of less than 2.5 µm

PMT	photomultiplier tube
ppb	parts-per-billion
ppm	parts-per-million
QqQ	(triple-)quadrupole (mass spectrometer)
Q-ToF	quadrupole time-of-flight (mass spectrometer)
REMPI	resonance-enhanced multiphoton ionization
RF	radio frequency
SIMS	secondary ion mass spectrometry
SOA	secondary organic aerosols
SPMS	single-particle aerosol mass spectrometry
SVOC	semi-volatile organic compounds
TEM	transmission electron microscopy
ToF	time-of-flight (mass spectrometer)
UV	ultraviolet
VOC	volatile organic compounds
VUV	vacuum ultraviolet
WHO	world health organization
XRF	X-ray fluorescence (spectroscopy)
PCA	principal component analysis
HCA	hierarchical clustering analysis
PSO	particle swarm optimization

List of Publications

The cumulative dissertation presented here describes the results of the research work within the dissertation topic in an abridged form. A detailed presentation of the results can be found in the following, already published articles:

1. Barth, C., Hinz, K.-P. & Spengler, B. On-line and off-line analysis of particles from rock, sediment, sand, snow water and atmospheric air at the Jungfraujoch site, using single-particle laser mass spectrometry. *Aerosol Science and Technology* **55,** 552–570; 10.1080/02786826.2021.1873236 (2021).

2. Barth, C., Hinz, K.-P. & Spengler, B. Particle characterization and quantification of organic and inorganic compounds from Chinese and Iranian aerosol filter samples using scanning laser desorption/ionization mass spectrometry. *Anal Bioanal Chem* **414,** 7223–7241; 10.1007/s00216-022-04275-1 (2022).

Statement in Lieu of an Oath

"I declare that I have completed this dissertation single-handedly without the unauthorized help of a second party and only with the assistance acknowledged therein. I have appropriately acknowledged and cited all text passages that are derived verbatim from or are based on the content of published work of others, and all information relating to verbal communications. I consent to the use of an anti-plagiarism software to check my thesis. I have abided by the principles of good scientific conduct laid down in the charter of the Justus Liebig University Giessen „Satzung der Justus-Liebig-Universität Gießen zur Sicherung guter wissenschaftlicher Praxis" in carrying out the investigations described in the dissertation."

_____

Date, Signature

Accepted by the Faculty 08 Biology and Chemistry of Justus Liebig University of Giessen as dissertation on 20.03.2024.

First reviewer: Prof. Dr. Bernhard Spengler

Second reviewer: Prof. Dr. Sven Heiles

Examiner: Prof. Dr. Gerd Hamscher

Examiner: Prof. Dr. Rolf-Alexander Düring

Chairman: Prof. Dr. Gerd Hamscher

Day of oral exam: 16.12.2025

Abstract

The investigations in the present work are intended to contribute to the understanding of the health and environmental impacts of aerosol pollution, both in remote regions and in strongly polluted megacities. This was achieved by a combination of different instrumental and methodological approaches. First, in-situ single-particle analysis and its evaluation, based on multivariate statistical methods, was methodologically advanced using the example of a comparative measurement of standard samples in the laboratory and of online measurements on the Jungfraujoch high altitude research station at 3580 m asl in the Swiss Alps. In order to rationalize single-particle data, weather conditions, wind speed and wind direction as well as the geographical position during the measurement were taken into account. It was found that during the field measurements at the Jungfraujoch site, Sahara desert storm events were a major source for less aged iron- and silicon-rich mineral particles. Between those events the particle population was dominated by inorganic carbonaceous compounds. Both types of particles increase the local temperature and accelerate snowmelt, either by reducing snow albedo or by absorbing light over a broad spectral range. Secondly, in order to be able to address the environmental and health related factors in greater detail, particles from two heavily polluted megacities in Hangzhou, China and Tehran, Iran were extensively characterized. Filter samples were collected and measured by high-resolution mass spectrometry imaging to assign organic hydrocarbons and more complex inorganic compounds. This enabled analysis of intact organic molecules with high mass resolution and high mass accuracy. The novel methodological approach, in which the surface of particle quartz filter samples was scanned under atmospheric pressure using a 343 nm (Yb:YAG) laser (lateral resolution about 50 µm), enabled spatially resolved determination of the molecular particle composition. More than 3200 inorganic and organic compounds were specifically assigned to individual particles based on their exact mass and location on the filter surface. Particle sources could be easily distinguished from each other by means of characteristic mass spectrometric patterns using statistical clustering methods. Standard addition methods were also used to quantify polyaromatic hydrocarbons (PAHs) on the surface of the filters. By correlating the quantitative data with the spatially resolved particle measurements, it was possible to make well-founded statements about the respective particle pollution and its causes on site. Levels of heavy metals and harmful organic compounds, primarily from anthropogenic sources, were significant in both cities. However, higher concentrations of PAHs and a greater number of heavy metal compounds were found in the samples from Tehran. Since total particle pollution in Tehran during sampling was lower than in Hangzhou, these values are extremely alarming and demonstrate the non-compliance with and the lack of air pollution control strategies in the eastern Mediterranean region. Finally, it was shown that both methods require little or no sample preparation and provide excellent results in terms of speed, accuracy and selectivity.

Zusammenfassung

Die Untersuchungen in der vorliegenden Arbeit sollen dazu beitragen, Auswirkungen der Aerosolbelastung auf Gesundheit und Umwelt, sowohl in abgelegenen Regionen als auch in stark belasteten Megastädten, besser zu verstehen. Dazu wurden unterschiedliche instrumentelle und methodische Ansätze der Aerosolanalytik genutzt und weiterentwickelt. Unter anderem wurden multivariate statistische Methoden für die In-situ-Einzelpartikelanalytik optimiert und dazu verwendet, die Quellen von Aerosolpartikeln auf der Höhenforschungsstation Jungfraujoch (3580 m ü. M.) in den Schweizer Alpen zu untersuchen. Dies erfolgte anhand einer vergleichenden Messung von bekannten Partikelpopulationen im Labor mit Online-Messungen unbekannter Aerosolpartikel auf dem Jungfraujoch. Zur Einordnung der erzeugten Einzelpartikeldaten wurden sowohl meteorologische Parameter wie Wetterbedingungen, Windgeschwindigkeit und Windrichtung als auch die geographische Lage der Messstation berücksichtigt. Die Vergleichsmessungen ermöglichten die Identifizierung von Saharawüstenstürmen als Hauptquelle für eisen- und siliziumreiche mineralische Partikel mit geringer Verweilzeit in der Atmosphäre, während der Messkampagne. Außerdem konnte gezeigt werden, dass zwischen den Wüstensturmepisoden die Partikelpopulation am Jungfraujoch von anorganischen, kohlenstoffhaltigen Verbindungen dominiert wurde. Beide Partikelarten tragen maßgeblich dazu bei, die lokale Temperatur zu erhöhen und die Schneeschmelze zu beschleunigen, entweder durch eine Verringerung der Schneealbedo oder durch die Absorption von Licht in einem breiten Spektralbereich. Weiterhin wurden im Rahmen der vorliegenden Arbeit Partikel aus zwei stark verschmutzten Megastädten, Hangzhou (China) und Teheran (Iran), umfangreich charakterisiert. Ziel dabei war es, die umwelt- und gesundheitsrelevanten Faktoren der Partikelbelastung genauer zu untersuchen. Auf Filtern gesammelte Partikel aus beiden Städten wurden mittels hochauflösender, bildgebender Massenspektrometrie untersucht, um organische Kohlenwasserstoffe sowie komplexe anorganische Verbindungen mit hoher Massenauflösung und hoher Massengenauigkeit zu identifizieren. Das Abrastern der Filterproben mittels 343-nm-(Yb:YAG)-Laser (laterale Auflösung ca. 50 µm) unter Atmosphärendruck, ermöglichte eine räumlich aufgelöste Bestimmung der molekularen Partikelzusammensetzung. So konnten im Rahmen der Studie mehr als 3.200 anorganische und organische Verbindungen anhand ihrer genauen Masse und Position auf der Filteroberfläche, spezifisch einzelnen Partikeln zugeordnet werden. Die Identifikation der Partikelquellen erfolgte zudem anhand charakteristischer, massenspektrometrischer Muster und unter Zuhilfenahme statistischer Clusteranalysen. Des Weiteren wurden polyzyklische aromatische Kohlenwasserstoffe (PAK) auf der Filteroberfläche mittels Standardaddition quantifiziert. Durch die Korrelation der quantitativen Daten mit den räumlich aufgelösten Partikelmessungen, konnten fundierte Aussagen über die jeweilige Partikelbelastung und deren Ursachen vor Ort getroffen werden. Die Belastung mit Schwermetallen und organischen Verbindungen, insbesondere solche anthropogenen Ursprungs, war in beiden Städten signifikant. Jedoch wiesen die Proben aus Teheran höhere Konzentrationen an PAK sowie eine höhere Anzahl an Schwermetallverbindungen auf. Da die Gesamtpartikelbelastung in Teheran während der Probenahme geringer war als in Hangzhou, sind diese Werte äußerst alarmierend und deuten auf die Nichteinhaltung oder das Fehlen von Strategien zur Luftreinhaltung in der östlichen Mittelmeerregion hin. Zusammenfassend konnte gezeigt werden, dass beide Methoden wenig oder gar keine Probenvorbereitung erfordern und exzellente Ergebnisse in Bezug auf Geschwindigkeit, Genauigkeit und Selektivität liefern.

1 Synopsis

1.1 Introduction and Motivation

Aerosols are ubiquitous in our environment. By definition of the International Union of Pure and Applied Chemistry (IUPAC), an aerosol consists of finely dispersed solids or liquids or a mixture of both suspended in air.[1] Aerosol particles can be few nanometers in diameter only or can grow up to several micrometers. They are of particular interest with regard to their influence on the global climate, atmospheric visibility, ozone depletion, toxicity, or, as SARS-CoV-2 made particularly clear, as carriers of diseases.[2–7] The main components of aerosol particles are inorganic water-soluble compounds (sulfates, nitrates, ammonium, sea salt), black carbon (BC), organic carbon (OC), mineral dust and water.[3,8] Estimates show that the share of aerosol components associated with negative health effects (BC, OC, sulfate and nitrate) and global warming (BC) will increase significantly by the year 2030, if no changes are adopted to current legislations on emissions.[3] For example BC, and SO_2 as precursor of sulfate aerosol will rise by 10 and 29% respectively, while the main emission factor for SO_2 is industrial combustion, the major share of BC is emitted by domestic combustion.[9] Air pollution is considered the biggest risk factor for human health worldwide. The World Health Organization (WHO) estimates that about 3 million deaths in 2012 are due to polluted air.[10] While elevated concentrations of atmospheric gases such as NO plus NO_2 (NO_x), ozone, CO and SO_2 contribute to increased mortality and global warming, particulate phase pollutants like sulfate, particulate organic matter and mineral dust are more likely associated with global cooling.[3]

If air quality is assessed based on particulate matter (PM), the most common measure to assess the concentration of particles in the gas-phase is the $PM_{2.5}$ value, i.e., number of particles with an aerodynamic diameter of less than 2.5 µm.[11] Particles of this diameter are usually alveolar and are also known as fine dust. They penetrate deep into the human lung, settle there and may cause ischemic heart disease (IHD), strokes, lung cancer, chronic obstructive pulmonary disease (COPD) and acute diseases of the lower respiratory tract (ALRI).[10] However, the danger of the particles does not only depend on their size, but above all on their chemical composition and the associated acute and long-term toxicity, as well as their pro-inflammatory effect.[12] In particular, contamination by heavy metals such as lead, cadmium and chromium as well as by arsenic and polyaromatic hydrocarbons (PAHs) is of major concern.[6,13] A large number of harmful particles are of anthropogenic origin and therefore occur more frequently in heavily populated areas.[14] Often, however, atmospheric transport of such particles leads to their worldwide distribution, even to the most remote regions of the earth, such as the Arctic or the primeval forests of the Amazon.[15,16] Conversely, it has been shown that rising population, urbanization and increasing demands on technology and prosperity are accompanied by an increase in exposure to harmful particles, predominately black carbon, sulfates and nitrates.[17] The reduction of visibility can be observed in this context as well. For example, in India, where in regions with more than 100 persons per km^2, an increase in population of 1.5% per year is accompanied by approximately 2% increase in aerosol optical thickness.

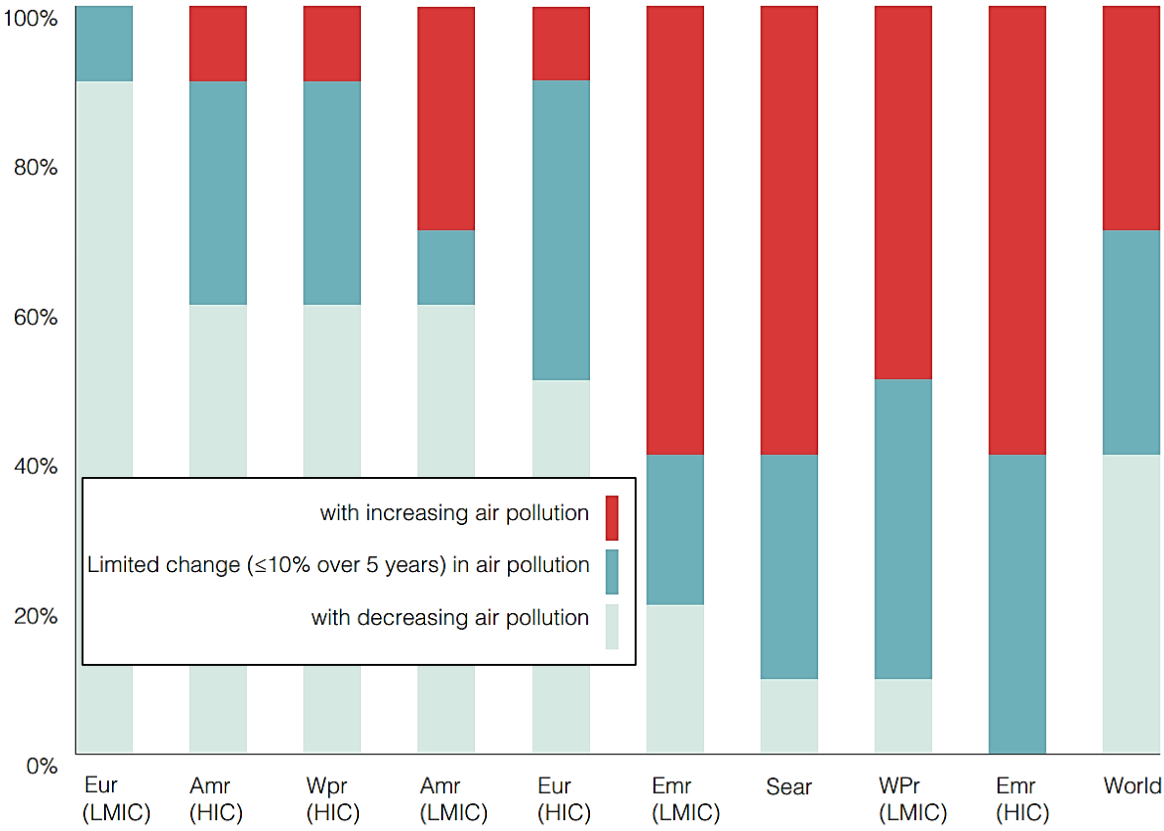

Region	*Trend over the mean period 2008-2013*
Africa (Sub-Saharan)	NA
America (LMIC)	→
America (HIC)	↘
Eastern Mediterranean (LMIC)	↗
Eastern Mediterranean (HIC)	↗
Europe (LMIC)	↘
Europe (HIC)	↘
South-East Asia	↗
Western Pacific (LMIC)	↗
Western Pacific (HIC)	↘
Global	↗

Figure 1: Trends of air pollution in different regions of the earth from 2008 to 2019. The figure at the top shows the proportion of countries in a particular region of the world in which air pollution is either increasing (red), barely changing (light blue) or decreasing (light green). Trends for each region show that drastic increase in air pollution was observed particularly for eastern Mediterranean and Asian countries.[10]

In this respect the situation has changed considerably since the 1950s.[18] Whereas Central Europe and the Americas were the main sources of these emissions at that time, the balance has shifted toward the rapidly growing industrialized nations in Southeast Asia and some eastern Mediterranean countries.[10] In both regions, strong growth, driven by industrial upturn, is contributing to a tendency for increased air

pollution, while in Europe, America and the Western Pacific countries a decrease in air pollution can be observed, as shown in Figure 1. Particularly in the eastern Mediterranean area and East Asia, a lack of governmental regulations to reduce air pollution or their non-compliance, is typically the cause.

In addition to understanding the composition of particles in heavily polluted regions of the earth and their mostly anthropogenic sources, it is important to understand how particles are distributed globally and which changes they undergo in the atmosphere. Both factors influence local climate conditions and serve as a basis for global climate modelling. For this purpose, studies in remote regions are of particular relevance, since the smaller number of particles and greater distance to anthropogenic sources allow more differentiated and detailed information about transport routes and atmospheric factors. In both cases, however, regarding particle pollution in remote regions as well as in densely populated metropolitan areas, the origin of the particles, their chemical composition and the changes they undergo during transport in the atmosphere have not yet been sufficiently clarified. This, however, is indispensable for assessing the influence of aerosol particles on climate and health.

The aim of this work was to develop mass spectrometric workflows that facilitate extensive characterization of particulate-matter pollution by uncomplicated and broadband methods. With the help of these methods, the chemical properties of aerosols, especially of single particles, were investigated to the greatest-possible detail. This included both the quantitative elemental and molecular, as well as the qualitative composition of the particles. Based on this information, details of formation and distribution, as well as atmospheric aging and the resulting effects on climate, environment and health, were inferred employing meteorological data and authentic standard particles. The obtained data will serve as a starting point for the calculation of climate models, whose initial parameters are mainly based on the knowledge of light absorption, light scattering, volume concentration, and size distribution of particles. Furthermore, hygroscopic properties of particles are important, as they have a major influence on cloud formation and thus have a secondary impact on the climate. A variety of analytical measurements are used to fill these gaps in our knowledge about the origin and chemical aging of particles under the influence of oxidative substances such as ozone or OH radicals, gaseous reactants such as CO, NO_2 or SO_2, or semi-volatile organic compounds.

Some highly relevant questions, however, have so far remained mostly unanswered in this context, for example regarding the influence of distant and regional natural particle sources, particularly of mineral particles in remote regions. This includes in particular the classification of atmospheric particles into fresh and aged, and the influence of this chemical processing on local climatic conditions. This is highly significant, especially regarding the reduction of backscattering of sunlight in snow-covered regions, such as the peaks of the Alps by insoluble mineral compounds, which is known to accelerate snow-melt dramatically. Beyond this, the pollution of megacities by harmful particles continues to be in the focus of public attention. In many of the world's fast-growing industrialized nations, immense efforts have already been made to reduce emissions of harmful particulate matter. Nevertheless, these positive changes are not universally applicable, nor are they occurring to the same degree in all regions. This is especially evident in the eastern Mediterranean region. Comparisons of densely populated areas in this region with highly polluted megacities in China, for example, are lacking. Detailed knowledge about the composition of very complex inorganic and organic aerosol particles in such highly populated areas is needed on the molecular level. Until now, only few efforts were made to unravel the risk of these particles, with minimal sample preparation and measurement effort at the same time. Both questions are of great scientific interest and are addressed in this thesis. By combining instrumental and methodological developments, the aim was to simplify the measurement, evaluation and interpretation of the data and to extend their information content.

1.2 Thematic and instrumental background

1.2.1 Mass spectrometry

Mass spectrometry (MS) is a method to determine the mass or more accurately the mass-to-charge-number ratio (*m*/*z*) of an ion. After the fundamental discovery of canal rays and investigation of their properties by Wilhelm Wien, the principle of MS was developed by J. J. Thomson in the early 20th century.[19–21] In this early days it was primary used in physics to study the fundamentals of small positively charged ions and to separate isotopes of certain elements.[22,23] MS became commercially available in the 1940s, where it was mainly used for analyzing complex oil mixtures.[24] MS has been developed in great strides since the 1950s and thanks to the work of Fred McLafferty, Klaus Biemann, and Carl Djerassi, the technique attracted the attention of the chemical community for the elucidation of structures of complex organic molecules.[25–29] This laid the foundations for modern MS, especially in the fields of environmental analysis, biochemical analysis and medical analysis.[30] Already in the 1950s, the detection of analyte quantities in the range of a few micrograms or significantly less was common.[31–33]

The instrumental procedure of such a measurement is always similar. First, the components of the analyte to be measured, whether organic or inorganic, must be converted into ions and transferred into the gas phase. This can either be done under atmospheric pressure (AP), after which the ions are transferred into vacuum via a suitable interface, or they can be generated in vacuum directly.[34–36] The most common methods to generate ions are based on the use of electrons, ions, photons, energetically excited atoms or even electrostatically charged droplets.[23,35,37–39] The latter one, better known as electrospray ionization (ESI), has had such a major impact on the analysis of intact, large biomolecules since its invention in 1989 that its inventor John B. Fenn was awarded the Nobel Prize in 2002.[35] Ionization of gas phase molecules using photons, referred to as photoionization (PI) and of solid and liquid substances by laser desorption/ionization (LDI) is also widely used and paved the way for the invention of another method found to be highly suitable for the analysis of large, intact biomolecules using organic matrices. This ionization method is now known as matrix-assisted laser desorption/ionization (MALDI).[40] After ion generation, transfer of ions into the mass analyzer occurs in which *m*/*z* values are determined.

Determining m/z values is realized by separating the ions from each other, typically by means of static or dynamic electric or magnetic fields as with magnetic sector analyzers, quadrupole mass analyzers or ion traps (IT). An exception is time-of-flight (ToF) mass spectrometry, in which the ions are accelerated in an electric field and then separated from each other while crossing a field-free flight path.[41] Historically, the first mass spectrometers were based on sector field analyzers. These accelerate the ions in an electric field, whereupon they enter a magnetic field arranged perpendicular to their direction of motion, all with the same kinetic energy. In accordance with the Lorentz force, the ions are deflected and, based on their *m*/*z*-ratio, are steered onto circular paths of different size (high mass = large radius). Thomson already used this geometry to investigate his cathode rays, which was then further improved by Dempster in 1918 leading to the invention of the first modern mass spectrometer.[23] Magnetic sector instruments are still used today, usually as double-focusing instruments and are valued for their high dynamic range and good resolution, especially in the field of isotope analysis.[22,42,43] Linear quadrupole analyzers operate as mass filters, meaning that only selected *m*/*z*-ratios can travel on stable trajectories through the device. For this purpose, the accelerated ions pass through an arrangement of four parallel rod electrodes in which the opposite electrodes are always at the same potential. A high-frequency alternating field is applied between neighboring electrodes, superimposed by a DC offset. By varying the voltage amplitude, only ions of certain *m*/*z*-values are on stable paths through the electrodes, which are described by Mathieu's differential equation, while the remainder are lost through collisions with the

rods.[44] Trapping of ions within coaxial cylinders by electric or magnetic fields was theoretically proposed by F. M. Penning in 1936 and implemented by Wolfgang Paul in 1953.[45,46] Ion separation occurs through excitation of the trapped ions via changes in the electric fields, which can either be used to force them onto circular trajectories whose frequency depends on their *m*/*z*-ratios, or selectively eject them from the trap.

Finally, the separated ions are quantitatively detected (signal intensity ~ number of ions), either by direct impact on a detector, for example on electron multipliers or indirectly by measuring the amplitude and frequency of oscillating ions.[47–49] The detection method used strongly depends on the analyzer for mass separation. Finally, the signal is transmitted to a data acquisition system and plotted as a two-dimensional diagram. The ordinate corresponds to the intensity of the recorded signal and is proportional to the number of detected ions, whereas the abscissa is represented by *m*/*z*, where *z* is equivalent to the charge state (or charge number) of an ion. The generated ions may well assume charge states > 1, depending on the ionization method used, but singly charged ions are common. The mass *m* can be defined as a multiple of the unified atomic mass unit u, which is 1/12 of the mass of an atom of the carbon isotope ^{12}C.[50]

An important requirement for the detection and separation of ions in a mass spectrometer is the presence of a vacuum to increase the mean free path, which can be described as the average distance that a particle can travel between two successive collisions with other particles.[51] In case of MS, this avoids collisions between the ions to be measured and neutral particles, which conversely increases the mass resolution (*R*) of a mass spectrometer and its limit of detection, since less ions get lost during analysis. Mass resolution is a dimensionless value, which describes, at a given *m*/*z* value, the smallest difference in *m*/*z* (Δ *(m/z)*) that can still be resolved. This definition is often extended to so-called mass resolving power at different criteria, for example to separate two neighboring signals at 10% or 50% of their maximum height (10% or 50% valley definition).[52] The two signals are separated, if the valley between both is maximum 10% or 50% of the intensity of the smallest signal as shown by

$$R_{10\%} = \frac{m/z}{\Delta(m_{10\%}/z)}. \quad (1)$$

The so-called full width at half maximum (*FWHM*) criterion is often used for ToF or linear quadrupole mass analyzers to describe the peak width at a given *m*/*z* value, which does not necessarily mean that two signals can be separated at this value.

In addition to *R*, which relies mainly on the performance of the mass analyzer, lower limit of detection (often wrongly referred to as „sensitivity“) and mass accuracy are also important for the characterization of a mass spectrometer. The lower limit of detection provides information about the minimum quantity of a substance that can be detected by the system. The lower limit of detection is influenced particularly by the ionization efficiency, the extraction of ions from the ion source (ion transmission), the sensitivity of the detector and the mass range to be measured.[53–55] When it comes to the identification of the measured ion, the most important factor is mass accuracy, which in the case of high mass accuracy, can deliver the molecular formula for a certain *m*/*z* signal up to a certain *m*/*z* limit. This absolute mass accuracy Δ(*m*/*z)* is defined as the difference between the measured mass (accurate mass) and the calculated exact mass (theoretical mass) and has the unit u.[56] Typically, the mass accuracy is given as a relative value in parts-per-million (ppm), which can be derived by dividing the absolute mass accuracy Δ(*m*/*z)* by *m*/*z* of the exact mass.

Due to the intrinsic mass defect of each atom, *m*/*z* values for each molecular formula are well defined. They can be calculated and given in the form of the exact mass of a molecule. The higher the mass

accuracy of a mass spectrometer, the higher is the confidence with which the atomic composition of an ion can be determined from the measured value.[57] However, with increasing *m*/*z*, the number of atoms in an ion also increases, and thus the number of different possible compositions within the measured mass accuracy. This makes it very difficult to confidently assign molecular formulas for larger *m*/*z* (> 500), even if the mass accuracy is in the range of ±1 ppm or lower, which is a typical value for modern ultra-high resolution instruments.[58]

Modern mass spectrometers benefit from a whole range of different mass analyzers, each of them with their own advantages and disadvantages. For example, orbital trapping and Fourier-transform ion cyclotron resonance (FT-ICR) analyzers allow the measurement of high molecular weight and very complex molecules with ultra-high resolutions (R > 500,000 at m/z 200), and therefore the identification of intact proteins and their fragments on the basis of their calculated exact masses.[47,59] These instruments are usually very expensive and the time of measurement scales with performance, leading to poorly resolved mass spectra at high measurement frequencies. Commonly used systems for routine applications are ion trap and (triple-)quadrupole (QqQ) devices due to their good price-performance ratio, but they typically suffer from limited mass resolution and medium scan rates.[45,60] One of the most widely used types of mass analyzers are ToF systems, either in linear arrangement, with ion reflector design, or as a combination of quadrupole mass filter and ToF analyzer (Q-ToF).[41] ToF analyzers offer resolutions up to R = 50000 at acceptable costs. Other, even more important advantages are the rather simple construction, high scan rates, their high ion transmission and a theoretically unlimited mass range.[61,62] Due to the simple design, this analyzer type is especially suitable for use in self-built systems, particularly when only low amounts of sample are available and the measurements should be fast.[63]

ToF mass spectrometry

The principle of ToF mass spectrometry as shown in Figure 2 is based on the fact that ions are accelerated within a homogenous electric field E_a, typically applied between a backing plate and an acceleration grid and acquire a defined amount of electrical energy E=qU.[64] As E_a depends on the distance and the voltage between two electric charges in the electric field, which is the distance x_a between the ions and the charged grid, it can be written as $U = x_a E_a$. In theory each ion acquires the same kinetic energy, based on the electric field strength in the acceleration region and starts at the same position in space (x = 0).

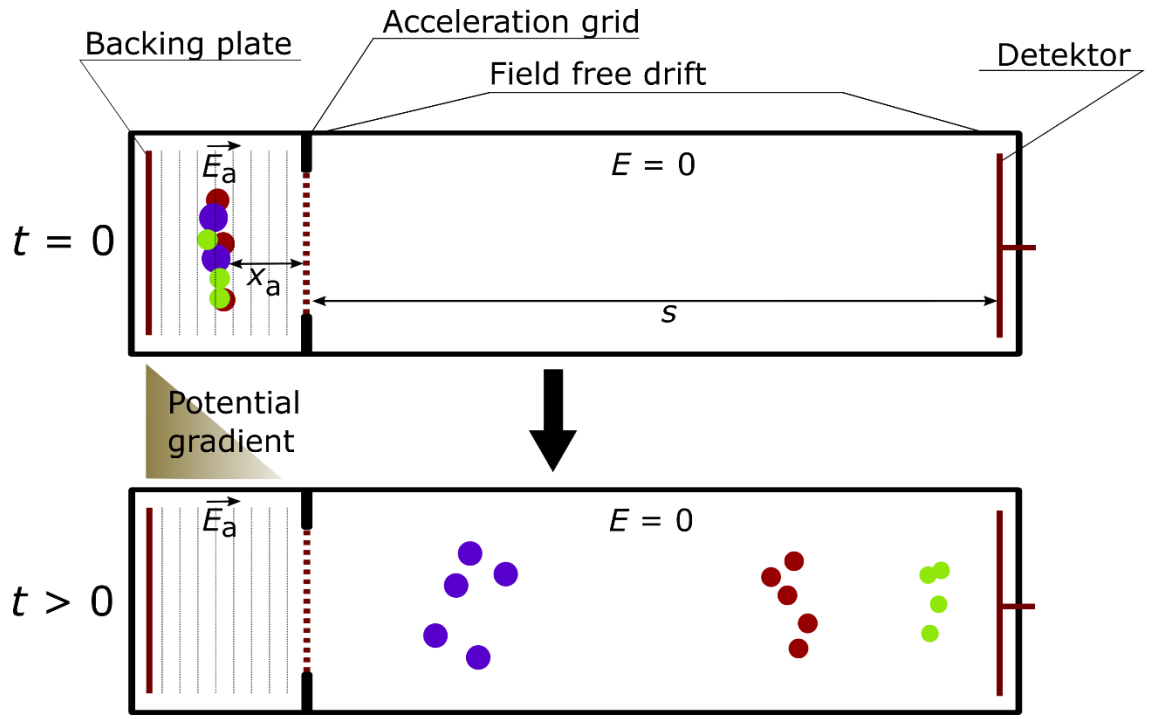

Figure 2: Principle of ToF mass spectrometry for two timepoints *t* = 0 and *t* > 0. Example shows ions with three different *m*/*z* values (green < red < violet).

While entering the field-free drift region, discrete packages of ions are separated from each other based on their *m*/*z*-ratio as the velocity *v* of each ion is constant during its movement along the drift path *s* (*t* > 0). The kinetic energy E_{kin} of an ion is

$$E_{kin} = \frac{1}{2}mv^2 = \mathrm{q}U = \mathrm{q}x_a E_a, \tag{2}$$

and with drift time $t_{drift} = s/v$, an m/z-dependent expression is deduced:

$$t_{drift} = s\sqrt{\frac{m}{2zeU}}. \tag{3}$$

To determine the total flight time *t* of an ion, an additional factor must be included, which results from the residence time of the ion in the acceleration field t_{acc}.[64] The acceleration *b* is constant here, with $b = \mathrm{q}E_a/m$, while velocity increases until t_{acc}. Integrating velocity over time for distance x_a results in

$$x_a = \frac{1}{2}bt_{acc}^2 = \frac{1}{2}\frac{\mathrm{ze}E_a t_{acc}^2}{m}. \tag{4}$$

Rearranging Eq. (4) gives

$$t_{acc} = \sqrt{\frac{2x_a m}{\mathrm{ze}E_a}}, \tag{5}$$

and finally the total flight time

$$t = t_{acc} + t_{drift}. \tag{6}$$

The maximum time spread Δt between the first and last ion within a package of ions with identical *m*/*z* values defines the resolving power of the ToF mass spectrometer, which can be expressed by[65]

$$R = \frac{m}{\Delta m} = \frac{t}{2\Delta t}. \quad (7)$$

Final goal of ion acceleration and drift time is to produce ion packages as narrow in time as possible, which are well separated from each other. Optimizing mass spectrometric conditions to achieve high resolving powers for ToF instruments typically include space- and energy-focusing which can be achieved by two-stage ion acceleration, orthogonal acceleration, reflector geometry and time-lag focusing (delayed ion extraction).[65–68] As energy and space focusing need opposite requirements on the design of a ToF MS, making it hard to reconcile both, a compromise between different techniques seems to offer optimal conditions for high resolving power. The concept of such an improved ToF MS, introducing two of the above mentioned techniques, was invented by W. C. Wiley and I. H. McLaren in 1955.[66] They used two-stage acceleration to reduce spatial ion spread Δt within a package of isobaric ions and therefore increases space resolution, while a time-lag between ionization and extraction causes a relaxation of the initial kinetic energy.

Two-stage acceleration is particularly important in dual-polarity ToF mass spectrometry (described in detail in section 1.2.4), as the ions are formed from a single particle in free space, allowing them to fly into opposite directions, resulting in dramatically different starting points and thus space distribution s_0. The use of single-stage ion acceleration instead means that ions located close to the first accelerating grid experience a weaker force than those located further away. The reason for this is the change in the potential energy of an ion with the change in the distance to the charged grid, which increases with increasing distance. Ions further away from the field-free drift region are thus accelerated to a higher kinetic energy and overtake the slower ions shortly after entering the field-free drift region. Typically, the detector is positioned in such a way that it is in the plane (first order space focus) where the two ions just overtake each other and thus have the smallest spatial distance to each other (low Δt). There are two possibilities to achive space focusing, either by reducing the initial distance between the ions Δs, which is very difficult to control, or by generating an ion velocity that is dependent on s. The latter is achieved by the two-stage design. An extraction field E_s at the beginning brings the ions closer to each other, after which they are brought to their final energy in the second stage with electric field E_d, the actual acceleration region. This greatly extends the distance until the rear ion overtakes the front one (second order space focus), the time-of-flight is increased, as well as the compactness of the ion package and thus the mass resolution. The final energy of the ions is reached typically within 5 % of their flight-time compared to about 50 % for single-stage sources.[66] The space resolution R_s can be obtained from:

$$R_s \approx 16 k_0 (s_0/\Delta s)^2, \quad (8)$$

with k_0 depending on the electric fields in the first and second stage of the ion source and distance d between the first and second acceleration grid

$$k_0 = (s_0 E_s + d E_d)/s_0 E_s. \quad (9)$$

The initial kinetic energy ($E_{kin,0}$) spread of ions is best illustrated by two ions with the same starting point but moving in opposite directions. Both acquire the same acceleration energy in the ionization region due to the applied fields, but the second ion, which is not moving towards the detector must first be decelerated, turned around and accelerated again until it has the same direction and energy as the first ion. This so-called turn-around time is a representative for the spread of initial velocities of the ions and can be compensated by a short time lag between ion formation and ion extraction. This time lag (field free time), typically in the range of 100 ns, allows the second ion to travel in the direction of a higher potential energy surface, while the first ion increases the distance to this surface. After switching on the

acceleration voltage both ions are accelerated towards the detector at the same time. The ion that traveled in direction of the surface with higher potential energy will gain more energy than the one traveling in the direction of the detector, thus allowing to compensate the turn-around time.[66] The energy resolution R_E is given by

$$R_E = \frac{1}{4}\sqrt{\left(\frac{E_{kin,t}}{E_{kin,0}}\right)}\left(\frac{k_0+1}{\sqrt{k_0}} - \frac{\sqrt{k_0}-1}{k_0+\sqrt{k_0}}\frac{d}{s_0}\right) \tag{10}$$

with ion kinetic energy $E_{kin,t}$ defined as

$$E_{kin,t} = qs_0E_s + qdE_d. \tag{11}$$

The total time spread R_{tot} resulting from energy and space distribution is therefore

$$\frac{1}{R_{tot}} = \frac{1}{R_s} + \frac{1}{R_E}. \tag{12}$$

As the resolution R in a ToF instrument is directly proportional to the flight time t of an ion by Eq. (7), it is a mandatory requirement to increase the field-free flight path for high R. In order to keep the dimensions of such devices as small as possible, ion reflectors are used for each polarity, which approximately doubles the distance of field free movement of ion packages. Additionally, the ion reflectors compensate for initial kinetic energy spread within isobaric ions. The electric field of the reflector is opposite to the acceleration field, which slows down and reverses the movement of the ions. Ions with higher kinetic energy penetrate deeper into the reflector, thus covering a longer distance to the detector. Finally, all ions of the same m/z arrive at the detector with a very small time spread.

By combining orthogonal and two-stage acceleration with multi-reflector geometries, instruments can reach mass resolving powers up to 80,000 *FWHM* (at m/z > 800).[69] Short duty cycles and short measurement times, mainly depending on mass range and ion mass allow data acquisition rates of up to 2 kHz.[61]

Orbital trapping mass spectrometry

While ToF MS is well suited for fast and sensitive measurements but suffers from low mass resolution, orbital trapping devices show their particular strength in this context. The principle of orbital trapping mass spectrometry was reported in the early 1920`s by K. H. Kingdon. The so called Kingdon trap was based on ions that circle around a thin central filament.[70] This idea was adopted by A. Makarov, who published the first working prototype of an orbitrap mass analyzer in 2000.[59] Apart from the first idea of Kingdon using a filament, Makarov developed a cylindrical design of inner and outer electrode with a static voltage between both, resulting in a quadrologarithmic electrostatic field. Ions are injected into the trap perpendicular to the axis of the inner spindle-like electrode and slightly off-center as shown in Figure 3.

The potential distribution in the trap leads to a combination of ion movement around and along this axis, which can be described as a spiral trajectory. The ion motion along the z-axis is independent of perpendicular motions along the plane, which strongly depends on initial spatial and kinetic energy spread of the ions. In Makarovs design the mass-to-charge ratio m/q is obtained via Fourier transformation of time-resolved image currents on split outer electrodes, induced by harmonic oscillation of ions.[71]

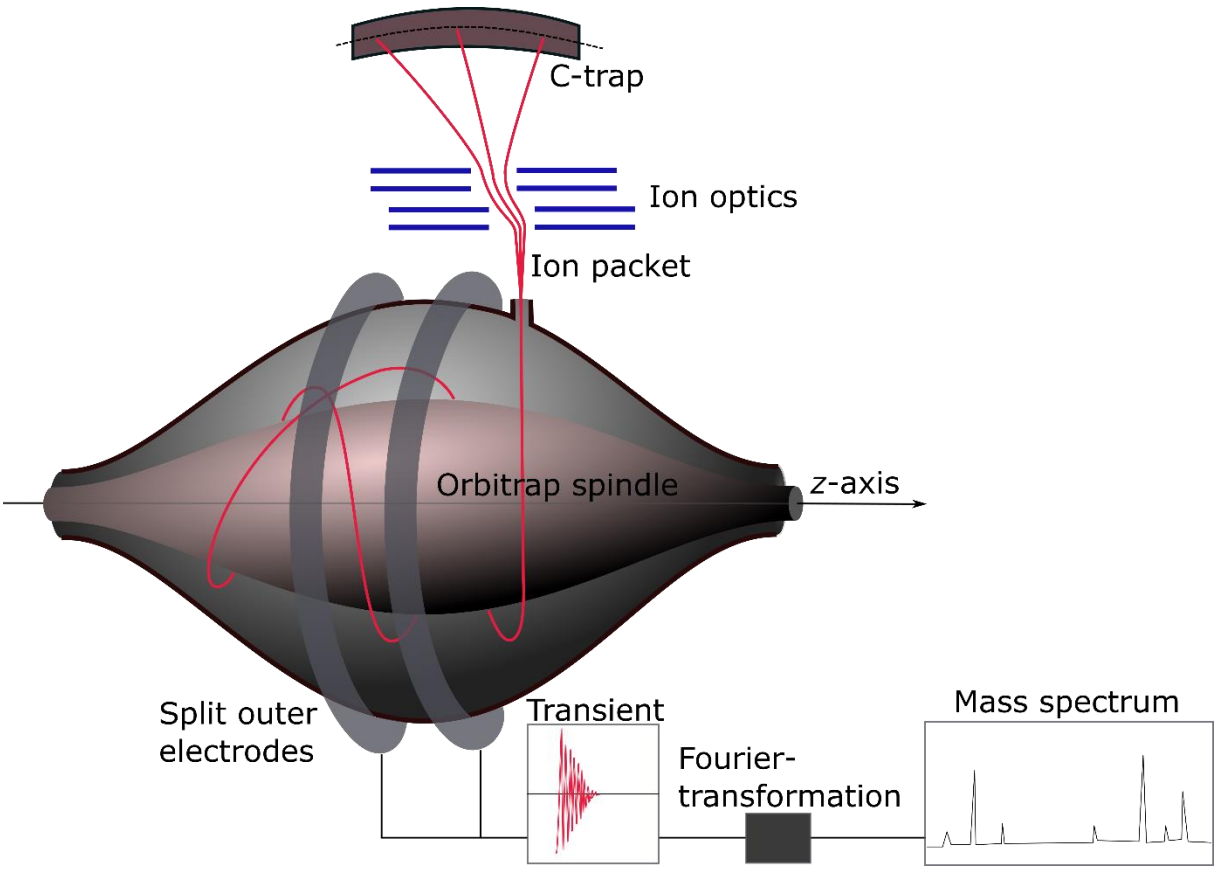

Figure 3: Schematic of an orbital trapping mass analyzer, with ion injection through C-trap and signal processing.[59]

The axial oscillation frequency ω (rad/s) of an ion, as shown in Eq. (13) only depends on the axial restoring force *k*, which describes the exact form of the electrodes and applied potentials.[59]

$$\omega = \sqrt{\frac{qk}{m}} \tag{13}$$

Calibration of measured frequencies with ions of known *m*/*z*-ratios translates the frequency values into *m*/*z* values. With orbitrap mass analyzers, high mass resolving power (> 100,000 at *m*/*z* 200), high mass accuracy (< 1 ppm) and a wide dynamic range is realized, without the need for high magnetic fields.[72] In 2005, Thermo Fisher Scientific commercially introduced the orbitrap mass analyzer with their hybrid LTQ Orbitrap™ instrument.[73] Mass resolving power exceeding 1,000,000 has been shown for a minimized high-electric field orbitrap at a transient detection time of 3 seconds.[74] Mass resolving power is mainly limited by the number of passages of ions close to the detector electrodes and thus the length of the transient or the oscillation frequency. A prerequisite for stable trajectories, and a major hurdle at the beginning of the development was the controlled injection of ions into the trap. By developing a curved, linear quadrupole ion trap outside the orbitrap, the so-called C-trap, the ions can be injected as small packets with low space-charge effects and minimized axial location distribution.[75] After collecting a certain number of ions in the C-trap, they are tangentially fed into the orbitrap by switching off the trapping RF followed by a DC gradient across the C-trap. This allowed the use of discontinuous ion sources, and led to increased mass resolution, mass accuracy and limit of detection. Real time lock mass calibration of background ions in the C-trap further increased mass accuracy to less than 1 ppm.[76]

For the work presented here, two major mass spectrometric setups were employed. One is based on LDI, which was used for the ionization of small atmospheric particles in bipolar ToF MS. This method and

the instrument used are further described in section 1.2.4. A second approach relied on rasterizing a nearly flat surface, covered with small atmospheric particles by LDI under atmospheric pressure and subsequent measurement of the generated ions by a high-resolution orbital trapping mass spectrometer, which is shown in detail in section 1.2.5.

1.2.2 Chemical properties of aerosol particles and their sources

The overall subject of this work and thus the samples to be studied are aerosol particles, whether of natural origin or anthropogenic. Aerosol particles typically consist of a wide variety of components, either inorganic or organic, from natural origin or anthropogenic sources. Any object can be classified as an aerosol particle, assuming it is pulverized or dispersed finely enough and fits in the size range between few nanometers up to 100 µm. Typically, the quantity of particles is classified by the particle number concentration or particle density, meaning their number per volume of air in $1/cm^3$. In global scales, the particle number concentrations vary strongly between rural and urban areas as well as between different layers of air. Mean concentrations are 300 – 3,000 particles/cm^3 in the marine boundary layer and free troposphere, while they can easily reach 1,000 – 10,000 particles/cm^3 in the continental boundary layer.[77] This variety complicates classification and description of aerosol particles, hence only the most important constituents and sources are considered in this chapter. Particle classes such as animal tissue and excrements[78], polysaccharides and proteins[79], cement[80] and metal particles from industrial processes or abrasion[81] are important as well but are not described here. Particles are typically grouped based on the origin of particle production. Primary particles are emitted directly from natural or anthropogenic sources, whereas secondary particles are formed from gaseous precursors in the atmosphere.

Large aerosol particles above 2.5 µm (coarse-mode particles) are primary particles, which are usually created by mechanical processes, i.e., erosion, abrasion, volcanic eruptions, wind turbulences and biomass burning.[82,83] Well-known types of particles in this category include mineral dust, sea salt, pollen, tire abrasion and coarse fly ash. Herein, sea salt aerosols and eroded dust particles are the quantitatively most important representatives on a global scale. They account to the total particle emissions with 6273 Tg/yr (2002/2003) and 1678 Tg/yr (2000), respectively.[84,85] The coarse mode particles also include purely biological material, such as bacteria, viruses, and fungal spores. Often, fungal spores receive little attention, but account for up to 23% of the primary organic aerosol.[86] The quantitatively most important sources of anthropogenic primary aerosol particles are traffic, combustion plants for energy production, heavy industry and combustion of biogenic material in the household sector (cooking and heating).[87,88] The residence time of these particles in the atmosphere is short (minutes to few hours) compared to particles below 2.5 µm size, as their sedimentation to the ground occurs quickly due to their high mass density.[83]

Smaller particles below 2.5 µm (fine-mode particles) emerge mainly from gas-to-particle conversion processes. The most important precursors are inorganic trace gases such as NO_x, NH_3 and SO_2, volatile organic compounds (VOC) and semi-volatile organic compounds (SVOC).[89–92] While the reactive inorganic trace gases are mainly of anthropogenic origin, e.g., industrial combustion plants for energy production, large-scale chemical industry, as well as shipping, aviation and road traffic, the majority of VOCs, such as terpenes and isoprenes, originate from natural sources. These biogenic volatile organic compounds (BVOC) are mainly emitted by coniferous forests and, at about 1007 Tg/yr in 2000, are significantly above the global emission of anthropogenic SO_2 with 103.3 Tg/yr in 2014.[93,94] Particles between 0.1 and 2.5 µm primarily result from condensation of the gaseous precursors on already existing particles, such as nanometer-sized carbon particles from combustion processes (black carbon), or from coagulation of ultrafine precursors. They have a much longer half-life compared to particle fractions

below and above this size range. Residence times of several weeks in the atmosphere enable them to travel several thousands of kilometers, hence they are called accumulation mode particles. Such particles are usually washed out of the atmosphere by rain or snow, or eliminated by impaction and sedimentation.[83]

Ultrafine particles are smaller than 0.1 µm in diameter. Due to their appearance during the initial formation of new particles (NPF), they received a lot of attention and are often the subject of current research.[95–97] This size range is also known as nucleation mode, since the particles are formed by nucleation of single molecules, clusters and macromolecules, rather than condensation of fine droplets. One well-known example of this process is the oxidation of SO_2 to H_2SO_4 and reaction with ammonia to form very small precursor particles by nucleation, which is followed by coagulation of the tiny clusters to larger particles.[98,99] The lifetime of these particles is typically short compared to particles in the size range between 0.1 and 2.5 µm as they quickly coagulate to bigger particles or condensate on existing ones. Nucleation mode particles emerge mainly at higher altitude in the planetary boundary layer (lower troposphere) and are also the most relevant factor for cloud formation and thus influence the earth`s climate and energy balance.[95,100] Model calculations assume that secondary ultrafine particles account for about 45% of the global cloud condensation nuclei (CCN), indirectly contributing to global cooling, while the remaining 55% contain primary particles.[101,102] It is now known that particles in the nucleation mode are formed not only by inorganic acid clusters, but also by organic acids resulting from the photooxidation and hydroxyl radical oxidation of terpenes and isoprenes. These organic acids can either increase the formation rates of inorganic acid clusters or generate particles on their own.[91,103–105] Chemically modified organic precursors are referred to as secondary organic aerosols (SOA). Observations of nucleation mode particles in the size range of few nanometers was mainly limited to existing technologies, which can precisely detect such small particles, as well as measure their size and number concentration.[99,106] A large partition of ultrafine particles also arises from combustion processes, whether anthropogenic or natural. Interestingly, the major sources of anthropogenic primary particles, which are dominated by ultrafine particle emissions by about 80%, differ between countries and continents. For example, road traffic is the most important factor in Europe, while emissions in China and India are dominated by industrial combustion processes.[107]

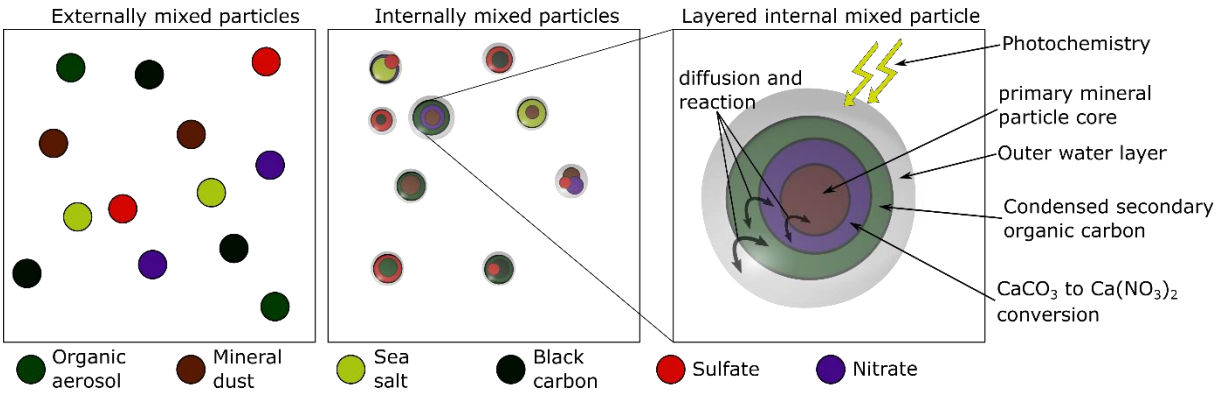

Figure 4: Mixing states of aerosol particles based on the most common components. The layered structure of an atmospherically aged particle is shown, with typical reaction and diffusion processes between the respective layers.

Physicochemical properties of aerosol particles are strongly correlated with their internal and external mixing state as shown in Figure 4.[108] While internally mixed particles are self-contained units (single particles), including different compounds, structures and related reactions, externally mixed particles are populations of multiple single particles separated within a certain volume of air.[109] Among the most important chemical properties of aerosol particles larger than 0.1 µm are their inhomogeneity and composition. Although the composition of particles is less relevant for cloud formation and thus the

indirect aerosol effect, as about 80 % of the cloud condensation properties of particles can be explained by their size distribution rather than their chemical composition, they are major factors determining extinction and scattering of light by particles.[110,111] Nevertheless, the chemical composition of the particles affects their hygroscopicity and in turn their CCN activity. Highly hygroscopic nitrate particles like $Ca(NO_3)_2$ and $NaNO_3$ are formed from $CaCO_3$ mineral dust at the presence of nitric acid within a few hours due to their high CCN activity.[112] The immediate feedback of the earth's climate and temperature to intrinsic features of aerosol particles is called direct aerosol effect. Both, direct and indirect aerosol effects are found to decrease the overall earth temperature, with the direct contribution of anthropogenic aerosol of -0.35 W/m^2.[113] Even small fluctuations in the optical properties of particles therefore have a drastic effect on the global radiation balance. The optical properties of particles are usually described by the wavelength-dependent "single-scattering albedo" ω_0 (λ). The internal mixing ratio of the particles is highly complex and decisive for this physical measure. Internally mixed particles consist of a multitude of different chemical components. The degree of internal mixing usually increases due to aging of the particles in the atmosphere. For example, chemical substances can be adsorbed on the wet surface of particles, react with particle constituents or can be oxidized by the influence of sunlight, thereby forming new compounds and leading to particle growth.

The main components of atmospheric aerosols, whether of anthropogenic or natural origin, are inorganic ionic species as well as elemental and organic carbon (EC and OC). The cations of the particles are clearly dominated by ammonia, while alkali, alkaline earth metals and silicon also play an important role as main components in mineral dust and sea salt.[114] Among the trace elements, heavy metals such as zinc, iron, chromium, nickel, lead, cadmium or vanadium are of particular relevance, as they allow statements to be made about the harmful properties of a particle.[115] Ions such as sulphates, nitrates or ammonium allow conclusions to be drawn about the degree of atmospheric alteration and the influence of secondary anthropogenic sources on the particles.[116] Apart from the inorganic constituents, organic substances and black carbon are frequently found in aerosol particles and are dominant in aerosols from urban and industrialized areas.[117] Particular attention is paid to organic, polyaromatic hydrocarbons, so-called PAHs, with regard to long-term health hazards. Especially lung, skin and bladder cancer but also DNA, kidney and liver damage are reported.[6] It has been shown that the degradation products of PAHs, such as oxygenated or nitrated PAHs, are even more harmful and mobile in the environment than their parent compounds.[118,119] The main sources for PAHs are road traffic as well as energy and heat generation by burning of fossil fuels and biomass.[120] PAHs are mostly components of black carbon and ash particles and make a particularly significant contribution to air pollution. Their formation is based on the incomplete combustion of aliphatic and aromatic hydrocarbons. While the emission of PAHs and other persistent hydrocarbons in Europe has decreased continuously in recent years, by 47% between 1990 and 2003 according to Breivik et al.,[121] the opposite trend is observed in emerging industrial nations such as China and India. Particularly high concentrations have been measured so far, especially in some regions of China such as Sichuan and Fujian, due to the heavy use of fossil fuels and biomass.[122]

A detailed determination of the chemical constituents of aerosol particles and their internal mixing degree is required to identify particle sources and to understand the aging behavior of particles in the atmosphere. Only in this way is it possible to create meaningful climate models and to estimate the impact of particle pollution in the atmosphere on humans and the environment. Internally and externally mixed particles can be analyzed by a wide variety of different methods. Some of them are quantitative with a high sensitivity but restricted to the laboratory, others are very selective and can even measure single particles in field. The next chapter will provide an overview of the most important analytical methods, their field of application, and their respective advantages and disadvantages.

1.2.3 Techniques used for aerosol measurements

Analytical techniques for the measurement of particles smaller than 10 µm can be distinguished based on the physical and chemical parameters investigated. For example, the particle size, particle number concentration or particle surface are typical representatives of physical measurement parameters. The particle size distribution is a decisive factor for cloud formation from condensation nuclei and also determines cloud properties, i.e., density, size and persistence. A readily accessible parameter to characterize an aerosol population is the particle number concentration, which can be calculated from the volume of air that was sucked in for collection of a bunch of particles – typically on filter papers or by means of impactors - and by the weight of those particles which is determined gravimetrically. Impactors additionally allow for a size-selected particle number concentration.[123] Apart from physical properties, the chemical components and optical appearance of aerosol particles are of major interest, as they allow to make conclusion about particle sources and aging.[80,116] From such receptor-oriented approaches, typically divided into microscopic and chemical analysis techniques, the latter are described in more detail in the following.

The chemical composition of fine dust particles is commonly determined by quantitative analytical methods like atomic absorption spectroscopy (AAS), inductively coupled plasma mass spectrometry (ICP-MS), ion chromatography (IC), proton-induced X-ray emission spectroscopy (PIXE) or X-ray fluorescence (XRF).[117,124–127] All of these methods are suitable for the quantitative analysis of either water-soluble or total inorganic aerosol components, but are, in case of AAS and ICP-MS particularly used for determination of trace metal components.[128,129] The organic components of the aerosol particles are often of greater importance, both in terms of their absorption properties of light and from a health point of view. Elemental analysis is used to quantify inorganic, elemental and organic carbon, but is very time and labor intense.[130] An exact characterization of all organic components is hardly possible by a single technique and rather requires multiple analytical tools. Prominent combinations are, for example, gas chromatography mass spectrometry (GC-MS) and liquid chromatography mass spectrometry (LC-MS).[131] The large number of methods, each very selective to a certain group of analytes, impressively demonstrates how complex the determination of all components within an aerosol sample can become. Hildemann et al., for example, used gravimetric analysis to determine aerosol mass, XRF to quantify heavy metals, IC and AAS for ionic components, GC-MS for organic species and a thermal evolution and combustion technique for determination of elemental carbon to finally achieve an almost complete material balance on the bulk chemical content.[132] All of the above mentioned methods are based on collecting the particles on filters and then, except for PIXE and XRF, this is followed by laborious extraction, clean-up and concentration procedures and final analysis in the laboratory. Such techniques are called offline analysis methods. Reactivity, volatility and sorption behavior of the substances sampled for lab measurements often lead to artifacts, as well as changes in substance properties and quantities, even before the actual analysis.[133] Early attempts with laser microprobe MS (LAMMS) instruments based on LDI, allowed to unravel the molecular composition of aerosol particles on filter samples at the single-particle level, without the necessity of analyte extraction procedures.[134]

In contrast to offline methods, the online techniques such as online mass spectrometry and online particle counters allow the direct measurement of particles in the environment.[135] This effectively prevents contamination or chemical changes of the particles due to storage and transport. The online mass spectrometers differ mainly in the number of particles used for the measurement. If the mass spectra are generated from the measurement of several particles, the spectra reflect the sum of the chemical information of these particles (so-called "multi-particle mass spectrometry" - MPMS). MPMS, also referred to as aerosol mass spectrometry (AMS) offers the advantage that the evaporation and ionization of the particles are two separate processes within one instrument, which allows a quantification of

particle components. Typical setups include an aerodynamic lens inlet, a chopper to separate the particles into defined packages followed by flash vaporization, ionization and the final measurement in a quadrupole analyzer.[136] Although positive matrix factorization in MPMS allows the assignment of particle classes within a bulk particle population, this method is highly dependent on large datasets and initial parameters for the calculation. This can lead to significant errors in the assignment.[137] However, statements about the internal mixing degree of a single particle directly from the measurement data cannot be made with this method. In contrast to MPMS, single-particle mass spectrometry (SPMS) can be used to obtain information about the composition of individual aerosol particles and thus can provide access to their internal mixing state.[63] The ionization method can also be adapted to the requirements for the analysis. For example, the chemical ionization or single-photon ionization by means of vacuum UV (VUV) allows for an almost fragmentation-free ionization of organic molecules.[138,139] While LDI is thought to be selective towards inorganic compounds, the so-called resonance-enhanced multiphoton ionization (REMPI) process leads to selective formation of intact organic radical ions.[140] By using different lasers for desorption (IR laser) and ionization (UV or VUV), it is even possible to obtain information about the makeup of the individual particles.[141] A much more precise classification of a single particle, compared to the abovementioned methods can be achieved by bipolar single-particle aerosol mass spectrometry, which was developed by Hinz et al in 1996.[142] While the measurement of only positive or negative ions gives hints about the composition of the original particle, bipolar measurements provide reliable statements about the correlation of positive and negative ions. Using ToF MS enables a high temporal resolution up to several hundreds of particles per second, depending on laser shot frequency, particle transmission of the inlet system and data recording rather than ToF measurement speed. More recently, the separation of desorption and a two-step ionization process, involving the combination of REMPI and LDI, allowed for very sensitive bipolar detection of organic and inorganic compounds from the same particle.[143]

1.2.4 Laser mass analyzer for particles in the airborne state (LAMPAS)

The LAMPAS 3 instrument is a highly integrated mass spectrometric device, combining particle aerodynamic size determination with bipolar mass spectrometry and respective data acquisition and data evaluation unit. The system offers excellent conditions for autarkic single-particle measurements especially under field conditions.[144] Due to its compact dimensions 1.52 x 0.64 x 0.57 m (*H* x *L* x *W*) and easy transportability (weight: 150 kg), the LAMPAS 3 instrument enables determination of the chemical composition of single aerosol particles in the size range from 200 nm to 10 µm even at remote places. The bipolar configuration allows for a simultaneous detection of positively and negatively charged ions from the same particle. It consists of three main instrumental parts, an atmospheric pressure interface (inlet system), the LDI ion source and two ToF mass analyzers with reflector geometry as shown in Figure 5.

The particles are transferred from the surrounding air through the suction of the inlet system into the mass spectrometer. The differentially pumped inlet system is divided into three vacuum stages, separated by a nozzle, a skimmer and an orifice with decreasing opening sizes of 500, 400 and 300 µm, respectively. The same inlet system was tested and used before in the LAMPAS 2 instrument and provides an acceptable detection efficiency of 10^{-3} for particles with 800 nm aerodynamic diameter.[145] The task of the inlet system is not only the transfer of the particles, but also their size selection and focusing of the particle beam to reduce its divergence in the ionization region. The pressures in the different stages during operation are about 10 mbar behind the nozzle, 10^{-2} mbar behind the skimmer and 2×10^{-6} in the main chamber behind the orifice plate. These pressures are achieved by means of two turbomolecular pumps (70 and 250 L/s) for stage 2 and 3 respectively and a rotary vane oil pump for the first stage. A diaphragm pump provides the backing vacuum for the two turbomolecular pumps.

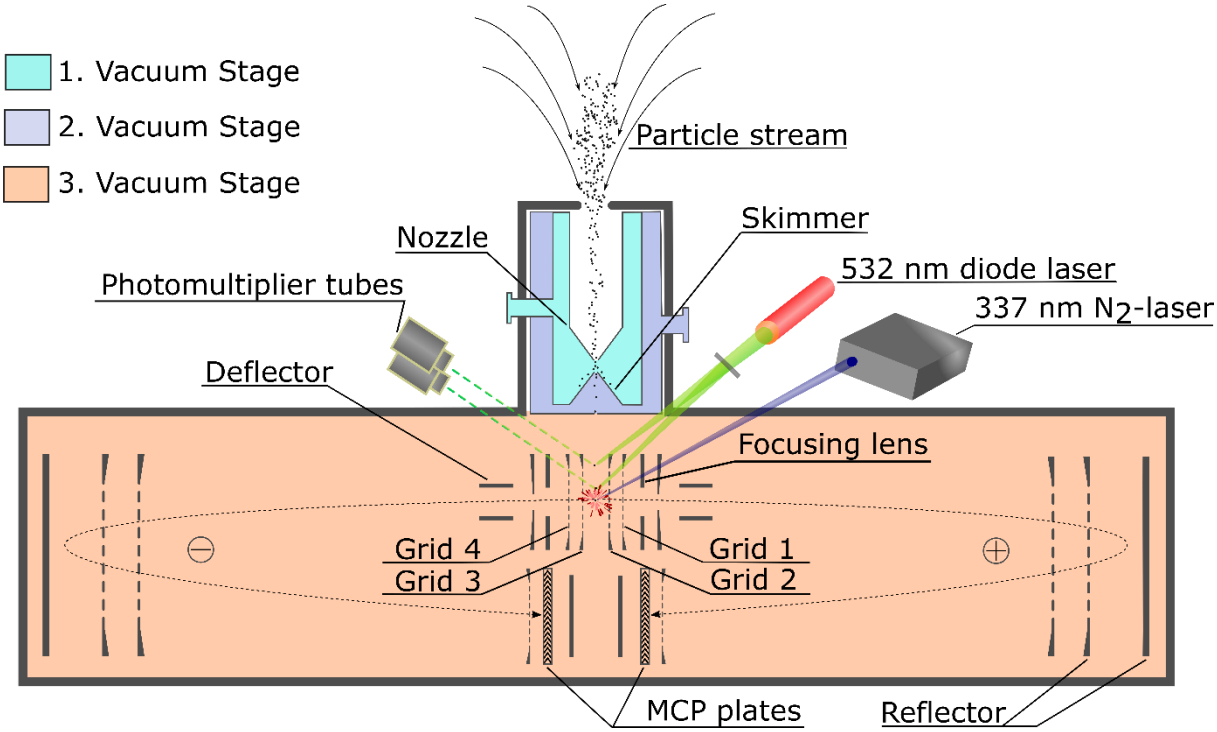

Figure 5: Schematic of the LAMPAS 3 instrument consisting of inlet system, ion source and ToF mass analyzers for positively and negatively charged ions, respectively. The three vacuum stages, divided by a nozzle, a skimmer and an orifice are shown in different colors.

After passing the small orifice, the particle velocity is detected by two continuous laser beams of a diode-pumped frequency doubled Nd:YVO_4 laser (λ = 532 nm) at a constant distance of 3.3 mm. The accelerated particles pass both beams of the diode laser while the scattered light is transmitted by several optical fiber cables to two photomultiplier tubes (PMT). The electric signal produced by the scattered light is then processed by two discriminator units, one for each PMT channel, to filter signal intensities from incident light of particles > 200 nm from smaller particles, electric noise and background photons. If the signal-to-noise ratio of the scattered light is high enough, a coincidence unit checks whether the signals of both PMTs are within a predefined time window, which means that they come from the same particle. The rectangular output pulses of the coincidence unit, one for each time the particle passes through the laser beam, are then evaluated by an active triggering unit. Via the time interval between the signals, the active triggering unit calculates the time delay in which the ionization laser (N_2 laser, λ = 337 nm, 250 mJ per pulse, 3 ns pulse width) must be triggered to hit the particle exactly in its laser focus (Ø ~ 30 µm). Due to the known distance between both detection laser beams, the aerodynamic diameter can be determined for unknown particles by prior calibration of the system with polystyrene latex spheres of different sizes. By measuring the velocities of the spheres, which depends on their aerodynamic diameter, the delay time for unknown particles can be determined from their calculated velocities.

After the particles were hit by the focused 337 nm ionization laser beam at a typical power density of 10^9 W/cm^2, a certain amount of material from the particles, depending on the pulse energy (can be varied by means of an attenuator) and on the particles size and composition, is then desorbed and ionized. The range of laser irradiance used for the LAMPAS 3 is above the ionization threshold of ~ 2 • 10^6 W/cm^2 reported for LDI, thus creating a dense plasma containing neutrals, positively and negatively charged ions as well as electrons at the ionization region.[146,147] The ions are extracted by two electrode grids per flight time tube (two-stage acceleration) for each positively and negatively charged ions, in opposite directions. Typical voltage settings are 0 and 0.3 kV at grid 1 and 2 and 5.8 and 6.8 kV at grid 3 and 4,

respectively. An ion lens is used to focus the ion beam and a deflector to guide the ion packages through static ion reflectors at the end of each flight tube. After passing the field-free region a second time, which results in a total length of 630 mm for both polarities, they are detected by microchannel plates (MCPs) producing a voltage pulse for each ion package, whose area is proportional to the number of ions measured over the time-of-flight. An oscilloscope covert these pulses into digital signals which can be recorded and processed by a PC. Typical mass resolutions of R = 300 can be achieved in positive- and negative-ion mode.

A major disadvantage of single-particle time-of-flight mass spectrometry and ionization using LDI is the strong fragmentation of ions and molecules in the resulting plasma. It can be reduced by attenuating the laser energy at the expense of the amount of ions generated, which is of decisive importance especially when measuring the smallest particles. The major advantage of the instrument is the bipolar arrangement of the flight tubes which allows the simultaneous determination of two oppositely charged ion types of one and the same particle and thus drastically increases the number of identified compounds.[142] Correlations between ions of different polarities likewise simplify the assignments of mass spectra with unit resolution.

1.2.5 Ultra-high-resolution mass spectrometry imaging (MSI)

Mass spectrometry imaging (MSI) has first been described for secondary ion mass spectrometry (SIMS) in 1962 by Castaing and Slodzian for the analysis of semiconductors.[148] Based on this idea and encouraged by the search for the spatial distribution of inorganic ions in biological samples, the technique of laser microprobing mass analysis (LAMMA) was invented in the 1970`s by Franz Hillenkamp and Raimund Kaufmann.[37] The idea was to develop a combination of an optical microscope with a laser mass analyzer to unravel information on the location of inorganic ions within a sample. The technique allowed for the correlation of *m*/*z*-ratios and signal intensities, corresponding to qualitative and quantitative analyte information, with location-based data from a sample surface. Ionization by LDI and subsequent measurement of ions with mass spectrometry limited the approach to small inorganic substances, due to high fragmentation. The latter has been overcome by the invention of matrix-assisted laser desorption/ionization (MALDI) in 1985, providing the analysis of larger unfragmented biomolecules.[40,149]

In 1994, Spengler et al. reported the combination of the laser microprobe principle and the MALDI method with coaxial geometry and two-dimensional scanning of a sample under high laser focusing conditions.[150] MALDI mass spectrometry imaging is nowadays the most important mass spectrometric imaging technique for biological tissue samples.[151,152]

In contrast to many classical biochemical identification methods, MALDI does not require complicated labelling of target molecules or extensive sample preparation. In contrast to secondary ion mass spectrometry (SIMS), MALDI MSI can be used without the need for ionization under high vacuum conditions, which is why it is regarded as an ambient ionization method.[153,154] Lateral resolution of typical MALDI imaging sources is in the range of 5 – 50 µm, when using highly focused UV-laser beams.[155] More recently, subcellular spatial resolution < 2 µm was reported.[156] Operating MSI sources on ultra-high resolution mass spectrometers like FT-ICR or orbital trapping devices with $R > 30000$ and mass accuracies better than 1 ppm allows for highly reliable assignments of *m*/*z*-values to molecular formulas.

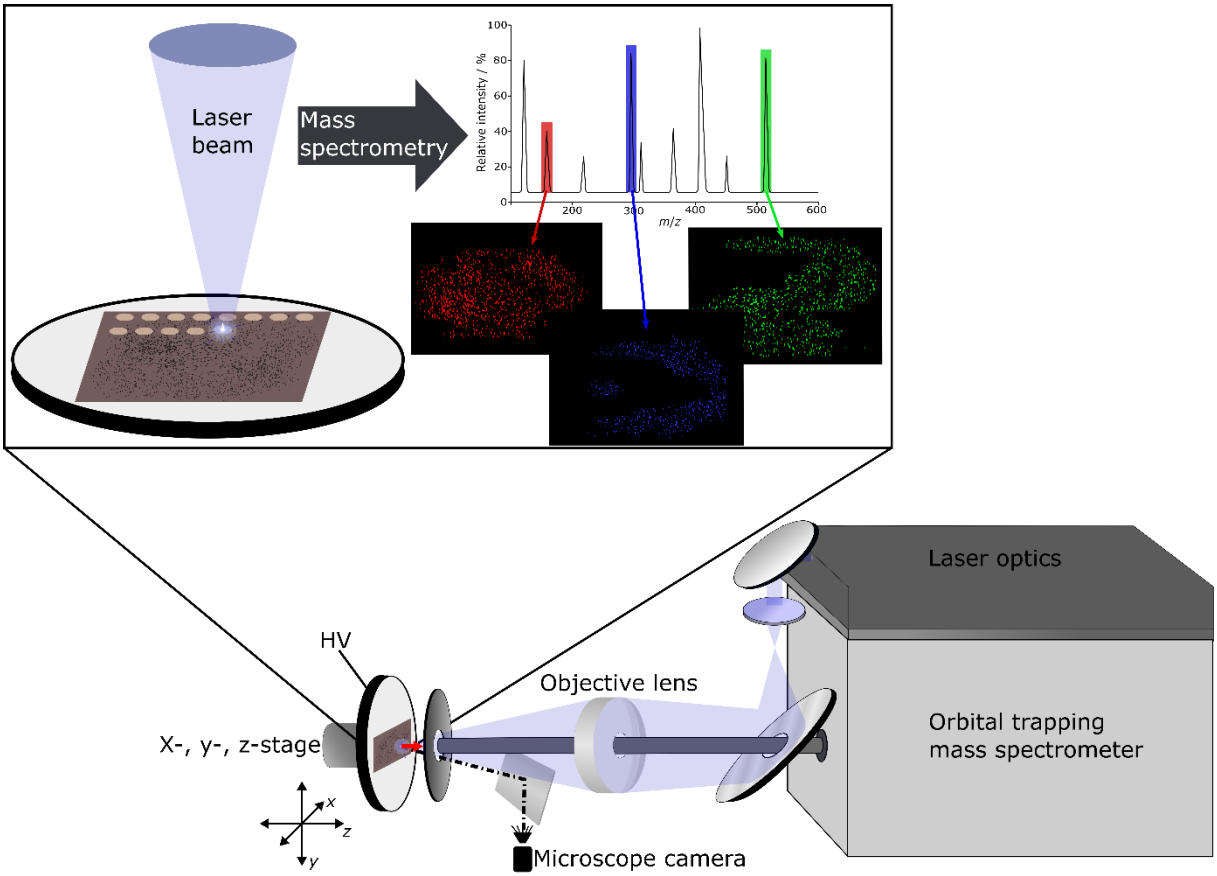

Figure 6: Principle of LDI imaging by the example of a filter paper covered with tiny aerosol particles. The filter paper is mounted on an x-, y-, z-stage and high voltage is applied, while a highly focused UV-laser beam desorbs and ionizes material from the surface spot by spot. The ions are measured by an ultra-high resolution orbital trapping mass spectrometer, allowing to create images with compound specific intensity distributions.[155]

For LDI imaging, thin surfaces containing the analytes of interest are scanned by a desorption laser to determine their molecular compositions. Particularly for MALDI, which is highly suitable for examination of large organic molecules, tissue sections are additionally covered with a thin layer of organic matrix prior to measurement, supporting desorption and ionization by strong optical absorption and preventing molecules from fragmentation by distribution of excess energy. A schematic of an LDI imaging measurement procedure applied to atmospheric particles on a filter paper is shown in Figure 6. The prepared sample is fixed on a sample holder, which is mounted on a precisely moveable *x*-, *y*-, *z*-stage. Observation of the sample surface is possible by a microscope camera, allowing to position the fixed laser beam on a certain point of interest. While illuminating the selected focus spot with highly intense UV-light pulses, a certain amount of sample, strongly depending on pulse energy and focus diameter, is desorbed and ionized. The ionized material is transferred via an atmospheric pressure interface into the mass spectrometer and a mass spectrum is acquired, representing the composition of the ionized material in the ablated area. Subsequently, the stage is moved to the next spot, which is treated the same way, until the whole area of interest is measured. Later on, the software assigns each location on the sample to the corresponding mass spectrum, often exceeding several thousand in number, depending on the pixel size (distance between two spot centers) and measurement area.[157] From this information, MS images can be created by selecting a small *m*/*z*-window and plotting the contained signal intensities, converted to gray scale values or color gradients on a grid with *x*- and *y*-coordinates. As a result, compound specific intensity distributions (selected ion images) are obtained.[155] Demanding surface topographies have so far been a major obstacle for MSI as well, as the samples had to be as flat as possible in order to avoid variations of the laser spot size and thus fluctuations of the laser intensity.

This has been overcome recently by the invention of a triangulation-based autofocusing system, capable of measuring even samples with strong variations in their height profile.[158] Earlier attempts to measure for example biological specimens suffered from additional sample prerequisites and preparation steps, such as cutting and embedding to create very thin and flat surfaces.[155] Due to their extreme surface roughness, particle measurements on glass fiber or quartz filters were also not possible until now and were limited to very flat surfaces or the collection of particles on transmission electron microscope (TEM) grids.[159]

Reaching high lateral resolutions with MALDI MSI is a very challenging task, as it does not only depend on the focal size of the laser and thus the physical properties, but also on matrix application and composition.[160] Sample handling and preparation are crucial to minimize matrix crystal size, enhance co-crystallization and prevent analyte spreading by dissolution. These effects have often been observed with organic dissolved matrices, leading to distorted compound mapping and reduced resolution.[161] More recently, inorganic alternatives emerged, including graphite, graphene, carbon nanotubes, gold and silver nanoparticles as well as nanophotonic surfaces.[162–167] Many of these compounds have been proven to be very effective in ionization and fragmentation-free measurements of small, often nonpolar molecular compounds, successfully preventing interferences with matrix ions below *m*/*z* 700.[168,169] Matrices that are not reliant on liquid solvents are of particular interest. Graphite particles, for example, served as matrix for the measurement of filter extracts to detect oligomeric species of isoprene photooxidation.[170] Direct measurements of particles generated by smog chamber experiments without further treatment were carried out by Kalberer et al.[171] They used graphite and crystalline titanium nitride (TiN) particles deposited on impactor plates before sampling the aerosol on these targets. However, using the abilities of already existing black carbon aerosol particles on filter samples, acting as matrix, does not need sample preparation and has been shown to be well suited for the determination of inorganic and organic particle components.[172] Jaoui et al. claimed that filter extracts mixed with graphite particles and particles measured directly from impactor stages provided similar results.[173] Measurements of particles on filter samples by LDI successfully demonstrated the utility of this approach for sensitive detection of organic compounds in low concentrations, particularly PAHs and nitro-PAHs.[151] Quantification of analytes on surfaces has been shown to exhibit high accuracy due to higher ionization yields and increased limit of detection by graphite-assisted ionization.[174] Fragmentation can be reduced, artifacts are successfully prevented and the limit of detection for organic compounds compared to inorganic ions is increased. Additionally, the use of atmospheric-pressure MSI effectively prevents evaporation of volatile and semi-volatile compounds from sample surfaces, which has been a major obstacle until now.[172]

Assignment of signals within high-mass-resolution imaging mass spectra to atomic compositions of molecules typically relies on their exact mass and fragmentation spectra from tandem mass spectrometry (MS^2) experiments. Combination of both measures in combination with database search engines have been proven to be highly suited for a reliable identification of compounds in untargeted experiments.[175] Identification is made significantly more difficult if MS^2 is not available, either technically or due to inhomogeneous and thus unpredictable analyte distribution within a sample. Furthermore, the number of possible atomic combinations (sum formulas) for a given signal, even under high mass accuracy and at high resolution, increases significantly when the number of possible elements increases. This applies especially for atmospheric particles, as these mixtures of inorganic and organic compounds can contain almost any element found on earth. This means that even database-assisted search engines cannot be used for the majority of compounds, since molecules in atmospheric particles are often very unspecific or insufficiently documented in databases. However, there are a number of options to simplify the assignment, including isotope distributions, isotope ratio analysis, elemental probability restriction and

Kendrick mass defect plots.[57,176] Issues can arise from interpretation of isotopic distributions and intensities for orbital trapping mass analyzers, as very low-abundant signals can be underrepresented by a factor of up to 10 % due to cut-off values, influencing isotopic beat patterns during data acquisition.[177] However, if MSI is coupled to an ultra-high-resolution orbital trapping mass spectrometer, highly reliable compound annotations and their accurate presentation in space are possible. Location-based compositions of inorganic and organic substances in positive- and negative-ion mode can be unraveled, while carbon particles serve as "in-situ" matrix on aerosol filter samples as shown in publication 2 of this work.

1.2.6 Statistical methods for the identification of particle sources

Not only is data generation important to achieve a desired result, but data handling and evaluation is even more critical, especially for MSI applications and single-particle MS, as both are non-targeted and deal with a variety of possible organic and inorganic molecular compounds. Furthermore, the occurrence of possible elements for molecular formula assignments in atmospheric particle populations is theoretically not restricted and predictions can only be made based on their abundance in, for example, the earth's crust. However, assumptions made for naturally occurring particles are of limited value when anthropogenic sources are involved, some of which are characterized by rare earths or heavy metals, leading to non-trivial spectra, complicating the assignment of ions to *m*/*z*-ratios. For all these reasons, manual evaluation of several thousands of spectra and their source apportionment becomes extremely complicated and inefficient. For single-particle laser MS, due to nominal mass resolution and high fragmentation, this becomes particularly clear. Therefore, particles can only be traced back to their sources by statistical methods, as small differences in the spectra are revealed that would not be noticed by manual inspection. Structuring and organizing large heterogeneous datasets in order to find similar mass spectral patterns is provided by a variety of mathematical functions.

The aim of these methods is to reduce huge datasets by harvesting significant information from the gathered spectra. In search for similar characteristics in the spectra, statistical algorithms cluster them, based on different variables like *m*/*z*-values or signal intensities. Each cluster is then considered as a class of similar internally mixed particles and can be assigned to a particle source according to its characteristic signal intensities and distributions.[135] However, the dependence of the ionization probability of individual molecules or atoms on the ionization potential, the particle matrix and the existing chemical bonds complicate intercomparability between spectra.[178] Therefore, the spectra have to be appropriately prepared before evaluation in order to achieve better comparability, reproducibility and reliability. This includes, among others, an accurate calibration, the normalization of signal intensities to reference values (total ion count, largest signal, average signal intensity, etc.) and scaling of the signal intensities by mathematical functions like logarithmic and square root to avoid strong intensity variations.[179–181] The required variables are then extracted from the pre-processed spectra and combined in a multidimensional matrix, including as many dimensions as variables.

The most widely used multivariate statistical methods are principal component analysis (PCA), k-means or fuzzy-c-means clustering, hierarchical cluster analysis (HCÀ) and artificial neural networks (ART-2a).[142,179,182,183] The goal of a PCA analysis is to reduce the number of dimensions in a multidimensional input matrix, while trying to keep the loss of information as low as possible. The illustration of the data is thus significantly improved and the coherence emphasized. K-means and fuzzy-c-means are so-called partitioning clustering methods, meaning that the number of clusters must be defined prior to clustering evaluation, while spectra with high similarities are grouped to this clusters.[135] They are frequently used in source identification and determination of aerosol properties from single-particle measurements.[135,184] Preselection of cluster number can be considered as a disadvantage, since there is usually an optimal

number of clusters to which the spectra can be assigned to. Both methods tend to get stuck in local minima during calculation, leading to wrong optimal cluster numbers, but nevertheless are appreciated for their efficiency and simplicity.[185] Fuzzy-c-means is denoted as "soft" algorithm, assigning spectra to clusters based on a membership degree, ranging from 0 (no membership) to 1 (full membership).[135] Especially for strongly internally mixed atmospheric particles, this is meant to be closer to reality than assigning spectra to a cluster by a "hard" algorithm using a yes/no criterion as for example k-means does. However, comparative evaluation of the same dataset with both algorithms barely showed any differences.[186] Furthermore, k-means outperforms fuzzy-c-means in terms of speed and computing power.[187] In contrast to k-means and fuzzy-c-means, hierarchical clustering starts with as many clusters as there are spectra. As the analysis progresses, the spectra (clusters) with high similarity are merged together in a joining-tree (dendrogram) finally forming a single cluster, containing all spectra.[179] The similarity between the spectra in the dendrogram is illustrated by the length of each branch of the tree until they are merged. This method is very time consuming and computationally intensive.[188] Recently, the Art-2a algorithm has been increasingly used, as it can be trained based on preexisting clusters and is therefore particularly suitable for real time online classification.[189] However, for single-particle measurements it has been shown, that best clustering results are achieved by using dual polarity spectra from a particle.[190] Each algorithm uses different types of distance functions to establish the relationship between variables and cluster centers. The choice of the distance calculation is critical and strongly depends on the chosen dataset.[191] Some well-known methods are Euclidean, Manhattan and Pearson correlation-based distance metrics.[180,192] Since the signal areas of two ions of different polarity from the same compound usually have a high correlation and are therefore linearly dependent on each other, the Pearson correlation method is well suited.[180] This is especially true for bipolar MS as long as no mathematical scaling functions are applied, typically disturbing such linear relationships. In contrast, the Euclidean distance calculation, which uses the direct distance between two variables in space, offers advantages as soon as highly intense signals should be separated from lower ones.

Often, combinations of the different statistical algorithms are the best option. The intrinsic problem of partitioning cluster algorithms to get lost in local minima, for example, has recently been circumvented by combining them with particle swarm optimization (PSO) methods.[185,193] PSO uses global stochastic variation in order to optimize multivariate functions. The advantages of computationally intensive HCA and fast partitioning clustering algorithms can also be combined. A limited number of start clusters at hierarchical clustering can be achieved by preprocessing large datasets with fuzzy-c-means or k-means calculations.[135] Choosing, for example, 50 start clusters from 2000 spectra, will reduce the start value for the HCA by a factor of 40, but at the same time it can be assumed that with 50 clusters the largest part of the variability of the internally mixed particles is covered. Instead of using completely unsupervised statistical methods, a promising approach relies on preselection of characteristic signals upfront of classification. In such a way, the influence of large but insignificant signals on the resulting clusters can be prevented. Schmidt et al. showed the efficiency of this approach by comparing representative lab-measured particle populations with online-derived data of ice particles for source apportionment.[180] Choosing selective characteristic signals from lab-measured single-particle populations of reference materials and aging-related features from online-measured populations, enables to visualize time-dependent aging of atmospheric particles according to predefined sources, as shown in publication 1 in this work. Not only single-particle spectra are optimally suited for multivariate statistical evaluation. Numerous examples show the application of PCA and clustering methods for MSI measurements.[194–198] This idea was therefore likewise adapted for source apportionment of particles on filter samples in publication 2.

Regardless of the clustering method used, spectra patterns are finally calculated for each generated cluster, representing the mean signal intensity of the associated spectra. Evaluation and sorting of the spectra patterns is typically done manually, based on chemical knowledge, particle mixing characteristics and expected particle sources. Reliability and accuracy of multivariate statistical analysis approaches therefore often rely on starting criteria and manual interpretation of results. Therefore, the quality of results often depends less on the algorithm used than on the user and his knowledge about the classified data.

1.3 Influence of regional and remote factors on the particle population in remote regions (Publication 1)

Climate strongly depends on aerosol particles, whether by direct influence due to scattering and absorption of sunlight and earth radiation, or indirectly as cloud condensation nuclei.[100,102,199] The first two factors become more relevant when the particle size exceeds the critical diameter of about 200 nm, while at the same time these particles become less important for cloud formation.[200] Light scattering and absorption behavior mainly depend on the particle size and shape, but as well on the chemical composition.[3,18,113,201 110] Strongly hydrophilic particles containing easily soluble sulfates, nitrates and sea salt, are considered as generally cooling, due to enhanced light scattering.[3,202] Soot or BC in contrast absorbs sunlight in a broad spectral range, and is therefore associated with climate warming.[3,18] In general, the contribution of anthropogenic aerosol to the global radiation balance is negative, and thus cooling.[100] However, more realistic observations and models include mixtures of different particle types and high fractions of mineral dust.[110] Strong scattering is attributed to these particles, which decreases due to agglomeration or even increases by aging reactions with acidic gaseous components in the atmosphere.[203–206] Besides that, most mineral particles (quartz, calcite and gypsum) are highly reflective, in contrast to, for example, hematite that exhibits high absorption.[204] From this, it is of particular importance to differentiate between fresh and aged mineral particles and different mineral particle types. Furthermore, the net effects of scattering and absorption is drastically increased if the underlying surface is particularly reflective. This is the case in snow-covered alpine regions, where even the relatively strong scattering of the mineral aerosol particles reduces the reflectivity of the snow cover (snow albedo). The increased melting of snow and ice as a side effect, induced by particle coverage, is gaining more and more attention in the last years, but it is, however, only little proven empirically.[207,208] It was found that this effect plays a significant role when the amount of mineral particles in the atmosphere and their deposition on the snow increases above average, for example during volcanic eruptions or sandstorm events.[209,210] In addition, the increased solubility of aged mineral particles, in particular calcite and dolomite particles, is leading to higher precipitation during transport and reduced stability at snow contact.[211]

However, such effects could be well studied in remote locations like the Jungfraujoch high altitude research station at 3580 m asl, in the Swiss Alps as shown by several published multiple-measurement campaigns.[178,212–214] Schmidt et al. furthermore demonstrated, that characteristic features of aerosol particles could be derived from laboratory measurements and applied to online-measured populations.[180] Particularly at the Jungfraujoch site, regional influences are still only poorly understood, and applied measurement techniques and evaluation procedures do not allow for a comprehensive differentiation of mineral particle sources and transportation pathways. Combination of bipolar single-particle mass spectrometry and reference-particle-supported multivariate statistical classification offers an excellent solution to address this issue.[215]

1.3.1 Laboratory and on-line single-particle measurements[215]

To assess these effects and to gain a deeper insight into which particle sources, regional or remote, are of particular importance in the free troposphere at the Jungfraujoch measurement site, atmospheric and laboratory-derived bipolar single-particle mass spectra served as basis for a refined evaluation method. Supplementary data to prove signal intensities and plausibility was taken from ICP-MS measurements. For the allocation of mineral particles, reference spectra from Alpine rock stone, Morocco desert sand and Rhine river sediment were measured in the laboratory as model systems. Artificial aging of these spectra should allow to identify aged mineral particles as well. These results were compared with atmospheric particle spectra measured at the “Cloud and Aerosol Characterization Experiment”

CLACE-1 campaign between March 17, 2000 and March 24, 2000 at the Jungfraujoch research station in the Swiss alps, which was influenced by periods of intense sandstorm events.

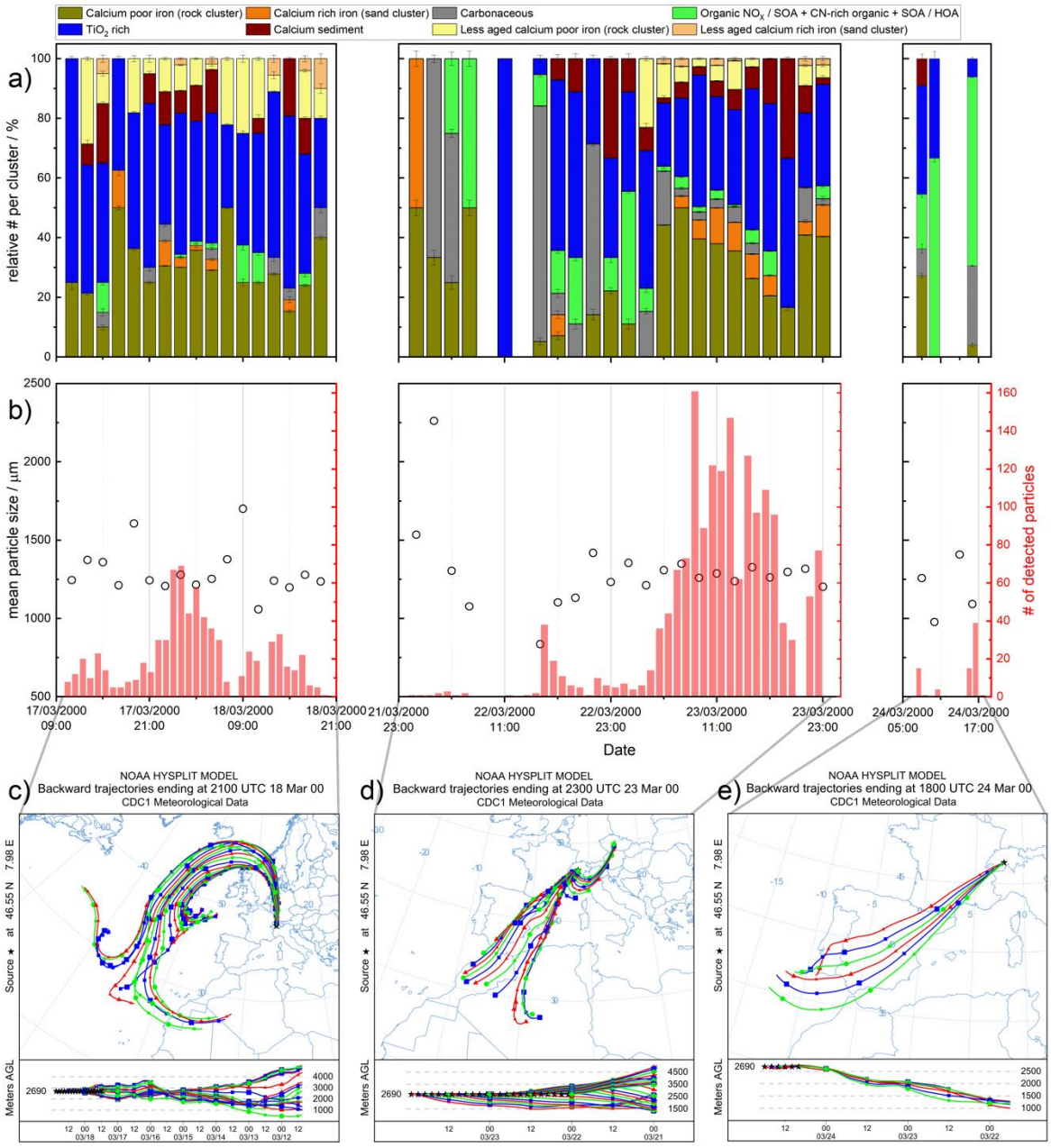

Figure 7: Atmospheric particle composition during three measurement episodes at CLACE-1, derived from model system comparisons in two-hour intervals a) and the respective number and mean size of these particles as derived from the LAMPAS 2 particle detection system b). HYSPLIT back trajectories of air masses arriving at the measurement station within these time slots for 180 h c) and 72 hours d) and e) are shown likewise.

Particle sources, apart from typical particle compositions on the measurement site, could be addressed on basis of sedimented and accumulated particles in dried-up snow water samples from the Jungfraujoch top region, representing an average particle population over a longer period of time. The size range of mineral aerosol particles from the model populations and the sandstorm events between 200 nm and 10 µm was ideally suited for single-particle measurements with the LAMPAS instruments. For all 3432 measured spectra, intensity scaling to the total ion count was used to normalize the signal intensities in an interval between 0 and 1. In order to distinguish individual sources and their share in the total

composition of atmospheric, river sediment and dried-up snow-water particles, they were classified by a hierarchical clustering algorithm preprocessed by k-means, as these are expected to be external mixtures of different mineral components. Characteristic compound features of Alpine rock stone, Morocco desert sand and Rhine river sediment were identified prior to the clustering approach through a systematic comparison of the model populations and was later used as sorting criteria. A correlation-coefficient-based distance metric was used for classification, as in-depth characterizations of model system spectra showed excellent correlations between positive and negative ions, expected to result from the same compounds. Finally, the classes derived from the atmospheric particles were compared to aged and non-aged model system spectra to differentiate between different particle sources and their atmospheric processing during transportation in high altitude. HYSPLIT back trajectories were simulated for the measurement episodes for 180 and 72 hours to back up the composition data and support source-based hypothesis.

The particle composition at the Jungfraujoch high altitude research station for three episodes in the year 2000 (March 17 at 9 am to March 18 at 10 pm, March 21 at 11 pm to March 23 at 12 am and March 24 at 5 am to March 24 at 7 pm) could be resolved in two-hour intervals as shown in Figure 7 a). The huge variety of differently aged and non-aged particles could be allocated to a total of 8 particle classes, whereas 6 out of these classes were assigned to mineral sources and precursors like aged sand particles (calcium rich iron), aged rock particles (calcium poor iron), river sediment particles (calcium sediment), titanium oxide particles (TiO_2-rich), less-aged sand (less-aged calcium rich) and less aged rock particle (less-aged igneous rock). Carbonaceous (Carbonaceous) and organic particles (organic NOx/SOA + CN-rich organic + HOA/SOA) provide additional information about the typical composition of mostly anthropogenic influences like local traffic and industrial emissions at the remote location, which was of particular relevance on March 22nd and March 24th. Back trajectories showed that these particles are dominated by continental air from the east on March 22 and from the Iberian Peninsula on March 24th. However, the focus was on the composition of atmospheric particles during the sandstorm, which were clearly visible in the dramatically increased particle numbers (Figure 7 b) on all other measurement days, particularly on March 17th in the evening and March 23rd. Both days showed similar trends for the different particle classes, but strongly differed in the number of incoming and detected particles. The number of particles on March 23rd was about twice as high as on March 17th and 18th, which can be attributed to the differences in transport paths and residence times of the particles in the atmosphere. On March 17th and 18th the transport took about 180 hours as shown in Figure 7 c), due to indirect transport over the Atlantic Ocean while on March 23rd the particles were transported directly over the Mediterranean Sea from the southwest direction within 70 hours (Figure 7 d)). The composition of the first incoming particles at each event started with a majority of less-aged calcium-poor iron particles, most likely silicates. Very soon, typically after 2 to 4 hours, the composition changed to more aged calcium-poor iron particles, showing a typical conversion of carbonate to nitrate, as expected from reactions of primarily calcium carbonate with gaseous nitric acid. The first aged calcium-rich iron particles were detected on March 17th at 5 pm and 11 pm and on March 23rd at 7 am, which was another two to four hours later. At the same time the proportion of aged and less-aged rock particles decreased constantly (March 23rd between 1 and 9 pm). Calcium sediment and TiO_2-rich particles were found on all measurement days in different ratios and can therefore be attributed to local sources (Alpine calcium basement rock and dolomite) and intensely aged remote mineral particles, which can hardly be assigned to a distinct source.

The observed effects can be explained by the initial particle composition and their transformation during atmospheric transport. The initial particles from the Sahara Desert outbursts are expected to consist of a mixture of calcium carbonate and calcium-poor silicon-rich particles. Especially the calcium-poor

particle types react to a lesser extent with nitric acid, and conversion to nitrate takes longer. Predominately, the first arriving particles were able to react with the atmospheric acids and neutralized them to a large extent due to their high number concentration. In this process, the calcium-rich particles in particular were converted into nitrates, and their increased hygroscopicity leads to greater precipitation during long range transport, as a result of which the poorly aged particles survived and were measured at the beginning of each event. High numbers of insoluble mineral particles sedimenting on the reflective snow cover will induce local temperature increase and enhanced snow smelt, particularly during late winter and early spring when less fresh snowfall is expected. It was shown that this effect is increasingly important during the frequently occurring dust storm events and with high probability also exceeds the effect of deposited and strongly absorbing black carbon from anthropogenic sources.

1.4 Particle characterization and quantification of organic and inorganic compounds from Chinese and Iranian aerosol filter samples using scanning laser desorption/ionization mass spectrometry (Publication 2)

Air pollution in many heavily populated regions of the world is a major issue, with 3.3 million premature deaths attributed to outdoor air pollution worldwide.[216] The emission of urban aerosols, a mixture of organic and inorganic substances, is of particular concern due to its detrimental impacts on human health. 82 % of the world's population is exposed to mean levels of $PM_{2.5}$ or PM_{10} that exceed the WHO`s air quality guidelines (20 µg/m^3 for PM_{10} and 10 µg/m^3 for $PM_{2.5}$).[11,217] Particulate matter in highly polluted regions usually originates from the same sources, such as heavy industry, coal combustion for power generation, traffic, and the burning of organic material in private households.[218,219] An additional complicating factor for certain cities is their location in valley depressions, enclosed by mountain ranges, surrounded by deserts or exposed to marine winds. The associated weather conditions, frequent calm winds, and seasonal events such as sandstorms significantly exacerbate particle pollution.[220,221]

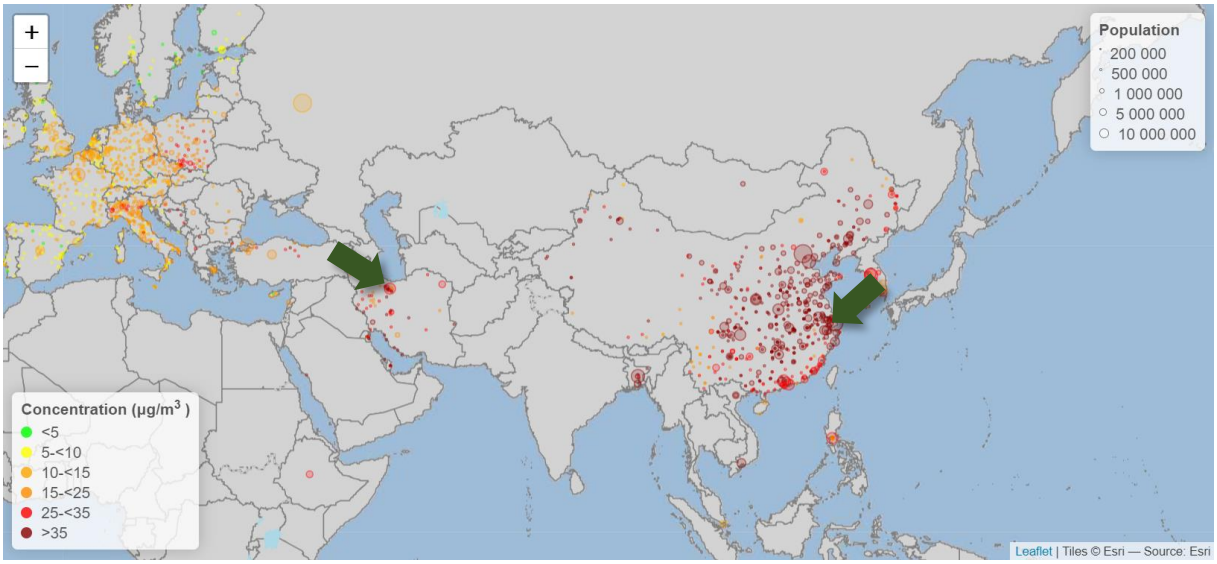

Figure 8: Overview of regions exceeding WHO`s mean $PM_{2.5}$ levels in 2016.[222] The two regions covered in this study (Tehran and Hangzhou) are marked by arrows.

The map in Figure 8 shows particularly heavily polluted regions in Asia, Europe and the Arabian Peninsula from 2016.[222] The accumulation of limit violations in eastern China and Iran is striking. This is particularly relevant for Iran because no new data were recorded in this country after 2016 and

therefore no air monitoring by the WHO has taken place since then.[217] Hence, the focus of this work was on the two heavily polluted megacities Hangzhou in China and Tehran in Iran marked by green arrows in Figure 8. In both cities, particles were collected on quartz filters in 2018 and later on analyzed in the laboratory.[223]

The majority of the methods used for characterizing air quality as described in section 1.2.3 are limited by their ability to gain enough selective molecular insight into the sampled particles to allow conclusions about their chemical and physical properties as well as sources and atmospheric alterations. Mass spectrometric measurements coupled with chromatographic separation techniques would allow comprehensive chemical characterization of the collected particles, but require extensive sample preparation steps and prevent assignment of the measured compounds to individual particle assemblies.[224,225] Thus, in the present study, the advantages of high-resolution atmospheric-pressure laser desorption/ionization mass spectrometry imaging and statistical evaluation of imaging data were combined to identify as many substances as possible in the sample, even close to the single-particle level.[223] A standard-addition calibration approach requiring very little sample preparation was used to allow quantification of PAHs that are considered to have carcinogenic and mutagenic properties.[6]

1.4.1 Extensive chemical characterization of particles on filter samples[223]

The comprehensive evaluation of filter samples collected on two days in Hangzhou (China) and Tehran (Iran) led to the assignment of around 3258 mass signals, excluding isotopic features. Mass concentrations in Hangzhou were found to be significantly higher than those in Tehran, as well as respective numbers of assigned sum formulae. The samples from Tehran contained higher amounts of sulphur-containing organic compounds and heavy-metal species, while the samples from Hangzhou showed higher amounts of CHO-containing compounds and PAHs as shown in Figure 9. This difference is likely due to the SO_2 air pollution control policy in China on the one hand and traffic-related sources in Tehran on the other. It was also observed that the relative number of CHO-containing compounds was reduced compared to other studies, due to the parallel detection of inorganic compounds and PAHs. Oxy-PAHs were only found in the samples from Hangzhou, suggesting that these particles were exposed to oxidizing compounds in the atmosphere for a longer period of time compared to the particles in Tehran. This observation was verified by evaluation of the double-bond equivalents (DBE) of organic molecules, which, as a structural descriptor, can be used to separate compounds into functional groups. The results showed that the Hangzhou samples had higher DBEs for all compounds, especially in the PAH class, indicating that the PAHs were from more distant sources, such as coal combustion and remote traffic. The Tehran samples on the other hand showed higher oxidation of nitrogenous compounds, suggesting that these originate from car exhaust. Statistical evaluation of the high-resolution atmospheric-pressure laser desorption/ionization mass spectrometry data revealed a number of 168 significant compounds in negative-ion mode and 186 significant compounds in positive-ion mode for both cities. A recurring motif here was the high proportion of sulfur-containing compounds in the samples from Tehran while for Hangzhou mainly highly molecular PAHs and oxy-PAHs, some CHN species and inorganic calcium were found to be characteristic. Tehran samples in general were dominated by lower-molecular-weight PAHs, CHON species and inorganic chromium compounds.

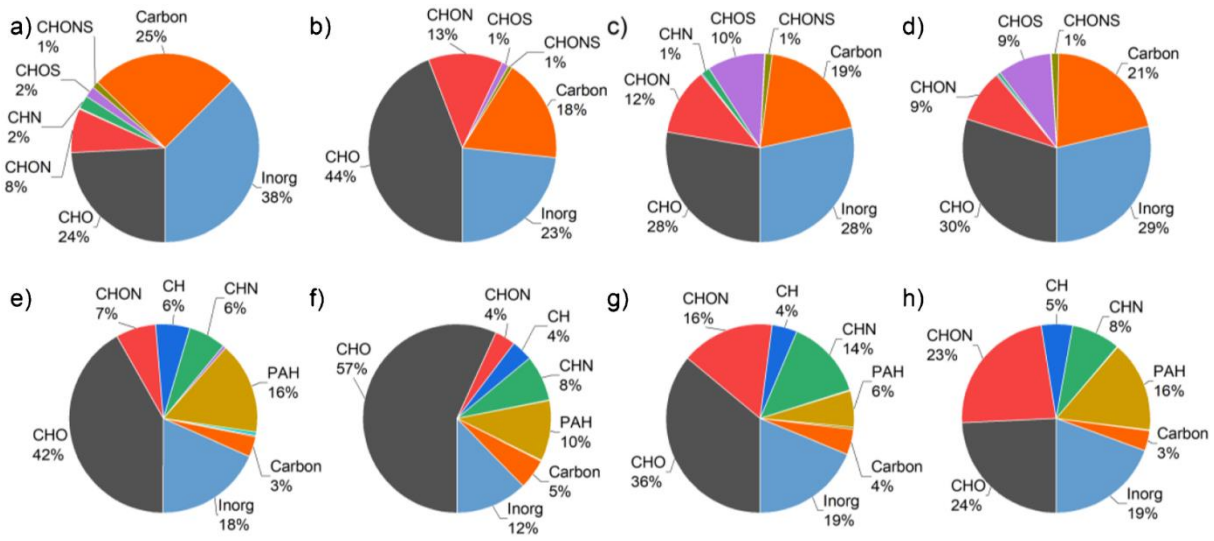

Figure 9: 11 identified particle classes in negative- (a–d) and positive-ion mode (e–h) are shown. Measurements of the Chinese filters on day 1 (a, e) and day 2 (b, f) and Iranian filters on day 1 (c, g) and day 2 (d, h) exhibit characteristic features for each location.

Furthermore, the samples were subjected to a statistical clustering approach, in which the generated mass spectra were correlated with their respective measurement location on the sample surface. Structurally similar compounds could thus be assigned to specific particle classes. Inorganic and organic compounds could both be detected and occurred in the same data cluster, allowing to draw conclusions about mixing of different chemical components and ageing or the composition of primary particles. Prominent data clusters include black carbon, mineral clusters, PAHs, plant materials, SOA, calcium compounds, caprolactam, methyl methacrylate and inorganic iron. The presence of heavy metals mixed with PAHs and SOA in the samples from Tehran is concerning and may lead to negative consequences for human health. Even quantification of 13 selected PAH species was possible on the same samples by using a dried droplet method. It was found that the PAH concentrations in samples from Tehran were twice as high as in those from Hangzhou. The higher concentrations of PAHs in Tehran samples were primarily caused by small organic and soot particles.

For the first time, ambient LDI MSI was used to analytically characterize the chemical composition of aerosol particles sampled with/on quartz fiber filters. The technique has been proven to be particularly useful for untargeted analysis of particles, allowing for the characterization of small communities of particles and the identification of different particle classes (data clusters). Using an autofocusing MALDI MSI source enabled to compensate for the extensive surface roughness of the filter and allowed for constant and high ion signals throughout the whole ablated area. An ultrahigh-resolution orbital trapping mass analyzer was used to differentiate very small differences in *m*/*z* values and to identify more than 3200 sum formulae in positive- and negative-ion mode with quite a number of them as intact molecular compounds instead of fragments. The method easily accesses a variety of organic or inorganic molecular information in aerosol particles. Results showed a reduction in the number of sulphur compounds and nitric oxide compounds in particles from Hangzhou, China, compared to the samples from Tehran which may indicate a successful Chinese sulphur dioxide emission policy. Despite lower mass loadings of the filters from Tehran, Iran, the relative number of heavy-metal-containing compounds and polycyclic aromatic hydrocarbons (PAHs) were higher, raising concerns about the exposure of the population in Tehran to toxic pollutants.

1.5 Conclusion and perspective

Subordinate to the topic of chemical characterization of aerosol particles, the present work highlights two sides of a coin. On the one hand, the in-situ single-particle analysis in a remote region in the Swiss Alps and, on the other hand, the laboratory analysis of particle samples from heavily polluted megacities.

The combination of ToF MS and aerosol single-particle ionization in the field allowed for the determination of the composition of numerous individual aerosol particles. Changes to the particles that might occur during collection, transport and storage have been effectively eliminated. This method is particularly effective when combined with multivariate statistical evaluation methods, such as PCA, clustering or neuronal networks.[178,215] A large proportion of the particles at the Jungfraujoch site developed chemically over long distances, often several thousand kilometers away from the actual measurement location, and under the influence of different urban and natural factors. Only few methods in the field provide information comparable to in-situ SPMS. However, also the limitations of the instrument regarding the quality of the generated mass spectra and the resulting data used for further statistical evaluation became apparent. Instrumental limitations with regard to mass accuracy, mass resolution, ionization process and dynamic range necessitate extensive processing of the measured spectra, such as manual calibration, normalization, peak selection and filtering.[135] The detection of primarily mineral particle components, due to plasma ionization in a high vacuum and the associated strong fragmentation, further limits the system's range of application with regard to biological and organic aerosols.

In contrast, the use of a high-resolution mass detector and a softer AP-LDI process was proven to be beneficial for the untargeted detection of a huge variety of different organic as well as inorganic aerosol compounds. The measurement of particle filter samples using MALDI-Orbitrap MS provided a comprehensive overview of even secondary organic aerosols, polyaromatic hydrocarbons, fatty acids and sugars due to its high mass resolution, high accuracy and low fragmentation. Statistical cluster analysis of the data allowed for the assignment of complex combinations of particle components to particle classes, revealing their origin and source more clearly than in-situ SPMS. Even quantification of PAHs was possible although with significant errors. However, due to the rather large laser focus with a diameter of approximately 50 µm, a clear assignment of the mass spectra to a single particle was limited and a risk of chemical alteration of the particles after collection and during storage cannot be excluded.

As demonstrated, high-resolution AP-LDI MS compensates for many of the disadvantages of single-particle in-situ ToF MS but lacks on the crucial portability and provides a lower measurement frequency and limit of detection.[226–228] While some instrumental adjustments of ToF SPMS, like for example delayed ion extraction, orthogonal acceleration and multiple ion reflection can improve the mass resolving power (up to 100,000) and increase the mass accuracy, they are often incompatible with the requirements of a mobile system.[229] Moreover, the quantification aspect and high fragmentation of particles caused by laser bombardment under low pressure conditions remains challenging.[182]

Finally, an ideal single-particle aerosol mass spectrometer, capable of measuring inorganic and organic compounds with high mass resolution, which is fast, compact and sensitive at the same time, combined with acceptable electronic requirements would be extremely difficult to develop. Nevertheless, an approximation to the ideal properties is certainly conceivable. Experiences made in this work with in-situ TOF SPMS, offering a comparably low mass resolution (~300) and laboratory measurements with ionization at ambient pressure using ultra-high-resolution MS provide the path for further developments. There is a great interest for accurate source apportionment of organic as well as inorganic pollutants

resulting from biomass burning, coal combustion and heavy traffic and their reliable identification that creates special instrumental and methodological demands.[230] The results of this work indicate that a combination of orbital trapping mass analyzers and ambient pressure single-particle laser ionization combined into a portable instrument would be a promising approach to meet the majority of those requirements. Technological aspects for dual polarity ion measurements and miniaturization of Orbitrap instruments are already available. [231,232] However, transfer of ions generated from single particles into vacuum conditions which is necessary to operate an orbitrap mass analyzer is challenging and will therefore remain part of future research. Such a system would not only be ideally suited for measurements in heavily polluted regions worldwide in order to specify source of particles responsible for adverse health effects. But it also has the potential to enhance the differentiation between local particles sources and particles that travelled over long distance at remote measurement locations, like deserts or the arctic regions.

2 References

1. IUPAC. Compendium of Chemical Terminology. the "Gold Book". Online version (2019-) created by S. J. Chalk. (2009).
2. Kolb, C. E. & Worsnop, D. R. Chemistry and composition of atmospheric aerosol particles. *Annual review of physical chemistry* **63,** 471–491; 10.1146/annurev-physchem-032511-143706 (2012).
3. M. Schulz *et al.* Radiative forcing by aerosols as derived from the AeroCom present-day and pre-industrial simulations. *Atmospheric Chemistry and Physics* **6,** 5246 (2006).
4. Bäumer, D. *et al.* Relationship of visibility, aerosol optical thickness and aerosol size distribution in an ageing air mass over South-West Germany. *Atmospheric Environment* **42,** 989–998; 10.1016/j.atmosenv.2007.10.017 (2008).
5. Tie, X. X. *et al.* The impact of high altitude aircraft on the ozone layer in the stratosphere. *J Atmos Chem* **18,** 103–128; 10.1007/BF00696810 (1994).
6. Kim, K.-H., Jahan, S. A., Kabir, E. & Brown, R. J. C. A review of airborne polycyclic aromatic hydrocarbons (PAHs) and their human health effects. *Environment international* **60,** 71–80; 10.1016/j.envint.2013.07.019 (2013).
7. Tang, S. *et al.* Aerosol transmission of SARS-CoV-2? Evidence, prevention and control. *Environment international* **144,** 106039; 10.1016/j.envint.2020.106039 (2020).
8. Lanz, V. A. *et al.* Characterization of aerosol chemical composition with aerosol mass spectrometry in Central Europe: an overview. *Atmos. Chem. Phys.* **10,** 10453–10471; 10.5194/acp-10-10453-2010 (2010).
9. Henderson-Sellers, A. & McGuffie, K. *The future of the world's climate* (Elsevier, Waltham, MA, 2012).
10. World Health Organization. *Ambient air pollution: a global assessment of exposure and burden of disease* (World Health Organization, 2016).
11. *Air quality guidelines. Global update 2005: particulate matter, ozone, nitrogen dioxide and sulfur dioxide* (World Health Organization Regional Office for Europe, Copenhagen, 2006).
12. Bernstein, J. A. *et al.* Health effects of air pollution. *The Journal of allergy and clinical immunology* **114,** 1116–1123; 10.1016/j.jaci.2004.08.030 (2004).
13. Hu, X. *et al.* Bioaccessibility and health risk of arsenic and heavy metals (Cd, Co, Cr, Cu, Ni, Pb, Zn and Mn) in TSP and PM2.5 in Nanjing, China. *Atmospheric Environment* **57,** 146–152; 10.1016/j.atmosenv.2012.04.056 (2012).
14. Tie, X. & Cao, J. Aerosol pollution in China: Present and future impact on environment. *Particuology* **7,** 426–431; 10.1016/j.partic.2009.09.003 (2009).
15. Bard, S. M. Global Transport of Anthropogenic Contaminants and the Consequences for the Arctic Marine Ecosystem. *Marine Pollution Bulletin* **38,** 356–379; 10.1016/S0025-326X(99)00041-7 (1999).
16. Glicker, H. S. *et al.* Chemical composition of ultrafine aerosol particles in central Amazonia during the wet season. *Atmos. Chem. Phys.* **19,** 13053–13066; 10.5194/acp-19-13053-2019 (2019).
17. Fang, C., Liu, H., Li, G., Sun, D. & Miao, Z. Estimating the Impact of Urbanization on Air Quality in China Using Spatial Regression Models. *Sustainability* **7,** 15570–15592; 10.3390/su71115570 (2015).
18. Ramanathan, V. & Carmichael, G. Global and regional climate changes due to black carbon. *Nature Geosci* **1,** 221–227; 10.1038/ngeo156 (2008).

19. Wien, W. Über positive Elektronen und die Existenz hoher Atomgewichte. *Annalen der Physik* **318,** 669–677; 10.1002/andp.18943180404 (1904).

20. Thomson, J. J. XIX. Further experiments on positive rays. *The London, Edinburgh, and Dublin Philosophical Magazine and Journal of Science* **24,** 209–253; 10.1080/14786440808637325 (1912).

21. Bakerian Lecture :—Rays of positive electricity. *Proc. R. Soc. Lond. A* **89,** 1–20; 10.1098/rspa.1913.0057 (1913).

22. Dempster, A. J. Isotopic Constitution of Uranium. *Nature* **136,** 180; 10.1038/136180a0 (1935).

23. Dempster, A. J. A new Method of Positive Ray Analysis. *Phys. Rev.* **11,** 316–325; 10.1103/PhysRev.11.316 (1918).

24. Washburn, H., Wiley, H. & Rock, S. Mass Spectrometer as Analytical Tool. *Ind. Eng. Chem. Anal. Ed.* **15,** 541–547; 10.1021/i560121a001 (1943).

25. McLafferty, F. W. Mass Spectrometric Analysis Broad Applicability to Chemical Research. *Anal. Chem.* **28,** 306–316; 10.1021/ac60111a005 (1956).

26. Gohlke, R. S. Time-of-Flight Mass Spectrometry and Gas-Liquid Partition Chromatography. *Anal. Chem.* **31,** 535–541; 10.1021/ac50164a024 (1959).

27. Biemann, K. & McCloskey, J. A. Application of Mass Spectrometry to Structure Problems.1VI. Nucleosides2. *J. Am. Chem. Soc.* **84,** 2005–2007; 10.1021/ja00869a048 (1962).

28. Biemann, K., DeJongh, D. C. & Schnoes, H. K. Application of Mass Spectrometry to Structure Problems. XIII.1Acetates of Pentoses and Hexoses2. *J. Am. Chem. Soc.* **85,** 1763–1771; 10.1021/ja00895a015 (1963).

29. Budzikiewicz, H., Wilson, J. M. & Djerassi, C. Mass Spectrometry in Structural and Stereochemical Problems. XXXII.1Pentacyclic Triterpenes. *J. Am. Chem. Soc.* **85,** 3688–3699; 10.1021/ja00905a036 (1963).

30. Schulten, H.-R. Biochemical, medical, and environmental applications of field-ionization and field-desorption mass spectrometry. *International Journal of Mass Spectrometry and Ion Physics* **32,** 97–283; 10.1016/0020-7381(79)80087-X (1979).

31. Cameron, A. E., Smith, D. H. & Walker, R. L. Mass spectrometry of nanogram-size samples of lead. *Anal. Chem.* **41,** 525–526; 10.1021/ac60272a020 (1969).

32. Regelous, M., Turner, S. P., Elliott, T. R., Rostami, K. & Hawkesworth, C. J. Measurement of femtogram quantities of protactinium in silicate rock samples by multicollector inductively coupled plasma mass spectrometry. *Anal. Chem.* **76,** 3584–3589; 10.1021/ac030374l (2004).

33. Feist, P. & Hummon, A. B. Proteomic challenges: sample preparation techniques for microgram-quantity protein analysis from biological samples. *International journal of molecular sciences* **16,** 3537–3563; 10.3390/ijms16023537 (2015).

34. Bruins, A. P., Covey, T. R. & Henion, J. D. Ion spray interface for combined liquid chromatography/atmospheric pressure ionization mass spectrometry. *Anal. Chem.* **59,** 2642–2646; 10.1021/ac00149a003 (1987).

35. Fenn, J. B., Mann, M., Meng, C. K., Wong, S. F. & Whitehouse, C. M. Electrospray ionization for mass spectrometry of large biomolecules. *Science (New York, N.Y.)* **246,** 64–71; 10.1126/science.2675315 (1989).

36. Carroll, D. I., Dzidic, I., Stillwell, R. N., Haegele, K. D. & Horning, E. C. Atmospheric pressure ionization mass spectrometry. Corona discharge ion source for use in a liquid chromatograph-mass spectrometer-computer analytical system. *Anal. Chem.* **47,** 2369–2373; 10.1021/ac60364a031 (1975).

37. Hillenkamp, F., Unsöld, E., Kaufmann, R. & Nitsche, R. A high-sensitivity laser microprobe mass analyzer. *Appl. Phys.* **8,** 341–348; 10.1007/BF00898368 (1975).

38. Munson, M. S. B. & Field, F. H. Chemical Ionization Mass Spectrometry. I. General Introduction. *J. Am. Chem. Soc.* **88,** 2621–2630; 10.1021/ja00964a001 (1966).

39. Barber, M., Bordoli, R. S., Sedgwick, R. D. & Tyler, A. N. Fast atom bombardment of solids as an ion source in mass spectrometry. *Nature* **293,** 270–275; 10.1038/293270a0 (1981).

40. Karas, M. & Hillenkamp, F. Laser desorption ionization of proteins with molecular masses exceeding 10,000 daltons. *Anal. Chem.* **60,** 2299–2301; 10.1021/ac00171a028 (1988).

41. William E. Stephens. A Pulsed Mass Spectrometer with Time Dispersion. *Phys. Rev.* **69,** 674; 10.1103/PhysRev.69.674 (1946).

42. Dempster, A. J. New Methods in Mass Spectroscopy. *Proceedings of the American Philosophical Society* **75,** 755–767 (1935).

43. Mattauch, J. & Herzog, R. ber einen neuen Massenspektrographen. *Z. Physik* **89,** 786–795; 10.1007/BF01341392 (1934).

44. Miller, P. E. & Denton, M. B. The quadrupole mass filter: Basic operating concepts. *J. Chem. Educ.* **63,** 617; 10.1021/ed063p617 (1986).

45. Paul, W. & Steinwedel, H. Notizen: Ein neues Massenspektrometer ohne Magnetfeld. *Zeitschrift für Naturforschung A* **8,** 448–450; 10.1515/zna-1953-0710 (1953).

46. Penning, F. M. Die glimmentladung bei niedrigem druck zwischen koaxialen zylindern in einem axialen magnetfeld. *Physica* **3,** 873–894; 10.1016/S0031-8914(36)80313-9 (1936).

47. Comisarow, M. B. & Marshall, A. G. Fourier transform ion cyclotron resonance spectroscopy. *Chemical Physics Letters* **25,** 282–283; 10.1016/0009-2614(74)89137-2 (1974).

48. Allen, J. S. An Improved Electron Multiplier Particle Counter. *Review of Scientific Instruments* **18,** 739–749; 10.1063/1.1740838 (1947).

49. Ladislas Wiza, J. Microchannel plate detectors. *Nuclear Instruments and Methods* **162,** 587–601; 10.1016/0029-554X(79)90734-1 (1979).

50. Cohen, E. R. & Taylor, B. N. The 1986 CODATA Recommended Values of the Fundamental Physical Constants. *Journal of Physical and Chemical Reference Data* **17,** 1795–1803; 10.1063/1.555817 (1988).

51. Outlaw, R. A. Practical Aspects of Vacuum System Mass Spectrometers. In *Handbook of vacuum science and technology*, edited by D. M. Hoffmann, B. Singh & J. H. Thomas (Academic Press; Elsevier e-books, San Diego, 2014), pp. 335–375.

52. McNaught, A. D. & Wilkinson, A. (eds.). *IUPAC compendium of chemical terminology.* 2nd ed. (Blackwell Science, Oxford, 1997).

53. Haapala, M., Suominen, T. & Kostiainen, R. Capillary photoionization: a high sensitivity ionization method for mass spectrometry. *Anal. Chem.* **85,** 5715–5719; 10.1021/ac4002673 (2013).

54. Ibrahim, Y., Tang, K., Tolmachev, A. V., Shvartsburg, A. A. & Smith, R. D. Improving mass spectrometer sensitivity using a high-pressure electrodynamic ion funnel interface. *Journal of the American Society for Mass Spectrometry* **17,** 1299–1305; 10.1016/j.jasms.2006.06.005 (2006).

55. Schwartz, D. E. & Ranalder, U. B. Highly sensitive and specific determination of mefloquine in biological fluids using gas chromatography mass spectrometry with selected ion monitoring. *Biomedical mass spectrometry* **8,** 589–592; 10.1002/bms.1200081206 (1981).

56. Brenton, A. G. & Godfrey, A. R. Accurate mass measurement: terminology and treatment of data. *Journal of the American Society for Mass Spectrometry* **21,** 1821–1835; 10.1016/j.jasms.2010.06.006 (2010).

57. Kind, T. & Fiehn, O. Seven Golden Rules for heuristic filtering of molecular formulas obtained by accurate mass spectrometry. *BMC Bioinformatics* **8,** 105; 10.1186/1471-2105-8-105 (2007).

58. G Marshall, A. *et al.* Mass resolution and mass accuracy: how much is enough? *Mass spectrometry (Tokyo, Japan)* **2,** S0009; 10.5702/massspectrometry.S0009 (2013).

59. Makarov. Electrostatic axially harmonic orbital trapping: a high-performance technique of mass analysis. *Anal. Chem.* **72,** 1156–1162; 10.1021/ac991131p (2000).

60. Paul, W. Electromagnetic traps for charged and neutral particles. *Rev. Mod. Phys.* **62,** 531–540; 10.1103/RevModPhys.62.531 (1990).

61. Moskovets, E. *et al.* High-throughput axial MALDI-TOF MS using a 2-kHz repetition rate laser. *Anal. Chem.* **78,** 912–919; 10.1021/ac051393t (2006).

62. Vorm, O., Roepstorff, P. & Mann, M. Improved Resolution and Very High Sensitivity in MALDI TOF of Matrix Surfaces Made by Fast Evaporation. *Anal. Chem.* **66,** 3281–3287; 10.1021/ac00091a044 (1994).

63. Hinz, K.-P., Kaufmann, R. & Spengler, B. Laser-Induced Mass Analysis of Single Particles in the Airborne State. *Anal. Chem.* **66,** 2071–2076; 10.1021/ac00085a023 (1994).

64. Boesl, U. Time-of-flight mass spectrometry: Introduction to the basics. *Mass spectrometry reviews* **36,** 86–109; 10.1002/mas.21520 (2017).

65. Cai, Y.-H., Lai, Y.-H. & Wang, Y.-S. Coupled Space- and Velocity-Focusing in Time-of-Flight Mass Spectrometry-a Comprehensive Theoretical Investigation. *J. Am. Soc. Mass Spectrom.* **26,** 1722–1731; 10.1007/s13361-015-1206-y (2015).

66. Wiley, W. C. & McLaren, I. H. Time-of-Flight Mass Spectrometer with Improved Resolution. *Review of Scientific Instruments* **26,** 1150–1157; 10.1063/1.1715212 (1955).

67. Mamyrin, B. A., Karataev, V. I., Shmikk, D. V. & Zagulin, V. A. The mass-reflectron A new nonmagnetic time-of-flight high resolution mass-spectrometer. *Zhurnal Ehksperimental'noj i Teoreticheskoj Fiziki* **64,** 82–89 (1973).

68. Dawson, J. H. J. & Guilhaus, M. Orthogonal-acceleration time-of-flight mass spectrometer. *Rapid Commun. Mass Spectrom.* **3,** 155–159; 10.1002/rcm.1290030511 (1989).

69. Chernushevich, I. V., Merenbloom, S. I., Liu, S. & Bloomfield, N. A W-Geometry Ortho-TOF MS with High Resolution and Up to 100% Duty Cycle for MS/MS. *J. Am. Soc. Mass Spectrom.* **28,** 2143–2150; 10.1007/s13361-017-1742-8 (2017).

70. Kingdon, K. H. A Method for the Neutralization of Electron Space Charge by Positive Ionization at Very Low Gas Pressures. *Phys. Rev.* **21,** 408–418; 10.1103/PhysRev.21.408 (1923).

71. Lange, O., Damoc, E., Wieghaus, A. & Makarov, A. Enhanced Fourier transform for Orbitrap mass spectrometry. *International Journal of Mass Spectrometry* **369,** 16–22; 10.1016/j.ijms.2014.05.019 (2014).

72. Makarov, A., Denisov, E., Lange, O. & Horning, S. Dynamic range of mass accuracy in LTQ Orbitrap hybrid mass spectrometer. *Journal of the American Society for Mass Spectrometry* **17,** 977–982; 10.1016/j.jasms.2006.03.006 (2006).

73. Makarov, A. *et al.* Performance evaluation of a hybrid linear ion trap/orbitrap mass spectrometer. *Anal. Chem.* **78,** 2113–2120; 10.1021/ac0518811 (2006).

74. Denisov, E., Damoc, E., Lange, O. & Makarov, A. Orbitrap mass spectrometry with resolving powers above 1,000,000. *International Journal of Mass Spectrometry* **325-327,** 80–85; 10.1016/j.ijms.2012.06.009 (2012).

75. Perry, R. H., Cooks, R. G. & Noll, R. J. Orbitrap mass spectrometry: instrumentation, ion motion and applications. *Mass spectrometry reviews* **27,** 661–699; 10.1002/mas.20186 (2008).

76. Olsen, J. V. *et al.* Parts per million mass accuracy on an Orbitrap mass spectrometer via lock mass injection into a C-trap. *Molecular & cellular proteomics : MCP* **4,** 2010–2021; 10.1074/mcp.T500030-MCP200 (2005).

77. Spracklen, D. V. *et al.* Explaining global surface aerosol number concentrations in terms of primary emissions and particle formation. *Atmos. Chem. Phys.* **10,** 4775–4793; 10.5194/acp-10-4775-2010 (2010).

78. Després, V. *et al.* Primary biological aerosol particles in the atmosphere: a review. *Tellus B: Chemical and Physical Meteorology* **64,** 15598; 10.3402/tellusb.v64i0.15598 (2012).

79. Hawkins, L. N. & Russell, L. M. Polysaccharides, Proteins, and Phytoplankton Fragments: Four Chemically Distinct Types of Marine Primary Organic Aerosol Classified by Single Particle Spectromicroscopy. *Advances in Meteorology* **2010,** 1–14; 10.1155/2010/612132 (2010).

80. Li, X. *et al.* Preliminary studies on the source of PM10 aerosol particles in the atmosphere of Shanghai City by analyzing single aerosol particles. *Nuclear Instruments and Methods in Physics Research Section B: Beam Interactions with Materials and Atoms* **210,** 412–417; 10.1016/S0168-583X(03)01058-9 (2003).

81. Miranda, R. M. de, Fátima Andrade, M. de, Worobiec, A. & van Grieken, R. Characterisation of aerosol particles in the São Paulo Metropolitan Area. *Atmospheric Environment* **36,** 345–352; 10.1016/S1352-2310(01)00363-6 (2002).

82. Harrison, R. M. *et al.* Studies of the coarse particle (2.5–10μm) component in UK urban atmospheres. *Atmospheric Environment* **35,** 3667–3679; 10.1016/S1352-2310(00)00526-4 (2001).

83. Wilson, W. E. & Suh, H. H. Fine particles and coarse particles: concentration relationships relevant to epidemiologic studies. *Journal of the Air & Waste Management Association (1995)* **47,** 1238–1249; 10.1080/10473289.1997.10464074 (1997).

84. Vignati, E. *et al.* Global scale emission and distribution of sea-spray aerosol: Sea-salt and organic enrichment. *Atmospheric Environment* **44,** 670–677; 10.1016/j.atmosenv.2009.11.013 (2010).

85. Dentener, F. *et al.* Emissions of primary aerosol and precursor gases in the years 2000 and 1750 prescribed data-sets for AeroCom. *Atmos. Chem. Phys.* **6,** 4321–4344; 10.5194/acp-6-4321-2006 (2006).

86. Heald, C. L. & Spracklen, D. V. Atmospheric budget of primary biological aerosol particles from fungal spores. *Geophys. Res. Lett.* **36**; 10.1029/2009GL037493 (2009).

87. Allan, J. D. *et al.* Contributions from transport, solid fuel burning and cooking to primary organic aerosols in two UK cities. *Atmos. Chem. Phys.* **10,** 647–668; 10.5194/acp-10-647-2010 (2010).

88. Huang, Y. *et al.* Quantification of global primary emissions of PM2.5, PM10, and TSP from combustion and industrial process sources. *Environ. Sci. Technol.* **48,** 13834–13843; 10.1021/es503696k (2014).

89. Clement, C. Gas-to-particle conversion in the atmosphere: I. Evidence from empirical atmospheric aerosols. *Atmospheric Environment* **33,** 475–487; 10.1016/S1352-2310(98)00264-7 (1999).

90. Chang, Y. *et al.* Nitrogen isotope fractionation during gas-to-particle conversion of NO_x to NO_3^- in the atmosphere – implications for isotope-based NO_x source apportionment. *Atmos. Chem. Phys.* **18,** 11647–11661; 10.5194/acp-18-11647-2018 (2018).

91. Zhang, R. *et al.* Atmospheric new particle formation enhanced by organic acids. *Science* **304,** 1487–1490; 10.1126/science.1095139 (2004).

92. Lee, S.-H. *et al.* New Particle Formation in the Atmosphere: From Molecular Clusters to Global Climate. *Journal of geophysical research. Atmospheres : JGR* **124,** 7098–7146; 10.1029/2018JD029356 (2019).

93. Zhong, Q. *et al.* Global Sulfur Dioxide Emissions and the Driving Forces. *Environ. Sci. Technol.* **54,** 6508–6517; 10.1021/acs.est.9b07696 (2020).

94. Guenther, A. B. *et al.* The Model of Emissions of Gases and Aerosols from Nature version 2.1 (MEGAN2.1): an extended and updated framework for modeling biogenic emissions. *Geosci. Model Dev.* **5,** 1471–1492; 10.5194/gmd-5-1471-2012 (2012).

95. Bianchi, F. *et al.* New particle formation in the free troposphere: A question of chemistry and timing. *Science* **352,** 1109–1112; 10.1126/science.aad5456 (2016).

96. Jokinen, T. *et al.* Ion-induced sulfuric acid-ammonia nucleation drives particle formation in coastal Antarctica. *Science Advances* **4,** 1-6; 10.1126/sciadv.aat9744 (2018).

97. Weber, R. J. *et al.* Measurements of new particle formation and ultrafine particle growth rates at a clean continental site. *J. Geophys. Res.* **102,** 4375–4385; 10.1029/96JD03656 (1997).

98. Gerhard, E. R. & Johnstone, H. F. Air Pollution Studies-Photochemical Oxidation of Sulfur Dioxide in Air. *Ind. Eng. Chem.* **47,** 972–976; 10.1021/ie50545a027 (1955).

99. Friend, J. P., Leifer, R. & Trichon, M. On the Formation of Stratospheric Aerosols. *J. Atmos. Sci.* **30,** 465–479; 10.1175/1520-0469(1973)030<0465:OTFOSA>2.0.CO;2 (1973).

100. Charlson, R. J. *et al.* Climate forcing by anthropogenic aerosols. *Science (New York, N.Y.)* **255,** 423–430; 10.1126/science.255.5043.423 (1992).

101. Merikanto, J., Spracklen, D. V., Mann, G. W., Pickering, S. J. & Carslaw, K. S. Impact of nucleation on global CCN. *Atmos. Chem. Phys.* **9,** 8601–8616; 10.5194/acp-9-8601-2009 (2009).

102. Twomey, S. The nuclei of natural cloud formation part II: The supersaturation in natural clouds and the variation of cloud droplet concentration. *Geofisica Pura e Applicata* **43,** 243–249; 10.1007/BF01993560 (1959).

103. Novakov, T. & Penner, J. E. Large contribution of organic aerosols to cloud-condensation-nuclei concentrations. *Nature* **365,** 823–826; 10.1038/365823a0 (1993).

104. Kavouras, I. G., Mihalopoulos, N. & Stephanou, E. G. Formation of atmospheric particles from organic acids produced by forests. *Nature* **395,** 683–686; 10.1038/27179 (1998).

105. George, I. J. & Abbatt, J. P. D. Heterogeneous oxidation of atmospheric aerosol particles by gas-phase radicals. *Nature Chem* **2,** 713–722; 10.1038/nchem.806 (2010).

106. McMurry, P. H. & Friedlander, S. K. Aerosol formation in reacting gases: Relation of surface area to rate of gas-to-particle conversion. *Journal of Colloid and Interface Science* **64,** 248–257; 10.1016/0021-9797(78)90360-0 (1978).

107. Paasonen, P. *et al.* Continental anthropogenic primary particle number emissions. *Atmos. Chem. Phys.* **16,** 6823–6840; 10.5194/acp-16-6823-2016 (2016).

108. Cheng, T., Wu, Y., Gu, X. & Chen, H. Effects of mixing states on the multiple-scattering properties of soot aerosols. *Optics express* **23,** 10808–10821; 10.1364/OE.23.010808 (2015).

109. Pósfai, M. & Buseck, P. R. Nature and Climate Effects of Individual Tropospheric Aerosol Particles. *Annu. Rev. Earth Planet. Sci.* **38,** 17–43; 10.1146/annurev.earth.031208.100032 (2010).

110. Dubovik, O. *et al.* Variability of Absorption and Optical Properties of Key Aerosol Types Observed in Worldwide Locations. *J. Atmos. Sci.* **59,** 590–608; 10.1175/1520-0469(2002)059<0590:VOAAOP>2.0.CO;2 (2002).

111. Dusek, U. *et al.* Size matters more than chemistry for cloud-nucleating ability of aerosol particles. *Science* **312,** 1375–1378; 10.1126/science.1125261 (2006).

112. Sullivan, R. C. *et al.* Timescale for hygroscopic conversion of calcite mineral particles through heterogeneous reaction with nitric acid. *Physical chemistry chemical physics : PCCP* **11,** 7826–7837; 10.1039/b904217b (2009).

113. Myhre, G. *et al.* Radiative forcing of the direct aerosol effect from AeroCom Phase II simulations. *Atmos. Chem. Phys.* **13,** 1853–1877; 10.5194/acp-13-1853-2013 (2013).

114. Putaud, J.-P. *et al.* A European aerosol phenomenology—2: chemical characteristics of particulate matter at kerbside, urban, rural and background sites in Europe. *Atmospheric Environment* **38,** 2579–2595; 10.1016/j.atmosenv.2004.01.041 (2004).

115. Saeedi, M., Li, L. Y. & Salmanzadeh, M. Heavy metals and polycyclic aromatic hydrocarbons: pollution and ecological risk assessment in street dust of Tehran. *Journal of hazardous materials* **227-228,** 9–17; 10.1016/j.jhazmat.2012.04.047 (2012).

116. Song, C. H. & Carmichael, G. R. The aging process of naturally emitted aerosol (sea-salt and mineral aerosol) during long range transport. *Atmospheric Environment* **33,** 2203–2218; 10.1016/S1352-2310(98)00301-X (1999).

117. Andreae, M. O. *et al.* Optical properties and chemical composition of the atmospheric aerosol in urban Guangzhou, China. *Atmospheric Environment* **42,** 6335–6350; 10.1016/j.atmosenv.2008.01.030 (2008).

118. Collins, J. F., Brown, J. P., Alexeeff, G. V. & Salmon, A. G. Potency equivalency factors for some polycyclic aromatic hydrocarbons and polycyclic aromatic hydrocarbon derivatives. *Regulatory toxicology and pharmacology : RTP* **28,** 45–54; 10.1006/rtph.1998.1235 (1998).

119. Elie, M. R. *et al.* Metabolomic analysis to define and compare the effects of PAHs and oxygenated PAHs in developing zebrafish. *Environmental research* **140,** 502–510; 10.1016/j.envres.2015.05.009 (2015).

120. Khalili, N. R., Scheff, P. A. & Holsen, T. M. PAH source fingerprints for coke ovens, diesel and, gasoline engines, highway tunnels, and wood combustion emissions. *Atmospheric Environment* **29,** 533–542; 10.1016/1352-2310(94)00275-P (1995).

121. Breivik, K., Vestreng, V., Rozovskaya, O. & Pacyna, J. M. Atmospheric emissions of some POPs in Europe: a discussion of existing inventories and data needs. *Environmental Science & Policy* **9,** 663–674; 10.1016/j.envsci.2006.09.001 (2006).

122. Xu, S., Liu, W. & Tao, S. Emission of polycyclic aromatic hydrocarbons in China. *Environ. Sci. Technol.* **40,** 702–708; 10.1021/es0517062 (2006).

123. Hillamo, R. E. & Kauppinen, E. I. On the Performance of the Berner Low Pressure Impactor. *Aerosol Science and Technology* **14,** 33–47; 10.1080/02786829108959469 (1991).

124. Pancras, J. P., Ondov, J. M. & Zeisler, R. Multi-element electrothermal AAS determination of 11 marker elements in fine ambient aerosol slurry samples collected with SEAS-II. *Analytica Chimica Acta* **538,** 303–312; 10.1016/j.aca.2005.01.062 (2005).

125. Cong, Z., Kang, S., Dong, S., Liu, X. & Qin, D. Elemental and individual particle analysis of atmospheric aerosols from high Himalayas. *Environ Monit Assess* **160,** 323–335; 10.1007/s10661-008-0698-3 (2010).

126. Bergametti, G., Dutot, A.-L., Buat-MéNard, P., Losno, R. & Remoudaki, E. Seasonal variability of the elemental composition of atmospheric aerosol particles over the northwestern Mediterranean. *Tellus B: Chemical and Physical Meteorology* **41,** 353–361; 10.3402/tellusb.v41i3.15092 (1989).

127. Cong, Z., Kang, S., Liu, X. & Wang, G. Elemental composition of aerosol in the Nam Co region, Tibetan Plateau, during summer monsoon season. *Atmospheric Environment* **41,** 1180–1187; 10.1016/j.atmosenv.2006.09.046 (2007).

128. Chandra Mouli, P., Venkata Mohan, S., Balaram, V., Praveen Kumar, M. & Jayarama Reddy, S. A study on trace elemental composition of atmospheric aerosols at a semi-arid urban site using ICP-MS technique. *Atmospheric Environment* **40,** 136–146; 10.1016/j.atmosenv.2005.09.028 (2006).

129. Salam, A., Bauer, H., Kassin, K., Mohammad Ullah, S. & Puxbaum, H. Aerosol chemical characteristics of a mega-city in Southeast Asia (Dhaka–Bangladesh). *Atmospheric Environment* **37,** 2517–2528; 10.1016/S1352-2310(03)00135-3 (2003).

130. Zappoli, S. *et al.* Inorganic, organic and macromolecular components of fine aerosol in different areas of Europe in relation to their water solubility. *Atmospheric Environment* **33,** 2733–2743; 10.1016/S1352-2310(98)00362-8 (1999).

131. O'Connell, S. G., Haigh, T., Wilson, G. & Anderson, K. A. An analytical investigation of 24 oxygenated-PAHs (OPAHs) using liquid and gas chromatography-mass spectrometry. *Anal Bioanal Chem* **405,** 8885–8896; 10.1007/s00216-013-7319-x (2013).

132. Hildemann, L. M., Markowski, G. R. & Cass, G. R. Chemical composition of emissions from urban sources of fine organic aerosol. *Environ. Sci. Technol.* **25,** 744–759; 10.1021/es00016a021 (1991).

133. Turpin, B. J., Huntzicker, J. J. & Hering, S. V. Investigation of organic aerosol sampling artifacts in the los angeles basin. *Atmospheric Environment* **28,** 3061–3071; 10.1016/1352-2310(94)00133-6 (1994).

134. Mauney, T., Adams, F. & Sine, M. R. Laser microprobe mass spectrometry of environmental soot particles. *Science of The Total Environment* **36,** 215–224; 10.1016/0048-9697(84)90269-9 (1984).

135. Hinz, K.-P., Greweling, M., Drews, F. & Spengler, B. Data processing in on-line laser mass spectrometry of inorganic, organic, or biological airborne particles. *J. Am. Soc. Mass Spectrom.* **10,** 648–660; 10.1016/S1044-0305(99)00028-8 (1999).

136. Jayne, J. T. *et al.* Development of an Aerosol Mass Spectrometer for Size and Composition Analysis of Submicron Particles. *Aerosol Science and Technology* **33,** 49–70; 10.1080/027868200410840 (2000).

137. Yuan, Z. B., Yu, J. Z., Lau, A. K. H., Louie, P. K. K. & Fung, J. C. H. Application of positive matrix factorization in estimating aerosol secondary organic carbon in Hong Kong and its relationship with secondary sulfate. *Atmos. Chem. Phys.* **6,** 25–34; 10.5194/acp-6-25-2006 (2006).

138. Hearn, J. D. & Smith, G. D. A chemical ionization mass spectrometry method for the online analysis of organic aerosols. *Anal. Chem.* **76,** 2820–2826; 10.1021/ac049948s (2004).

139. Woods, E., Smith, G. D., Dessiaterik, Y., Baer, T. & Miller, R. E. Quantitative detection of aromatic compounds in single aerosol particle mass spectrometry. *Anal. Chem.* **73,** 2317–2322; 10.1021/ac001166l (2001).

140. Heger, H., Boesl, U., Zimmermann, R., Dorfner, R. & Kettrup, A. On-line resonance-enhanced multiphoton ionization time-of-flight laser mass spectrometry for combined multi-component-pattern analysis and target-compound monitoring: non-chlorinated aromatics and chlorobenzene in flue gases of combustion processes. *Eur. J. Mass Spectrom.* **5,** 51; 10.1255/ejms.249 (1999).

141. Woods, E., Smith, G. D., Miller, R. E. & Baer, T. Depth profiling of heterogeneously mixed aerosol particles using single-particle mass spectrometry. *Anal. Chem.* **74,** 1642–1649; 10.1021/ac0110909 (2002).

142. Hinz, K.-P., Kaufmann, R. & Spengler, B. Simultaneous Detection of Positive and Negative Ions From Single Airborne Particles by Real-time Laser Mass Spectrometry. *Aerosol Science and Technology* **24,** 233–242; 10.1080/02786829608965368 (1996).

143. Schade, J. *et al.* Spatially Shaped Laser Pulses for the Simultaneous Detection of Polycyclic Aromatic Hydrocarbons as well as Positive and Negative Inorganic Ions in Single Particle Mass Spectrometry. *Anal. Chem.* **91,** 10282–10288; 10.1021/acs.analchem.9b02477 (2019).

144. Hinz, K.-P., Gelhausen, E., Schäfer, K.-C., Takats, Z. & Spengler, B. Characterization of surgical aerosols by the compact single-particle mass spectrometer LAMPAS 3. *Anal Bioanal Chem* **401,** 3165–3172; 10.1007/s00216-011-5465-6 (2011).

145. Trimborn, A., Hinz, K.-P. & Spengler, B. Online Analysis of Atmospheric Particles with a Transportable Laser Mass Spectrometer. *Aerosol Science and Technology* **33,** 191–201; 10.1080/027868200410921 (2000).

146. Dreisewerd, K., Schürenberg, M., Karas, M. & Hillenkamp, F. Influence of the laser intensity and spot size on the desorption of molecules and ions in matrix-assisted laser desorption/ionization with a uniform beam profile. *International Journal of Mass Spectrometry and Ion Processes* **141,** 127–148; 10.1016/0168-1176(94)04108-J (1995).

147. Ens, W., Mao, Y., Mayer, F. & Standing, K. G. Properties of matrix-assisted laser desorption. Measurements with a time-to-digital converter. *Rapid Commun. Mass Spectrom.* **5,** 117–123; 10.1002/rcm.1290050306 (1991).

148. Castaing, R. & Slodzian, G. Optique Corpusculaire - Premiers Essais De Microanalyse Par Emission Ionique Secondaire. *Comptes Rendus Hebdomadaires Des Seances De L Academie Des Sciences,* 1893–1895 (1962).

149. Karas, M., Bachmann, D. & Hillenkamp, F. Influence of the wavelength in high-irradiance ultraviolet laser desorption mass spectrometry of organic molecules. *Anal. Chem.* **57,** 2935–2939; 10.1021/ac00291a042 (1985).

150. Spengler, B., Hubert, M. & Kaufmann, R. MALDI Ion Imaging and Biological Ion Imaging with a new Scanning UV-Laser Microprobe. *Proceedings of the 42nd Annual Conference on Mass Spectrometry and Allied Topics,* 1041 (1994).

151. Bezabeh, D. Z. Screening of Aerosol Filter Samples for PAHs and Nitro-PAHs by Laser Desorption Ionization TOF Mass Spectrometry. *Aerosol Science and Technology* **30,** 288–299; 10.1080/027868299304642 (1999).

152. Takáts, Z., Wiseman, J. M., Gologan, B. & Cooks, R. G. Mass spectrometry sampling under ambient conditions with desorption electrospray ionization. *Science* **306,** 471–473; 10.1126/science.1104404 (2004).

153. Herzog, R. F. K. & Viehböck, F. P. Ion Source for Mass Spectrography. *Phys. Rev.* **76,** 855–856; 10.1103/PhysRev.76.855 (1949).

154. Laiko, V. V., Baldwin, M. A. & Burlingame, A. L. Atmospheric Pressure Matrix-Assisted Laser Desorption/Ionization Mass Spectrometry. *Anal. Chem.* **72,** 652–657; 10.1021/ac990998k (2000).

155. Römpp, A. & Spengler, B. Mass spectrometry imaging with high resolution in mass and space. *Histochemistry and cell biology* **139,** 759–783; 10.1007/s00418-013-1097-6 (2013).

156. Kompauer, M., Heiles, S. & Spengler, B. Atmospheric pressure MALDI mass spectrometry imaging of tissues and cells at 1.4-μm lateral resolution. *Nat Methods* **14,** 90–96; 10.1038/nmeth.4071 (2017).

157. Klinkert, I., Chughtai, K., Ellis, S. R. & Heeren, R. M. Methods for full resolution data exploration and visualization for large 2D and 3D mass spectrometry imaging datasets. *International Journal of Mass Spectrometry* **362,** 40–47; 10.1016/j.ijms.2013.12.012 (2014).

158. Kompauer, M., Heiles, S. & Spengler, B. Autofocusing MALDI mass spectrometry imaging of tissue sections and 3D chemical topography of nonflat surfaces. *Nat Methods* **14,** 1156–1158; 10.1038/nmeth.4433 (2017).

159. Denoyer, E., Natusch, D. F., Surkyn, P. & Adams, F. C. Laser microprobe mass analysis (LAMMA) as a tool for particle characterization: a study of coal fly ash. *Environ. Sci. Technol.* **17,** 457–462; 10.1021/es00114a004 (1983).

160. Bouschen, W., Schulz, O., Eikel, D. & Spengler, B. Matrix vapor deposition/recrystallization and dedicated spray preparation for high-resolution scanning microprobe matrix-assisted laser desorption/ionization imaging mass spectrometry (SMALDI-MS) of tissue and single cells. *Rapid Commun. Mass Spectrom.* **24,** 355–364; 10.1002/rcm.4401 (2010).

161. Buchberger, A. R., DeLaney, K., Johnson, J. & Li, L. Mass Spectrometry Imaging: A Review of Emerging Advancements and Future Insights. *Anal. Chem.* **90,** 240–265; 10.1021/acs.analchem.7b04733 (2018).

162. Cha, S. & Yeung, E. S. Colloidal graphite-assisted laser desorption/ionization mass spectrometry and MSn of small molecules. 1. Imaging of cerebrosides directly from rat brain tissue. *Anal. Chem.* **79,** 2373–2385; 10.1021/ac062251h (2007).

163. Qian, K. *et al.* Laser engineered graphene paper for mass spectrometry imaging. *Scientific reports* **3,** 1415; 10.1038/srep01415 (2013).

164. Rainer, M., Qureshi, M. N. & Bonn, G. K. Matrix-free and material-enhanced laser desorption/ionization mass spectrometry for the analysis of low molecular weight compounds. *Anal Bioanal Chem* **400,** 2281–2288; 10.1007/s00216-010-4138-1 (2011).

165. Hua, L., Chen, J., Ge, L. & Tan, S. N. Silver nanoparticles as matrix for laser desorption/ionization mass spectrometry of peptides. *J Nanopart Res* **9,** 1133–1138; 10.1007/s11051-007-9244-4 (2007).

166. Su, C.-L. & Tseng, W.-L. Gold nanoparticles as assisted matrix for determining neutral small carbohydrates through laser desorption/ionization time-of-flight mass spectrometry. *Anal. Chem.* **79,** 1626–1633; 10.1021/ac061747w (2007).

167. Walker, B. N., Razunguzwa, T., Powell, M., Knochenmuss, R. & Vertes, A. Nanophotonic ion production from silicon microcolumn arrays. *Angewandte Chemie International Edition* **48,** 1669–1672; 10.1002/anie.200805114 (2009).

168. Dale, M. J., Knochenmuss, R. & Zenobi, R. Graphite/Liquid mixed matrices for laser desorption/ionization mass spectrometry. *Anal. Chem.* **68,** 3321–3329; 10.1021/ac960558i (1996).

169. Dong, X., Cheng, J., Li, J. & Wang, Y. Graphene as a novel matrix for the analysis of small molecules by MALDI-TOF MS. *Anal. Chem.* **82,** 6208–6214; 10.1021/ac101022m (2010).

170. Surratt, J. D. *et al.* Chemical composition of secondary organic aerosol formed from the photooxidation of isoprene. *The journal of physical chemistry. A* **110,** 9665–9690; 10.1021/jp061734m (2006).

171. Kalberer, M., Sax, M. & Samburova, V. Molecular size evolution of oligomers in organic aerosols collected in urban atmospheres and generated in a smog chamber. *Environ. Sci. Technol.* **40,** 5917–5922; 10.1021/es0525760 (2006).

172. Rüger, C. P., Sklorz, M., Schwemer, T. & Zimmermann, R. Characterisation of ship diesel primary particulate matter at the molecular level by means of ultra-high-resolution mass spectrometry coupled to laser desorption ionisation--comparison of feed fuel, filter extracts and direct particle measurements. *Anal Bioanal Chem* **407,** 5923–5937; 10.1007/s00216-014-8408-1 (2015).

173. Jaoui, M. *et al.* Formation of secondary organic aerosol from irradiated α -pinene/toluene/NO x mixtures and the effect of isoprene and sulfur dioxide. *J. Geophys. Res.* **113**; 10.1029/2007JD009426 (2008).

174. Ng, E. W. Y., Lam, H. S., Ng, P. C. & Poon, T. C. W. Quantification of citrulline by parallel fragmentation monitoring--a novel method using graphitized carbon nanoparticles and MALDI-TOF/TOF mass spectrometry. *Clinica chimica acta; international journal of clinical chemistry* **420,** 121–127; 10.1016/j.cca.2012.10.039 (2013).

175. Kind, T. *et al.* Identification of small molecules using accurate mass MS/MS search. *Mass spectrometry reviews* **37,** 513–532; 10.1002/mas.21535 (2018).

176. Kune, C. *et al.* Rapid Visualization of Chemically Related Compounds Using Kendrick Mass Defect As a Filter in Mass Spectrometry Imaging. *Anal. Chem.* **91,** 13112–13118; 10.1021/acs.analchem.9b03333 (2019).

177. Erve, J. C. L., Gu, M., Wang, Y., DeMaio, W. & Talaat, R. E. Spectral accuracy of molecular ions in an LTQ/Orbitrap mass spectrometer and implications for elemental composition determination. *J. Am. Soc. Mass Spectrom.* **20,** 2058–2069; 10.1021/jasms.8b03342 (2009).

178. Hinz, K.-P. *et al.* Aerosol single particle composition at the Jungfraujoch. *Journal of Aerosol Science* **36,** 123–145; 10.1016/j.jaerosci.2004.08.001 (2005).

179. Murphy, D. M., Middlebrook, A. M. & Warshawsky, M. Cluster Analysis of Data from the Particle Analysis by Laser Mass Spectrometry (PALMS) Instrument. *Aerosol Science and Technology* **37,** 382–391; 10.1080/02786820300971 (2003).

180. Schmidt, S. *et al.* Online single particle analysis of ice particle residuals from mountain-top mixed-phase clouds using laboratory derived particle type assignment. *Atmos. Chem. Phys.* **17,** 575–594; 10.5194/acp-17-575-2017 (2017).

181. Rebotier, T. P. & Prather, K. A. Aerosol time-of-flight mass spectrometry data analysis: a benchmark of clustering algorithms. *Analytica Chimica Acta* **585,** 38–54; 10.1016/j.aca.2006.12.009 (2007).

182. Hinz, K.-P. & Spengler, B. Instrumentation, data evaluation and quantification in on-line aerosol mass spectrometry. *Journal of mass spectrometry : JMS* **42,** 843–860; 10.1002/jms.1262 (2007).

183. Song, X.-H., Hopke, P. K., Fergenson, D. P. & Prather, K. A. Classification of Single Particles Analyzed by ATOFMS Using an Artificial Neural Network, ART-2A. *Anal. Chem.* **71,** 860–865; 10.1021/ac9809682 (1999).

184. Roth, A. *et al.* Aerosol properties, source identification, and cloud processing in orographic clouds measured by single particle mass spectrometry on a central European mountain site during HCCT-2010. *Atmos. Chem. Phys.* **16,** 505–524; 10.5194/acp-16-505-2016 (2016).

185. Li, J. & Endo, Y. Fuzzy c-Means with Improved Particle Swarm Optimization. In *2020 IEEE International Conference on Fuzzy Systems (FUZZ-IEEE). 2020 conference proceedings* (IEEE, Piscataway, NJ, 2020), pp. 1–8.

186. Hinz, K.-P., Erdmann, N., Grüning, C. & Spengler, B. Comparative parallel characterization of particle populations with two mass spectrometric systems LAMPAS 2 and SPASS. *International Journal of Mass Spectrometry* **258,** 151–166; 10.1016/j.ijms.2006.09.008 (2006).

187. Azar, A. T., El-Said, S. A. & Hassanien, A. E. Fuzzy and hard clustering analysis for thyroid disease. *Computer Methods and Programs in Biomedicine* **111,** 1–16; 10.1016/j.cmpb.2013.01.002 (2013).

188. Hang, G., Zhang, D., Ren, J. & Hu, C. A Hierarchical Clustering Algorithm Based on K-Means with Constraints. In *Fourth International Conference on Innovative Computing, Information and Control. ICICIC-2009, December 7-9, 2009, Kaohsiung City, Taiwan* (IEEE Computer Society; IEEE, Los Alamitos, Calif., Piscataway, N.J., 2009), pp. 1479–1482.

189. Zhao, W., Hopke, P. K. & Prather, K. A. Comparison of two cluster analysis methods using single particle mass spectra. *Atmospheric Environment* **42,** 881–892; 10.1016/j.atmosenv.2007.10.024 (2008).

190. Bhave, P. V., Fergenson, D. P., Prather, K. A. & Cass, G. R. Source apportionment of fine particulate matter by clustering single-particle data: tests of receptor model accuracy. *Environ. Sci. Technol.* **35,** 2060–2072; 10.1021/es0017413 (2001).

191. Foss, A. H., Markatou, M. & Ray, B. Distance Metrics and Clustering Methods for Mixed-type Data. *International Statistical Review* **87,** 80–109; 10.1111/insr.12274 (2019).

192. Kapil, S. & Chawla, M. Performance evaluation of K-means clustering algorithm with various distance metrics. In *First IEEE International Conference on Power Electronics, Intelligent Control and Energy Systems (IPEICES 2016). July 4-6, 2016* (IEEE, [Piscataway, New Jersey], 2016), pp. 1–4.

193. Izakian, H. & Abraham, A. Fuzzy C-means and fuzzy swarm for fuzzy clustering problem. *Expert Systems with Applications* **38,** 1835–1838; 10.1016/j.eswa.2010.07.112 (2011).

194. Jones, E. A., Deininger, S.-O., Hogendoorn, P. C. W., Deelder, A. M. & McDonnell, L. A. Imaging mass spectrometry statistical analysis. *Journal of Proteomics* **75,** 4962–4989; 10.1016/j.jprot.2012.06.014 (2012).

195. Alexandrov, T. MALDI imaging mass spectrometry: statistical data analysis and current computational challenges. *BMC Bioinformatics* **13 Suppl 16,** S11; 10.1186/1471-2105-13-S16-S11 (2012).

196. Spengler, B. Mass spectrometry imaging of biomolecular information. *Anal. Chem.* **87,** 64–82; 10.1021/ac504543v (2015).

197. Khamehgir-Silz, P. *et al.* Strategy for marker-based differentiation of pro- and anti-inflammatory macrophages using matrix-assisted laser desorption/ionization mass spectrometry imaging. *The Analyst* **143,** 4273–4282; 10.1039/c8an00659h (2018).

198. Righetti, L. *et al.* Unveiling the spatial distribution of aflatoxin B1 and plant defense metabolites in maize using AP-SMALDI mass spectrometry imaging. *The Plant Journal* **106,** 185–199; 10.1111/tpj.15158 (2021).

199. Albrecht, B. A. Aerosols, cloud microphysics, and fractional cloudiness. *Science (New York, N.Y.)* **245,** 1227–1230; 10.1126/science.245.4923.1227 (1989).

200. Schmale, J. *et al.* Long-term cloud condensation nuclei number concentration, particle number size distribution and chemical composition measurements at regionally representative observatories. *Atmos. Chem. Phys.* **18,** 2853–2881; 10.5194/acp-18-2853-2018 (2018).

201. Che, H. *et al.* Aerosol optical properties and direct radiative forcing based on measurements from the China Aerosol Remote Sensing Network (CARSNET) in eastern China. *Atmos. Chem. Phys.* **18,** 405–425; 10.5194/acp-18-405-2018 (2018).

202. Charlson, R. J., LANGNER, J., RODHE, H., LEOVY, C. B. & WARREN, S. G. Perturbation of the northern hemisphere radiative balance by backscattering from anthropogenic sulfate aerosols*. *Tellus A* **43,** 152–163; 10.1034/j.1600-0870.1991.00013.x (1991).

203. Bauer, S. E. *et al.* Do sulfate and nitrate coatings on mineral dust have important effects on radiative properties and climate modeling? *J. Geophys. Res.* **112**; 10.1029/2005JD006977 (2007).

204. Sokolik, I. N. & Toon, O. B. Incorporation of mineralogical composition into models of the radiative properties of mineral aerosol from UV to IR wavelengths. *J. Geophys. Res.* **104,** 9423–9444; 10.1029/1998JD200048 (1999).

205. Li, W. J. & Shao, L. Y. Observation of nitrate coatings on atmospheric mineral dust particles. *Atmos. Chem. Phys.* **9,** 1863–1871; 10.5194/acp-9-1863-2009 (2009).

206. Sokolik, I. N. & Toon, O. B. Direct radiative forcing by anthropogenic airborne mineral aerosols. *Nature* **381,** 681–683; 10.1038/381681a0 (1996).

207. Yasunari, T. J. *et al.* Influence of dust and black carbon on the snow albedo in the NASA Goddard Earth Observing System version 5 land surface model. *J. Geophys. Res.* **116**; 10.1029/2010JD014861 (2011).

208. Painter, T. H., Bryant, A. C. & Skiles, S. M. Radiative forcing by light absorbing impurities in snow from MODIS surface reflectance data. *Geophys. Res. Lett.* **39,** n/a-n/a; 10.1029/2012GL052457 (2012).

209. Rémy, S. *et al.* Feedbacks of dust and boundary layer meteorology during a dust storm in the eastern Mediterranean. *Atmos. Chem. Phys.* **15,** 12909–12933; 10.5194/acp-15-12909-2015 (2015).

210. Gautam, R., Hsu, N. C., Lau, W. K.-M. & Yasunari, T. J. Satellite observations of desert dust-induced Himalayan snow darkening. *Geophys. Res. Lett.* **40,** 988–993; 10.1002/grl.50226 (2013).

211. Krueger, B. J., Grassian, V. H., Cowin, J. P. & Laskin, A. Heterogeneous chemistry of individual mineral dust particles from different dust source regions: the importance of particle mineralogy. *Atmospheric Environment* **38,** 6253–6261; 10.1016/j.atmosenv.2004.07.010 (2004).

212. Cozic, J. *et al.* Scavenging of black carbon in mixed phase clouds at the high alpine site Jungfraujoch. *Atmos. Chem. Phys.* **7,** 1797–1807; 10.5194/acp-7-1797-2007 (2007).

213. Kamphus, M. *et al.* Chemical composition of ambient aerosol, ice residues and cloud droplet residues in mixed-phase clouds: single particle analysis during the Cloud and Aerosol Characterization Experiment (CLACE 6). *Atmos. Chem. Phys.* **10,** 8077–8095; 10.5194/acp-10-8077-2010 (2010).

214. Henning, S. Seasonal variation of water-soluble ions of the aerosol at the high-alpine site Jungfraujoch (3580 m asl). *J. Geophys. Res.* **108**; 10.1029/2002JD002439 (2003).

215. Barth, C., Hinz, K.-P. & Spengler, B. On-line and off-line analysis of particles from rock, sediment, sand, snow water and atmospheric air at the Jungfraujoch site, using single-particle laser mass spectrometry. *Aerosol Science and Technology* **55,** 552–570; 10.1080/02786826.2021.1873236 (2021).

216. Lelieveld, J. *et al.* Cardiovascular disease burden from ambient air pollution in Europe reassessed using novel hazard ratio functions. *European heart journal* **40,** 1590–1596; 10.1093/eurheartj/ehz135 (2019).

217. *WHO Global Ambient Air Quality Database. Update 2018* (Geneva, 2018).

218. Li, W. & Sun, S. Air pollution driving factors analysis: Evidence from economically developed area in China. *Environ. Prog. Sustainable Energy* **35,** 1231–1239; 10.1002/ep.12316 (2016).

219. Tao, J. *et al.* PM 2.5 pollution in a megacity of southwest China: source apportionment and implication. *Atmos. Chem. Phys.* **14,** 8679–8699; 10.5194/acp-14-8679-2014 (2014).

220. Rodríguez, S. *et al.* Transport of desert dust mixed with North African industrial pollutants in the subtropical Saharan air layer. *Atmos. Chem. Phys.* **11,** 6663–6685; 10.5194/acp-11-6663-2011 (2011).

221. Yiu-chung Chan *et al.* Using multiple type composition data and wind data in PMF analysis to apportion and locate sources of air pollutants. *1352-2310* (2011).

222. *Global Air Quality Database App: App for exploring air quality in countries. WHO Global Air Quality Database (update 2018) edition.* 1st ed. (Geneva, 2018).

223. Barth, C., Hinz, K.-P. & Spengler, B. Particle characterization and quantification of organic and inorganic compounds from Chinese and Iranian aerosol filter samples using scanning laser desorption/ionization mass spectrometry. *Anal Bioanal Chem* **414,** 7223–7241; 10.1007/s00216-022-04275-1 (2022).

224. Kiss, G. Sample preparation of atmospheric aerosol for the determination of carbonyl compounds. *Talanta* **48,** 755–762; 10.1016/S0039-9140(98)00092-7 (1999).

225. Aldabe, J., Santamaría, C., Elustondo, D., Lasheras, E. & Santamaría, J. M. Application of microwave digestion and ICP-MS to simultaneous analysis of major and trace elements in

aerosol samples collected on quartz filters. *Anal. Methods* **5,** 554–559; 10.1039/C2AY25724F (2013).

226. Willis, P., Jaloszynski, J. & Artaev, V. Improving duty cycle in the Folded Flight Path high-resolution time-of-flight mass spectrometer. *International Journal of Mass Spectrometry* **459,** 116467; 10.1016/j.ijms.2020.116467 (2021).

227. Michalski, A. *et al.* Ultra high resolution linear ion trap Orbitrap mass spectrometer (Orbitrap Elite) facilitates top down LC MS/MS and versatile peptide fragmentation modes. *Molecular & cellular proteomics : MCP* **11,** O111.013698; 10.1074/mcp.O111.013698 (2012).

228. Senko, M. W. *et al.* Novel Parallelized Quadrupole/Linear Ion Trap/Orbitrap Tribrid Mass Spectrometer Improving Proteome Coverage and Peptide Identification Rates. *Anal. Chem.* **85,** 11710–11714; 10.1021/ac403115c (2013).

229. Plaß, W. R., Dickel, T. & Scheidenberger, C. Multiple-reflection time-of-flight mass spectrometry. *International Journal of Mass Spectrometry* **349-350,** 134–144; 10.1016/j.ijms.2013.06.005 (2013).

230. Ijaz, A. *et al.* Molecular and physical composition of tar balls in wildfire smoke: an investigation with complementary ionisation methods and 15-Tesla FT-ICR mass spectrometry. *Environ. Sci.: Atmos.* **3,** 1552–1562; 10.1039/D3EA00085K (2023).

231. He, M. *et al.* Dual-Polarity Ion Trap Mass Spectrometry: Dynamic Monitoring and Controlling Gas-phase Ion-Ion Reactions. *J. Am. Soc. Mass Spectrom.* **28,** 1262–1270; 10.1007/s13361-016-1504-z (2017).

232. Arevalo, R. *et al.* Laser desorption mass spectrometry with an Orbitrap analyser for in situ astrobiology. *Nat Astron* **7,** 359–365; 10.1038/s41550-022-01866-x (2023).

3 Publication 1

On-line and off-line analysis of particles from rock, sediment, sand, snow water and atmospheric air at the Jungfraujoch site, using single-particle laser mass spectrometry

Christof Barth, Klaus-Peter Hinz, and Bernhard Spengler

Institute of Inorganic and Analytical Chemistry, Justus Liebig University Giessen, Giessen, Germany

Aerosol Science and Technology **2021**, 55 (5), pp 552-570

DOI: 10.1080/02786826.2021.1873236

AEROSOL SCIENCE AND TECHNOLOGY
2021, VOL. 55, NO. 5, 552–570
https://doi.org/10.1080/02786826.2021.1873236

On-line and off-line analysis of particles from rock, sediment, sand, snow water and atmospheric air at the Jungfraujoch site, using single-particle laser mass spectrometry

Christof Barth, Klaus-Peter Hinz, and Bernhard Spengler

Institute of Inorganic and Analytical Chemistry, Justus Liebig University Giessen, Giessen, Germany

ABSTRACT

The chemical composition of aerosol particles strongly influences the earth's climate, including their effects as sediments reducing the reflectivity of snow surfaces. Source apportionment and transportation pathways of such particles help to assess their contribution to regional surface-radiative heating. The chemical composition of particles in the free troposphere was studied at the Jungfraujoch (3580 m asl) in the Swiss Alps, using the laser mass spectrometer LAMPAS 2 during the CLACE-1 campaign. Statistical methods and lab measurements of reference particles were used to investigate the source and aging of field-measured particles. Desert sand, igneous rock and river sediment were used as model systems to differentiate between aged and non-aged atmospheric particles. Dried-up snow-water particles showed a particle composition typically found at the measurement site, largely influenced by carbonaceous and organic particles from local sources. During on-line measurements between 17 and 24 March 2000, sand particles from two sandstorm events were a significant source for less-aged mineral particles. Our results show that desert-sand particles can be transported over long distances and that silicate-rich particles in particular are only slightly altered in the atmosphere. We assume that both, the carbonaceous fraction as well as the fresh mineral particles lead to a warming effect at the measurement site due to their intrinsic properties of low solubility and strong light absorption, decreasing the surface reflectivity of the Alpine snow layer. The results allow for a better assessment of environmental influences and particles' impact on the local climate in the Alpine region at the Jungfraujoch.

ARTICLE HISTORY
Received 28 April 2020
Accepted 23 December 2020

EDITOR
Jim Smith

1. Introduction

The influence of different kinds of aerosol on the earth's climate was studied extensively in a large number of publications in recent years (Allen, Landuyt, and Rumbold 2016; Isaksen et al. 2009; Koch et al. 2009; Nabat et al. 2015; Shindell et al. 2009) and in the past (Albrecht 1989; Charlson et al. 1991; Haywood and Shine 1995; Twomey 1977). Correct interpretation of light scattering versus absorption of certain types of aerosols will lead to a better understanding and prediction of the future climate evolution. Whether a certain aerosol has a warming or a cooling effect on the atmosphere, depends on various physical and chemical parameters as for example particle size, chemical composition, site of action and water content (Kandler et al. 2009; Tegen, Lacis, and Fung 1996). Usually a distinction is made between strongly hydrophilic particles consisting of easily soluble components (sulfates, nitrates, salts) and hydrophobic particles like black carbon (BC) or organic matter (Andreae and Gelencser 2006). The former ones are associated with climate cooling due to their light scattering abilities (Charlson et al. 1991), BC with warming by absorption of radiation in a broad spectral range (Hansen and Nazarenko 2004; Ramanathan and Carmichael 2008). Aggregated mineral-dust particles are associated with light-absorbing abilities as well (Sokolik and Toon 1999).

The strong light-absorbing properties of aerosol particles were found to play an important role in places where the reflectivity of the earth's surface is very high (Gautam et al. 2013). In the alpine region, for example, the white snow with its high albedo is partly covered by aggregated mineral dust particles as well as BC, further enhancing the warming effect of those particles by

CONTACT Bernhard Spengler Bernhard.spengler@anorg.chemie.uni-giessen.de Institute of Inorganic and Analytical Chemistry, Justus Liebig University Giessen, Heinrich-Buff-Ring 17, Giessen, 35392 Germany.

Supplemental data for this article is available online at https://doi.org/10.1080/02786826.2021.1873236.

reduction of snow surface reflectivity. This effect is well known for BC, but in case of mineral dust strongly depends on the solubility and hence chemical processing of these particles before deposition (Ming et al. 2008). The differentiation between fresh and aged mineral particles is therefore essential for assessing the influence of the particles on the regional snow albedo. In this context, the role of mineral dust is often neglected, but it has been shown to be an important contributor to the reduced surface reflectivity (Gautam et al. 2013; Liou et al. 2014). The lower absorption of the mineral dust compared to BC is thereby compensated by its larger deposition volumes, which play a particularly important role in the vicinity of large mineral dust sources. Especially the influence of regional particle sources and less-aged particles that were fast transported from a greater distance is very important and has still not been fully clarified (Henning et al. 2003). Such effects can be studied notably well in remote places where low particle concentrations are expected and where urban and rural influences can be well assessed. Many measurements on the Jungfraujoch in the Swiss Alps in recent years show that this site is particularly suitable for this purpose (Cozic et al. 2008; Henning et al. 2003; Hinz et al. 2005).

Various off-line analytical methods have been used for determination of the chemical composition of aerosol particles. Such methods are, for example, atomic absorption spectroscopy (AAS), proton-induced x-ray emission (PIXE) (Matschullat et al. 2000), ion chromatography (Henning et al. 2003) and gas-chromatography coupled with mass spectrometry (GC-MS) (Zheng et al. 2005). A prerequisite for all these methods is the collection of particles on filters or by means of impactors. The analysis of the filter samples often allows a quantitative statement about the overall chemical composition of the particle population at the sampling location. However, differentiating between the individual particle sources using these methods is very challenging, and it is still not possible to prevent changes in the particles during sampling and storage. In order to avoid these disadvantages, it is necessary to measure the particles at the place of their origin. On-line mass spectrometric methods are particularly suitable for this. There is only a small number of such techniques available, including multiple- and single-particle aerosol mass spectrometry (MPMS and SPMS) (Hinz and Spengler 2007).

It is particularly difficult to differentiate between externally and internally mixed particles when particle ensemble measurements are used, as in the case of MPMS. Although MPMS allows to quantitatively determine the chemical composition of particles and to identify certain particle sources by Positive Matrix Factorization (PMF), the results are based on many parameters and vary depending on the interpretation of the initially determined factors (Ulbrich et al. 2009). Another prerequisite for a reliable determination of particle sources using PMF is the availability of a sufficiently large data set. It is therefore important to be able to measure individual particles separately. Single-particle aerosol mass spectrometry offers optimal conditions for this, as individual particles are vaporized, ionized and detected one after another. Even a small number of measured particles makes it possible to draw conclusions about the origin of the particles and environment to which these particles were exposed (Hinz et al. 1999).

The analysis of single particles is often ambiguous, if only one ion polarity is monitored. A low mass resolution, which is typical for such devices, can lead to overlapping signals, making it difficult to correctly assign the detected ions. Bipolar time-of-flight mass spectrometry, detecting ions of both polarities from the same particle, therefore has been found to be crucial for correct assignment of signals. (Hinz, Kaufmann, and Spengler 1996). On-line measurement in bipolar single-particle mass spectrometry is a powerful tool for describing the native state of atmospheric particles. We report on the differentiation of fresh and aged internally mixed particles, based on comparing ion-abundance ratios in mass spectra of online-measured airborne particles at the Jungfraujoch with those in mass spectra of representative particles collected from locations that are expected to be important particle sources at the measurement site. Their chemical composition, origin and aging behavior are important parameters in this context and were therefore investigated for the isolated place of the Jungfraujoch. The results of this study should provide a deeper insight into the influence of regional and less-aged mineral particles on the surface reflectivity of snow layers in such remote regions.

2. Methodology

2.1. Samples collection and handling

Three different types of particles where chosen as model systems in laboratory measurements: Alpine rock stone, Morocco desert sand and Rhine river sediment. Each of these populations represents a possible class of mineral atmospheric aerosol particles, fresh mineral dust in case of the sand or eroded rock in case of Aarmassif granite. The sediment particles demonstrate a certain evolution of eroded mineral particles processed by anthropogenic and natural influences.

A fourth type of particles was also investigated. Those particles were retrieved from dried-up snow water, and it is expected that they reflect the particle composition in the surrounding atmosphere over a longer period of time. These particles precipitate during snowfall and accumulate in different snow layers. It is expected that most mineral atmospheric particle populations measured at the Jungfraujoch site are to some extent affected by these mineral particle classes or in the case of snow water residues reflect similar chemical features.

Snow and rock stone samples were collected at the top region of the high-alpine site Jungfraujoch in the Swiss Alps (3580 m asl) on 27 March 2000, during the field campaign "Cloud and Aerosol Characterization Experiment (CLACE-1)." Sampling spots for the snow samples were located at the exit area of the station facing the glacier while rock was sampled at the Jochplateau. Fresh snow was obtained from the top (0–30 cm) and pressed snow (30–45 cm) from deeper snow layers and molten to yield a total volume of more than 4 liters of water. The water was stored in plastic bottles at 4 °C in a refrigerator. For aerosol measurements, about 1.5 liters of snow water were slowly evaporated to dryness, and the remaining residues were ground with an agate mortar. The rock stone samples were stored in the refrigerator at 4 °C. For measurement, small pieces ($<1\,cm^3$) were dried in a desiccator overnight and ground with a mortar to yield a fine powder.

Rhine sediment was sampled in 2011 near Lörrach in Germany, dried and size selected. The inhomogeneous powder with particle sizes smaller than 2 mm was then ground with a ball mill to obtain particle sizes below 10 µm, which is in the measurement range of the LAMPAS 2 (Laser Mass Analyzer for Particles in the Airborne State) instrument (Trimborn, Hinz, and Spengler 2000).

Morocco sand was sampled in February 2005 near Laayoune in Morocco and treated the same way as the rock samples. Measurement of the finely dispersed powders from rock, sand and snow water residues was carried out with the LAMPAS 3 mass spectrometer (Hinz et al. 2011) in the laboratory. The powders from rock, sand and river sediment were additionally microwave digested with aqua regia and measured by inductively coupled plasma - optical emission spectrometry (ICP-OES).

2.2. Instrumentation

Direct analysis of single tropospheric aerosol particles was carried out during the field campaign CLACE-1 on ten days in March 2000 at the Jungfraujoch with the LAMPAS 2 instrument. A detailed description of the instrument can be found elsewhere (Trimborn, Hinz, and Spengler 2000). An overview of the whole dataset was published earlier (Hinz et al. 2005). The measured spectra were revised, partly recalibrated in greater detail, and crowded spectra containing saturated ion signals were filtered out. Only for 17, 18 and 22 till 24 March, the quality and number of spectra were sufficiently high for statistically reliable evaluation. Vacuum aerodynamic particle size was determined by calibrating the instrument with polystyrene latex spheres with diameters between 0.2 µm and 5.7 µm. Single-particle analyses of rock, sand and dried water samples were performed in the laboratory with an improved version of the previously described instrument. The LAMPAS 3 instrument was developed with reduced instrumental size and optimized for user-friendly long-term operation. A sketch of the instrument is shown in Figure S1. The dry powders were dispersed and transferred into the LAMPAS 3 instrument through a differentially pumped inlet system, consisting of a nozzle, a skimmer and an orifice. Particles in the size range between 0.2 and 10 µm were optically detected by two continuous cw-laser beams ($\lambda = 532$ nm) inside the main chamber of the mass spectrometer. Particle sizes were determined based on their size-dependent velocities. Afterwards, an actively triggered 337 nm pulsed UV laser evaporated and ionized the detected particles. The positively and negatively charged ions were then simultaneously analyzed using a bipolar time-of-flight mass spectrometer at a mass resolution ($M/\Delta M$) of about 300 for both polarities. LAMPAS 2 and 3 are comparable in terms of particle detection, ionization and ion separation and show the same spectral quality and intensities. The main difference is the more compact design of LAMPAS 3.

An ICP-OES instrument (Varian 720ES) was used for the quantification of aqua-regia-soluble components in rock, sand and river sediment. The amount of snow water residue was too small for an ICP-OES analysis. Microwave digestion was carried out twice for each sample (0.3 g/50 ml). Three repeated measurements (technical replicates) per sample were performed and the mean values were calculated. The values of both digestions were also averaged. Reference samples were measured at the beginning and end of each run, 18 samples were measured in total. Calibration was performed using several dilutions of an ICP multi-element standard (Carl Roth, Karlsruhe), with the following concentrations: As, Cd, Co, Cr, Cu, Na, Ni, Pb, S, Zn = 0.1, 0.5, 1.0 and 5 mg/l; K, Ca = 51.1, 60.5, 101 and 155 mg/l; Fe, Al =

101, 110.5, 151 and 205 mg/l; Mg, Mn = 1, 5, 11 and 55 mg/l; $P = 1$, 5, 10 and 100 mg/l.

2.3. Data evaluation

For data evaluation and classification of particles, a hierarchical clustering algorithm (HCA) was used (Ward 1963). This algorithm is part of the software package Perseus (Version 1.5.3.0) from the Max Planck Institute of Biochemistry (MPIB, Martinsried, Germany) (Tyanova et al. 2016). For HCA, predefined clusters are gradually combined into larger and larger clusters based on their similarity. This merging is visualized by a dendrogram (tree diagram), where the length of the branches until the merging reflects the similarity of the clusters. Pre-processing of data for finding initial cluster centers was done by a k-means algorithm. The iterative clustering process sorts mass spectra with similar composition into classes. 50 start clusters were created by the k-means algorithm to account for even rare clusters. We used a Pearson correlation distance metric for the HCA clustering. Euclidean distance was tested likewise but was found to join similar clusters only in a very late stage of the HCA (see Figure S3). Fuzzy clustering as an alternative clustering approach allows to assign a membership degree to each spectrum and is therefore more robust against false assignments, but due to its non-discrete nature it builds up artificial spectra patterns to which each spectrum participates according to its membership degree. To build up a joining tree like in HCA, we rather wanted to use mean spectra patterns, where each spectrum contributes equally. This allowed us to distinguish more strictly between the groups. The clustering quality is comparable between fuzzy clustering and k-means, while k-means performs better in case of speed and computing power (Azar, El-Said, and Hassanien 2013).

We found that highly intense signals of potassium and sodium are the dominating factors for the cluster separation. Both signals show very low dependence on the actual content of sodium or potassium in the particles but rather appear as ubiquitous background signals. Even more, the high intensity (often not completely resolved within the dynamic range of the detector) of both signals deplete and distort the remaining signals in the spectra. This effect is typical for laser desorption ionization (LDI) MS of aerosol particles due to the ionic nature of potassium and sodium in various compounds (Hinz et al. 2005). We therefore removed the potassium and sodium signals from all spectra, followed by normalization to the total ion count (TIC) of the remaining signals. The intensity ratios of signals in positive- and negative-ion spectra, as used for statistical evaluation, remained the same in our approach since no scaling (logarithmic, square root) was applied to the spectra.

The approach we present here is different from common methods, which are, for example, based on the determination of particle classes using the entire mass spectrum and leading to a large number of clusters and a suppression of less abundant spectra types. The effort of a manual separation and sorting after such clustering is high, compared to statistical identification of particle classes based on significant ion species (Kamphus et al. 2010; Schmidt et al. 2017). Most classification approaches rely on the idea that all particles exhibit signals of marker ions that belong primarily to one particle class, e.g., Mg^+, Al^+, and Fe^+ for mineral particles. These procedures are well suited for the identification of different kinds of particles in one dataset. To identify for example mineral particles only by using such marker signals in an aged population, based on representative mineral particle spectra patterns, is considerably more difficult because of the changes, the freshly emitted particles undergo in the atmosphere. For comparison of different datasets consisting of fresh and aged particles, the above methods would lead to a sharp separation into two groups. The prediction of the source for an atmospherically aged particle is not possible by only using the unmodified patterns of the fresh particles for a comparison.

The differentiation of aged from non-aged particles and their assignment to different particle sources that we provide here, involves a multi-step process: first, the identification of descriptive ions for each model population and second, the identification of signals associated with atmospheric aging in the online-measured single-particle spectra and artificial aging of each model system by these signals. The sum spectra of the model systems were thus recalculated with respect to the identified aging markers. For this process it was assumed that all mineral particles age at the same rate and form the same main chemical components. In our case, however, the intensity ratios of the other signals after simulated aging were of particular importance, as the classification was carried out using only descriptive ion signals specific to each mineral and not taking into account those identified as aging markers. Our aim was not to generate spectra as close to reality as possible, but to generate spectra that allow the classification of atmospherically aged particles using our model systems.

Finally, the HCA of aged and unaged particle populations for classification was carried out. As mentioned before, we used only descriptive ion signals for separation of the aged populations, while for HCA of unaged populations, additional signals were selected. A detailed workflow for selecting descriptive ions, artificial aging and the application of the HCA algorithm is shown in Figure S2.

In our study, we computed 180 and 72 h back trajectories for two time periods of interest, using the Hybrid Single-Particle Lagrangian Integrated Trajectory (HYSPLIT) model (Rolph, Stein, and Stunder 2017; Stein et al. 2015). We used the meteorological data from the National Centers for Environmental Prediction (NCEP) and the National Center for Atmospheric Research (NCAR) called NCEP/NCAR Reanalysis. HYSPLIT generated back trajectories for air masses arriving at the Jungfraujoch research station (3580 m a.s.l., 46°33N, 7°59E) every two hours from 17 March (0900 UTC) until 18 March (2100 UTC), from 21 March (2300 UTC) until 23 March (2300 UTC) and from 24 March (0600 UTC) until 24 March (1800 UTC), which corresponds roughly to both Sahara-desert storm events during the measurement period.

3. Results and discussion

3.1. Chemical signatures of rock, sand, river sediment, and snow water residues by SPMS and offline ICP-OES methods

Summed spectra patterns from rock, sand, river sediment and snow water residues are shown in Figure 1. A total number of 307, 452, 660, and 265 spectra were evaluated from rock, sand, river sediment, and snow water, respectively.

Using sum spectra from a sufficient number of single particle spectra is necessary because of the high inhomogeneity of mineral species. The following evaluation of our data is based on the assumption that all individual particles are completely evaporated/ablated within the mass spectrometer, which is not necessarily the case (Cai, Zelenyuk, and Imre 2006). Typical recurring signal patterns of Na^+ and K^+ (m/z 23 and 39) were found in all particle populations in

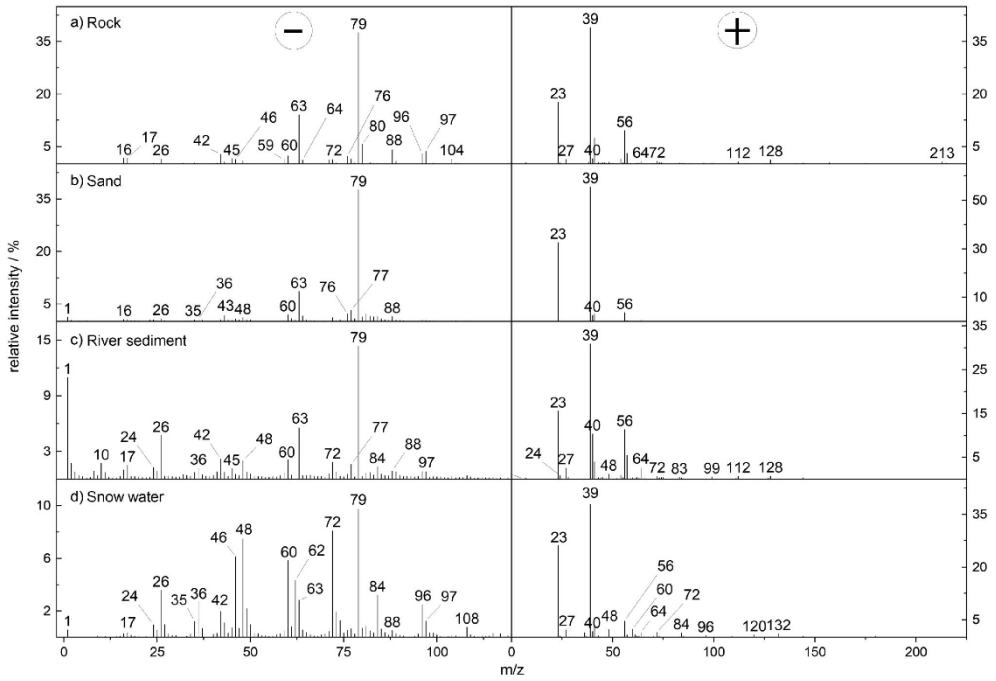

Figure 1. Sum spectra measured with LAMPAS 3 from (a) ground rock stone from the top region of the Jungfraujoch (307 spectra), (b) ground Morocco desert sand (452 spectra), (c) ground river sediment from Rhine river in Germany (660 spectra), and (d) dried snow water residues from the top region of the Jungfraujoch (265 spectra).

Table 1. Comparison between relative intensities (TIC normalized) taken from sum spectra of different mineral particle populations measured by LAMPAS, and aqua-regia-digested samples measured by ICP-OES. Assignments were made based on typical ions found for the respective signals (masses in brackets) in SPMS lab and field studies (Hinz et al. 2006; Murphy et al. 2006).

Population	LAMPAS (summed signal intensity) / %									
	PO_2^- (63), PO_3^- (79)	FeO_2^- (88), FeO_3^- (104)	SiO_3^- (76)	Ca (40)	O^- (16), OH^- (17)	Cl^- (35)	C_3^- (36), C_4^- (48), C_6^- (72), C_7^- (84)	NO_2^- (46), NO_3^- (62)	HSO_4^- (97)	K^+ (39)
Rock (lab)	51.7	5.6	2.2	1.6	3.4	0.3	2.8	1.5	3.7	39.0
Sand (lab)	46.2	1.7	2.2	2.7	1.4	0.6	4.3	1.2	0.3	55.6
Sediment (lab)	19.9	1.2	0.6	10.4	2.5	0.7	6.4	1.0	0.8	30.9
Snow (lab)	12.6	0.6	0.5	1.7	0.6	1.2	21.5	10.5	1.2	37.9
Jungfraujoch (field)	4.7	2.0	3.7	2.9	9.5	4.9	4.5	17.3	1.3	23.0
	ICP-OES / *wt*%									
	P	Fe		Ca					S	K
Rock	< 0.1	3.6	–	0.3	–	–	–	–	0.4	0.3
Sand	< 0.1	0.8	–	21.6	–	–	–	–	< 0.1	0.1
Sediment	< 0.1	1.3	–	10.4	–	–	–	–	< 0.1	0.4

exceptionally high intensities. The reasons for this were discussed above (Section 2.3). In case of ground rock stone, any modification of the particles prior to the measurement could be excluded. Besides sodium and potassium ions, positive-ion mass spectra from rock stone in Figure 1a were mainly characterized by signals of aluminum (*m/z* 27), calcium (*m/z* 40), iron (*m/z* 56 and 112), titanium oxide (*m/z* 64) and iron oxide (*m/z* 72 and 128). Negative-ion mass spectra showed intense signals of PO_2^- at *m/z* 63 and PO_3^- at *m/z* 79, common components of mineral crust particles and attributed to the P_2O_5 structures of apatite (El Asri et al. 2009). Despite the highly intense signals of PO_2^- and PO_3^- in the mass spectra, the amount of phosphorus measured by ICP-OES was lower than 0.1 *wt*% in all particle populations (see Table 1). The LDI process obviously supports the generation of phosphate ions in the plume by charge exchange reactions (Reilly et al. 2000).

This means that the formation of phosphate ions through the absorption of electrons in the plume is clearly preferred over the formation of other ions. Silicon oxide ions SiO_2^-, SiO_3^-, $HSiO_3^-$, $Si_2O_2^-$, and $Si_2O_3^-$ (*m/z* 60, 76, 77, 88, and 104) in Figures 1a–b are probably suppressed by this effect, resulting in low signal intensities compared to the expected abundance of silicate (>70 *wt*%) in the mineral populations (Abrecht and Schaltegger 1988).

FeO_2^- (*m/z* 88) and FeO_3^- (*m/z* 104) signals in the rock, sand and sediment spectra show the same trend as the iron content measured by ICP-OES (see Table 1), suggesting iron oxide rather than silicon oxide to be the major source of both signals (Gallavardin, Lohmann, and Cziczo 2008). The signal at m/z 56 was not used for evaluation, because of a possible interference with CaO^+, especially for the sediment particles. Ti_2O^+ and $Ti_2O_2^+$ could be observed at the same *m/z* values as Fe_2^+ and Fe_2O^+ (112 and 128). In rock, both signals most likely represent iron, due to low Ti^+ (*m/z* 48) and TiO^+ (*m/z* 64) signals compared to intense FeO_2^- and FeO_3^- signals. In the river sediment we expect an influence of titanium and iron, due to strong Ti^+ and TiO^+ signals. Both signals were absent in the sand spectra and even Ca^+ at *m/z* 40 was lower than in the river sediment particles, although the mass fraction of calcium in the sand particles is the highest within all mineral populations (Table 1) (Schmidt et al. 2017). The higher Ca^+ signal in the sediment particles is supposed to be a result of a better desorption/ionization yield for calcium in the respective mineral matrix due to an enrichment of chemically persistent TiO_2, which is known to support desorption/ionization due to its high UV absorption (Castro et al. 2008). Reilly et al. showed that the sensitivity for difficult-to-ionize species in matrices that are even more difficult to ionize, is greatly increased (Reilly et al. 2000). Probably this effect also contributes to a significant increase of the calcium signal due to a more complex mineral matrix in the sediment particles.

Other ion species indicating the influence of anthropogenic factors are NO_2^- (*m/z* 46), NO_3^- (*m/z* 62) and carbon cluster ions from C_2^- (*m/z* 24) to C_{15}^- (*m/z* 180), mainly found in the river sediment and snow water populations in Figures 1c–d, respectively. The carbon contents of the four populations were determined from the sum of all signal intensities at *m/z* 36, 48, 72, and 84 in the negative-ion spectra. Wherever possible, ambiguous *m/z* values were not used to determine the carbon content, hence the low number of signals. The higher carbon content of the river sediment and snow water populations reflects an anthropogenic influence that was not found for the rock and sand populations. The total nitrate content

Table 2. Comparison between rock, sand, and river sediment population with all ions shown to be descriptive for the respective population (Hinz et al. 2005; 2006; Schmidt et al. 2017; Shen et al. 2019).

Population	Positive ions (*m/z*)	Negative ions (*m/z*)
Rock	Al (27), Ti / C_4 (48), ^{54}Fe (54), Fe (56), ^{57}Fe (57), FeO (72), Fe_2 / Ti_2O (112), Fe_2O / Ti_2O_2 (128), K_2SO_4 (213)	CNO (42), C_2H_5O / COOH (45), AlO_2 / CH_2COOH (59), MnO (71), SO_3 / HPO_3 (80), FeO_2 / Si_2O_2 (88), SO_4 (96), HSO_4 (97), FeO_3 / Si_2O_3 (104)
Sand	–	C_3N (50), $HSiO_2$ (61), P_2O (78), H_2PO_3 / HSO_3 (81), C_5H_7O (83), C_7 (84), $NaNO_3$ (85)
Sediment	Mg / C_2 (24), Al (27), Ca / MgO (40), Ti / C_4 (48), ^{54}Fe (54), Fe / CaO (56), ^{57}Fe / CaOH (57), TiO / CaC_2 (64), FeO (72), Fe_2 / Ti_2O / Ca_2O_2 (112), Fe_2O / Ti_2O_2 / Ca_2O_3 (128)	C_2 (24), C_2H (25), CN (26), C_3 (36), C_2OH (41), C_4H (49), C_3N (50), AlO_2 / CH_2COOH (59), MnO (71), H_2PO_3 / HSO_3 (81), C_7 (84), $NaNO_3$ (85)

was calculated by the sum of the negatively charged ions at *m/z* 46 and 62. Significantly higher nitrate content was found in the snow water particles in Figure 1d, formed under atmospheric conditions. In the snow layer, no continuous replacement of the water-soluble nitrate salts takes place, in contrast to river sediment particles.

In summary, it is very difficult to differentiate between different mineral samples based on relative intensities of the respective ion species on the basis of LDI MS, as these depend very much on the ionization mechanism and the mineral matrix. Therefore, a statement about the identity of the mineral particles, especially on the basis of abundance in combination with the signal intensities of individual ions, even if they are very low, is more suitable. During our statistical evaluation, we focused more on characteristic signals with high abundance and possibly lower intensity in each population, than on common ones which are less abundant but highly intense.

3.2. Identification of descriptive ions and artificial aging

Statistical evaluation of online-measured single particles is a common method for the characterization of different particle populations within a large dataset (Hinz et al. 2005; Sierau et al. 2014). Here we focus on mineral particles because this was the main particle type measured during the field campaign CLACE-1 with the LAMPAS 2 instrument. To discover different sources of mineral particles in the online data set from CLACE-1, we first identified signals in the lab-measured rock, sand and sediment particles that are descriptive for each population and used only these signals for classification.

3.2.1. Descriptive ions

Signals that were increased or decreased in a model population relative to another model population could be characteristic for the identification of a specific mineral matrix. Table 2 shows descriptive ions for each model population. Because of the natural variability and the ambiguity of a number of *m/z* values, there is a high degree of uncertainty even between mineral particles (Gallavardin, Lohmann, and Cziczo 2008). Signals at m/z 80, 96, and 97 were attributed to SO_3^-, SO_4^-, and HSO_4^- and were found predominately in rock particles. Signals at m/z 79, 95, 96 and 97 may also belong to mineral phosphate (PO_3^-, PO_4^-, HPO_4^-, $H_2PO_4^-$) but correlations based on Pearson's correlation coefficient ρ between m/z 79 and 97 as well as 95 and 96 are poor ($\rho = -0.4$ and $\rho = 0.4$).

The high intensity of m/z 97 in the rock stone particles is very likely caused by the mineral sulfate content as can be seen from the ICP-OES results (see Table 1), while the same signal in the Jungfraujoch sum spectrum may also be a result of atmospheric aging.

For atmospheric particles it is known that the uptake of SO_2 or H_2SO_4 in the outer liquid layer of the particle, which is an irreversible process, leads to an enrichment of SO_4^{2-} in the particles (Song and Carmichael 1999). Our results indicate that the mineralogical sulfate content in atmospheric particles can become dominant, if a large proportion of igneous rock contributes to this population.

There were no characteristic signals found within the positively charged ions and only very few within the negatively charged ions for the sand particle population. Among some very minor signals, only $NaNO3^-$, C_3N^-, $HSiO_2^-$, $H_2PO_3^-/HSO_3^-$, $C_5H_7O^-$, C_7^-, and P_2O^- were found to be significant for this population. This complicates the identification of sand particles within populations of greater diversity such as online-measured particles from different natural and anthropogenic sources.

Rock and river sediment samples shared similar characteristic positive ions while sand and river sediment samples shared similar negative ions. The largest differences between characteristic rock and river sediment signals were found for sulfur oxides and calcium. As the calcium signal is found to be very low in the rock stone particles, the characteristic signals at

m/z 56, 57, 112, and 128 should represent iron, iron oxides or titanium oxides rather than calcium oxides. A unique feature of the rock stone is the signal at *m/z* 213 in the positive-ion spectra. The isotopologue pattern of this signal is similar to that of $K_3SO_4^+$ or $K_3HPO_4^+$ but the mass resolving power of the mass spectrometer is not sufficient for an exact determination. However, correlations between 213 and PO_3^- at *m/z* 79 ($\rho = -0.2$) as well as 213 and SO_4^- at *m/z* 96 ($\rho = 0.7$) suggest the formation of $K_3SO_4^+$. Often it is claimed that the signal at 213 is an indicator for atmospheric aging or biomass burning, but here we found this signal almost exclusively in the unaltered rock particles with a high share of 24% (Sierau et al. 2014; Zauscher et al. 2013). Due to the high content of sulfate in the rock samples, the formation of $K_3SO_4^+$ in the laser plume, from easily accessible ionic components, is very likely. The signal is not significantly enhanced in our atmospheric mineral samples. This example shows that the identification of ion signals, even with only nominal mass resolution, is possible if both polarities are measured simultaneously from one particle.

3.2.2. Characteristic signals indicating the aging of particles

In a second step, signals related to atmospheric aging were identified. Here the rock and sand particles served as a reference standard since no direct aging effects are expected for these populations. Details on the identification of ions related to atmospheric aging and consecutive theoretical aging of sand, rock and sediment spectra can be found in Sect. 2.3 and as detailed workflow in the SI (Section 2).

Ions that were found to play a significant role in atmospheric aging were only found within the negatively charged ions, for example H^- and H_2^-/He^- as a result of a higher water content and acidity in the atmospheric particles after uptake of acidic trace gases. Cl^-, NO_2^-, or NO_3^- are other typical ions found in aged particles. Nitrogen-containing ions, especially the higher oxidized species are the quantitatively most important indicators for aged mineral aerosol particles in polluted air (Hinz et al. 2005; Laskin et al. 2005). The growth rate of nitrate compounds, particularly for particles >2 µm is fast compared to other species such as chloride (Song and Carmichael 1999). The detected nitrate can either be formed by the direct uptake of ammonium nitrate, formed by neutralization of gaseous HNO_3 with NH_3 (Brauer, Koutrakis, and Spengler 1989), or by the conversion of gaseous precursors like NO_2 or N_2O_5 (Russell, Cass, and Seinfeld 1986). Alkaline oxides such as K_2O, Na_2O, or CaO, present in mineral particles, easily form water-soluble alkaline nitrate species. This reaction can also take place with lowly soluble $CaCO_3$. Calcium carbonate reacts to more soluble $Ca(NO_3)_2$ at the presence of HNO_3 (Laskin et al. 2005). The chloride species in aged aerosol particles are expected to be formed mainly at marine boundary layers, where the evaporation of volatile HCl from sea salt particles creates a high HCl concentration environment. In the case of our measurements we expect only a small amount of sea salt particles, but a high amount of mineral dust, which in turn is able to form hygroscopic $CaCl_2$ under these conditions (Tobo et al. 2010).

The reactions above lead to strong differences in hygroscopicity, solubility and light scattering as well as absorption behavior of the reaction products $Ca(NO_3)_2$ or $CaCl_2$ compared to $CaCO_3$. Henning et al. found $CaCO_3$ to be the major compound responsible for high nitrate content in particles > 1 µm after exposure to anthropogenic influences (Henning et al. 2003).

Some species are not expected to be formed during particle transport in the atmosphere but instead are chemically persistent and insoluble, such as Mg^+ from $MgCO_3$, Ti^+, or TiO^+ from TiO_2 and Al^+ from alumosilicates. These ions are more likely enriched in the particles while more soluble components like potassium and sodium salts are washed out. Changes in the signal patterns of these ions were not significant enough, so they were not identified as products of atmospheric aging. As a result, the influence of atmospheric processes is mainly reflected in the spectra of negatively charged ions, particularly by the ratio of nitrate compared to other compounds like for example phosphate, while the signal patterns of positively charged ions differ only slightly between fresh and aged populations. The signals identified above were used for recalculation of the signal patterns in rock and sand spectra in order to prevent those spectra to be classified as distinct groups, statistically separated from the Jungfraujoch atmospheric aerosol spectra. Prior studies with laboratory-aged particles showed very similar changes in the signal patterns, as we got after our theoretical aging approach (Hinz et al. 2006).

3.3. Statistical results from lab and field measurements

The complete data set (3432 spectra) used for the statistical evaluation consists of 2505 atmospheric single-

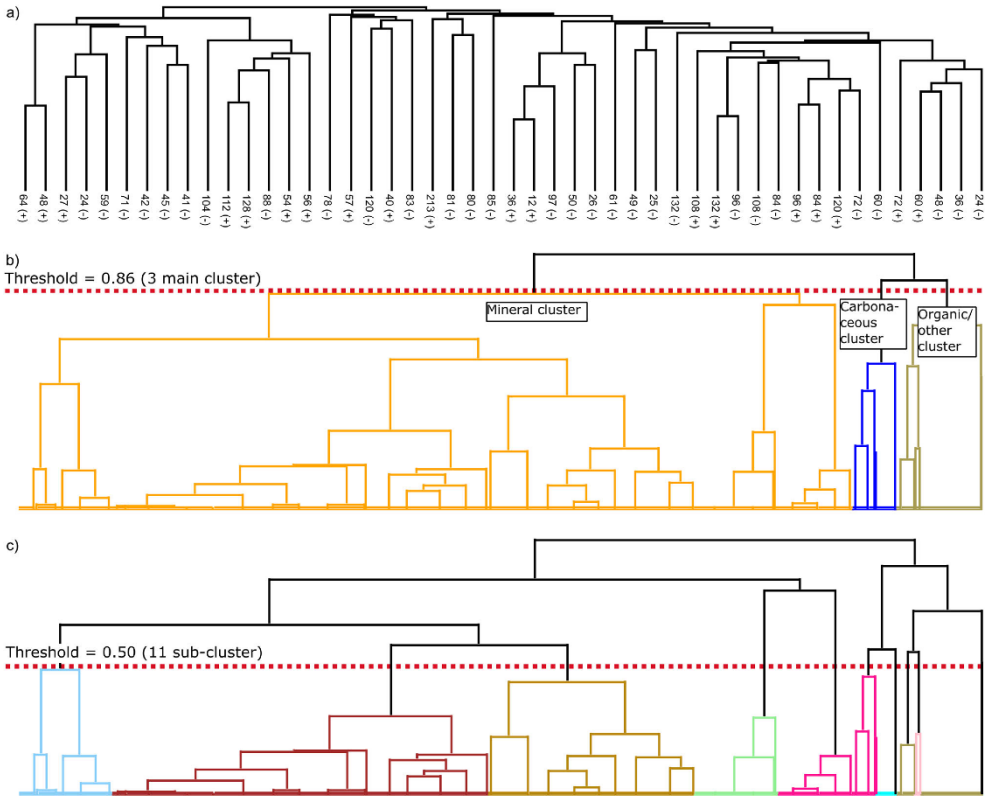

Figure 2. Dendrograms resulting from a HCA clustering method based on a Pearson correlation distance metric for the single particle spectra from Jungfraujoch atmospheric aerosols, ground and dispersed snow water residues and river sediment. (a) Column clustering for the descriptive signals from Table 2 and additional carbon cluster ions. (b) The three main cluster that can be further divided into 11 sub-clusters, and (c) after lowering the row tree threshold from 0.86 to 0.50.

particle spectra from the Jungfraujoch, 660 single-particle spectra from dispersed, ground river sediment, 265 single-particle spectra from dispersed, ground snow residue and the artificially aged as well as unaltered sum spectra of rock and sand populations.

The descriptive signals identified in Table 2 were used for clustering, together with additional carbon chain fragments from C_2^- to C_7^- and C_1^+ to C_{12}^+, which were included in the signal list to count for organic and carbonaceous particles in positive- and negative-ion spectra. The resulting dendrograms are shown in Figure 2. Dendrograms including heatmap visualization are shown in Figure S4. Column clustering of the chosen *m/z* values in Figure 2a shows groups of ions, with high correlations. For example, *m/z* (+) 56, 54, 112, 128, and *m/z* (-) 88, 104 were grouped together.

The respective ions arise from iron and iron oxides and are well separated from titanium and titanium oxide at *m/z* (+) 48 and 64. Correlations between different negative and positive ions, belonging to the same compound, enabled the separation of spectra with similar nominal-mass signal patterns, thus making the Pearson-based clustering well suited for classification of low-mass-resolution bipolar mass spectra.

For the generation of spectra patterns and to determine the quantitative composition of the Jungfraujoch single-particles, snow residues and sediments (Figure 3), a mean spectrum from all single-particle spectra contained within a chosen cluster (branch of the joining tree) was calculated. Changing the threshold in the joining tree of the dendrogram between 0.86 (Figure 2b), 0.50 (Figure 2c), and 0.17 (Figure S5) allowed to identify 3 main clusters, 11 sub-clusters

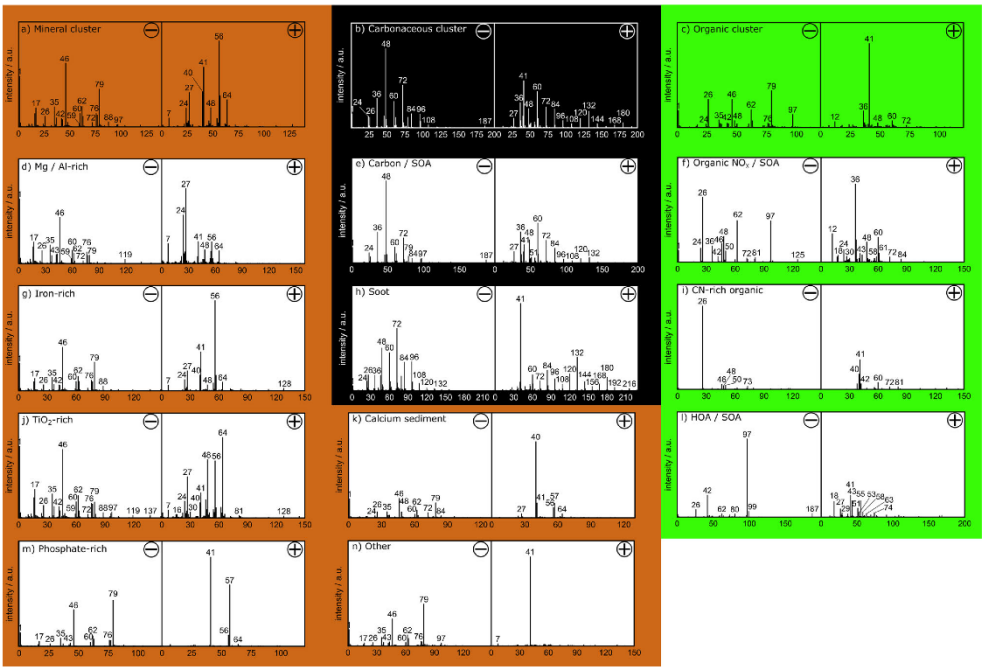

Figure 3. Spectra patterns derived from a HCA-clustering method based on a Pearson correlation distance metric for atmospheric single-particle spectra from Jungfraujoch, lab-measured snow water residues and river sediment. The patterns were assigned to different particle classes. The number of single particle spectra used to form the spectra patterns is given in brackets. Three main patterns were assigned to mineral particles (3177) (a), carbonaceous particles (160) (b), and organic particles (95) (c). Refining those main clusters allowed to identify 11 sub-spectra patterns (d) to (n). Sub spectra patterns for mineral particles were Mg/Al-rich (322) (d), iron-rich (1340) (g), TiO_2-rich (738) (j), phosphate-rich (293) (m), calcium sediment (267) (k), and other (215) (n). For the carbonaceous main cluster only one carbon/secondary organic aerosol (SOA) (92) (e) and one soot sub-cluster (68) (h) were found. Organic particles were separated in organic NO_x/SOA (70) (f), CN-rich organic (20) (i), and hydrocarbon like organic (HOA)/SOA (5) (l).

and 24 clusters (source apportionment), respectively. The artificially aged sum spectra were used as reference spectra in this classification to find online measured single-particle spectra that are most similar to aged sand and rock spectra.

A second clustering was carried out by using the unaltered instead of artificially aged rock and sand sum spectra. These were used here as a reference to identify "fresh" Jungfraujoch single-particle spectra that most closely resemble the rock and sand spectra patterns. To separate the very similar rock and sand sum spectra (see Figure S6), the distance threshold was lowered to 0.22, which resulted in 21 clusters. To pay more attention to aging-related features in this classification, the negatively charged ions with masses 46, 62, 63, and 79 (NO_2^-, NO_3^-, PO_2^-, and PO_3^-) were additionally used for HCA. It was observed that fresh mineral particles, besides their metal and metal oxide signals, were mainly characterized by their PO_3^- to NO_2^- signal intensity ratios. Higher values of PO_3^- indicate less-aged particles (Hinz et al. 2006). Some Jungfraujoch spectra appeared in the "fresh" as well as in the aged clusters, as these could not be clearly assigned due to slight aging characteristics. We decided to count these spectra as "fresh."

3.3.1. Particle clusters from JFJ, snow, and sediment samples

In a first step, a rough separation of particles, depending on the major characteristic ions was conducted. This resulted in a separation of three well defined main clusters (Figures 3a–c). These show carbonaceous, organic and mineral populations. The mineral particles make up 92.6% of the total particle population of all samples with a vacuum aerodynamic diameter between 400 and 5000 nm and an average of 1272 nm. Carbonaceous and organic particles are on average smaller with 1142 and 1136 nm, respectively.

From the three main clusters, a more refined classification into 11 sub-clusters was done. The sub-cluster patterns are shown in Figures 3d–n). Due to the removal of the sodium and potassium signals at *m/z* 23 and 39, the remaining potassium isotopic signal at *m/z* 41 is dominant in many spectra (see Figures 3c–n). The signal at *m/z* 41 was not removed because it can be an indicator for hydrocarbons ($C_3H_5^+$) as well. All clusters exhibited clearly distinguishable ion patterns which enabled a separate consideration of each individual cluster origin.

The carbonaceous cluster (Figure 3b) is divided into two sub-clusters, a soot cluster in Figure 3h, showing only carbon chain fragments from C_2^- to C_{11}^- and from C_5^+ to C_{18}^+ and a carbon/secondary organic aerosol (SOA) cluster in Figure 3e with shorter carbon-chain fragments and additional Al^+/$C_2H_3^+$, $C_4H_2^+$, $C_4H_3^+$ ions. Especially $C_4H_2^+$ and $C_4H_3^+$ are suitable diagnostic fragments for aromatic rings. The observed ions indicate the presence of polyaromatic hydrocarbons, which, due to their high fragmentation, mostly cannot be observed as complete molecular ions (Schmidt et al. 2017; Silva and Prather 2000). Schmidt et al. observed similar ions for a class of particles, which they assigned to cigarette smoke (Schmidt et al. 2017). In our case we found a higher degree of internal mixing for this particle cluster, including more and longer carbon-chain fragments. The negatively charged ion at *m/z* 187 ($C_8H_{11}O_5^-$) is referred to as a marker of α-pinene and indicates the absorption of SOA on soot or hydrocarbon particles followed by oxidation, resulting in the formation of 2-hydroxyterpenylic acid (Kahnt et al. 2014).

The smallest group of particles (Figure 3c), containing only 95 spectra, was assigned to organic material. The sub-cluster in Figure 3f represents oxidized organic material, mainly characterized by positively charged C^+, C_3^+, C_5^+/$C_3H_{10}N^+$, and $C_3H_8N^+$ (*m/z* 58) ions. The signal at *m/z* 43, referring to $C_2H_3O^+$, a marker of SOA single particle spectra, is elevated likewise (Dall'Osto and Harrison 2012; Qin et al. 2012; Schmidt et al. 2017). CN^-, NO_3^-, HSO_4^-, and C_3N^- (*m/z* 50) dominated the negatively charged ions besides less intense signals of carbon-chain fragments. Signals at *m/z* 125, 97, and 81 may be associated with the fragmentation of 2-hydroxyterpenylic acid. The fragment at *m/z* 125 is likely produced by loss of CO_2 and H_2O from *m/z* 187. The fragment at *m/z* 97 was caused by loss of CO from *m/z* 125 and *m/z* 81 by loss of CO_2 from *m/z* 125. The fragmentation patterns found are in very good agreement with results obtained by electrospray ionization tandem MS (ESI-MS^2) of extracted aerosol filter samples (Kahnt et al. 2014). The signal at *m/z* 97 can also arise from HSO_4^- as described before, while *m/z* 125 can also be assigned to $HN_2O_6^-$ (Silva and Prather 2000). The formation of 2-hydroxyterpenylic acid involves NO as reactant species and β-pinene is oxidized by NO_3, which explains the higher abundance of NO_2^-, NO_3^-, and NO^+ (at *m/z* 30) signals in this cluster (Kahnt et al. 2014; Zheng et al. 2005). C_3N^- and in particular $C_3H_8N^+$ and $C_3H_{10}N^+$ indicate a choline-like core structure, as for example in phosphatidylcholines. This could be an indication of a plant-based origin of the particle class. The latter two are known choline fragments in ESI-MS^2 (Chary et al. 2012). The CN-rich cluster in Figures 3i shows very high abundance of CN^-, which is generally associated with organic single particles (Bi et al. 2011). Besides that, there are hardly any characteristic signals in this class. SOA-like particles including hydrocarbon-like organic (HOA) species without any additional carbon chain fragments are summarized in Figure 3l. Major fragment ions in this sub-cluster were *m/z* 97 and 99, the latter due to a loss of two CO_2 groups from *m/z* 187. Positively charged ions in this cluster refer to hydrocarbon chain fragments at m/z 29, 43, 57… ($C_nH_{2n+1}^+$) and m/z 27, 41, 55, 69… ($C_nH_{2n-1}^+$) typically found for those particle type (Cross et al. 2009).

The numerically largest cluster with 3177 spectra in Figure 3a contains 6 different mineral sub-clusters shown in Figures 3d, g, j, k, m and n. These vary mainly in their metal and metal oxide intensities. Additionally, different degrees of atmospheric aging, represented by the negatively charged ions at *m/z* 35 (Cl^-), 46 (NO_2^-), and 62 (NO_3^-), are obvious. While the mineral sub-clusters (d), (g), and (j) show a moderate amount of calcium, cluster 3 (k) almost exclusively consists of calcium and shows, together with cluster 3 m), significantly enhanced intensities at *m/z* 57 within the positively charged ions. This signal is mainly caused by the presence of $CaOH^+$ rather than Fe^+ or $C_4H_9^+$. The phosphate-rich cluster in Figure 3m is an exception with respect to age-related signals. This sub-cluster is characterized by low nitrate and chloride intensities compared to phosphate. Particles in this cluster cannot be identified as fresh or aged, either because the phosphate was converted into easily soluble components which subsequently dissolved in snow, rain or river water, leaving undissolved phosphate in the mineral matrix, or because the particles were only slightly aged from the beginning (Tobo et al. 2010). As mentioned before, phosphate signals are boosted by matrix effects, so only small amounts

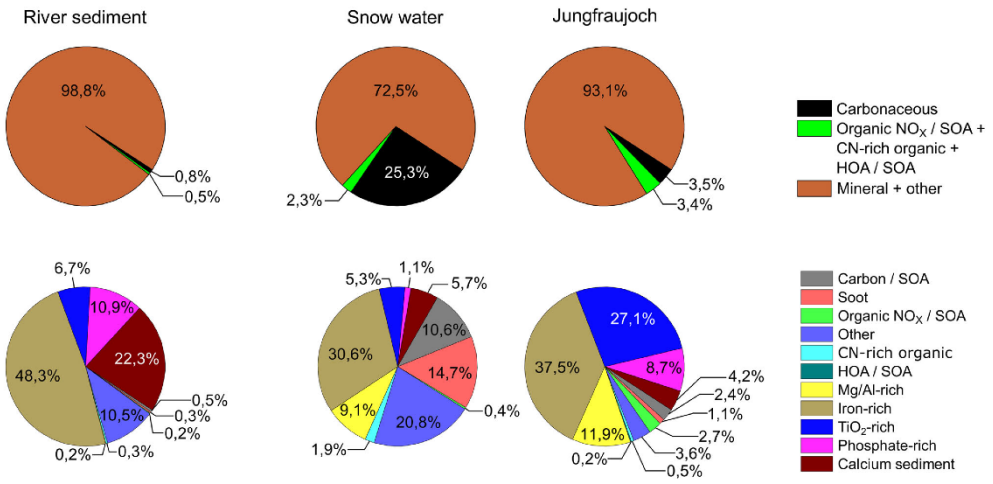

Figure 4. Distribution of particles over different clusters within the populations of dispersed, ground river sediment, dispersed, ground snow water residues and atmospheric aerosol particles online measured at Jungfraujoch. The categorization is based on the eleven clusters identified in Figure 3. The top row summarizes the three main groups but counting the "other" cluster to the mineral main cluster.

of phosphate are needed to produce sufficiently high signals once compounds that are easier to ionize are no longer present. As a result, these particles are mainly found in the river sediment population. Figure 3n summarizes particles which were difficult to assign to a distinct group. Due to the lack of characteristic signals in the spectra patterns, this cluster is labeled as "other." Particles assigned to this cluster typically show only very low intensities of ions in general, except for potassium, sodium, phosphate and silicon. However, these signals were mainly associated with mineral particles. Therefore, particles in this cluster were manually assigned to the group of mineral particles due to a higher consistency of the negatively charged ions with the mineral cluster patterns. Large proportions of particles from the snow water residues (20.8%) and river sediment (10.5%) were classified as "other" particles (see Figure 4).

The identified particle classes provide a good overview of the particle composition and internal mixing degree of the atmospheric particle population at the Jungfraujoch site. In this study, the different internally mixed particle types are clearly dominated by mineral particles with strong aging-related signals.

3.3.2. Composition of JFJ, snow, and river sediment samples

The composition of the Jungfraujoch, snow water and sediment populations can be illustrated by the proportion of spectra in the previously formed clusters. Figure 4 shows the distribution of particles based on the clusters identified in Figure 3. The first row of pie charts gives an overview of the distribution for the three main clusters within one population.

Comparison of the composition of snow water residues and Jungfraujoch aerosol particles is difficult. First, because snow water residues are an accumulation of particles over a longer period of time, whereas the Jungfraujoch data represent only a snapshot during the measurement campaign. On the other hand, the particles of the snow water residues were subsequently altered by dissolution, partitioning and agglomeration. The effect of accumulation is particularly evident in the high proportion of carbonaceous particles with a share of over 25% within the snow water spectra, especially in comparison to the atmospheric particle population on the Jungfraujoch. This proportion corresponds to the typical composition of the Jungfraujoch aerosol, which was measured, for example, during the CLACE-6 using a Single Particle Laser Ablation Time-of-Flight Mass Spectrometer (SPLAT), but is significantly lower than the proportion we see in our online measurements (Kamphus et al. 2010). One reason for this is the nozzle inlet system used in the LAMPAS 2, whose lower detection limit is around 500 nm and which can therefore detect the smaller carbon particles to a limited extent, compared to the aerodynamic lens used in the SPLAT

instrument. We assume that these small carbon particles will agglomerate in the snow water and thus enter the measurable size range of the LAMPAS device. On the other hand, the strong Sahara sandstorm activity during the measuring period is of course responsible for the low proportion of carbon particles measured online.

The iron-rich, Mg/Al-rich, calcium sediment and organic NO_x/SOA clusters exhibit very similar proportions within the Jungfraujoch and snow water populations. Greater differences exist for TiO_2-rich and phosphate-rich clusters. The dissolution of nitrate and other easily soluble compounds in the snow water and river sediment particles is expected to be the main cause for the high proportion of "other" particles in this populations. Due to the lack of further characteristic signals in this class, the original particle composition before dissolving in water is no longer accessible.

More than 70% of the river sediment particles were grouped within the iron-rich and calcium-sediment clusters. The high proportion of 22% calcium-sediment suggests that softer minerals like calcite accumulate within these particle populations due to their higher erosion. The iron-rich cluster in Figure 3g represents the largest group of particles within all three populations. The aged rock and sand particle sum spectra belong to this large cluster.

Deeper clustering into 24 clusters was able to separate these very similar particle types, whereas the most important distinguishing feature was the calcium content, as already confirmed by the ICP-MS measurements. These showed that the sand particles consist of 22% calcium, which corresponds to 45% $CaCO_3$, as long as $CaCO_3$ was the only source of calcium. So, this particle type consisted of roughly 50% igneous rock and 50% calcite, while the rock stone from the Jungfraujoch site was poor in calcium and resembled a more igneous-rock-like composition. The deeper clustering enables a more accurate identification of these types of mineral particles within the Jungfraujoch atmospheric aerosol population. As a result, 18% of the online-measured particles from the Jungfraujoch site were more igneous-rock-like while only 3% resembled the Morocco-sand-like signal pattern. The remaining 16% of the iron-rich particles in the Jungfraujoch population showed higher titanium ratios than the rock and sand particles. More than 23% of the river sediment particles belonged to the Morocco sand-like cluster.

3.3.3. Source apportionment analysis and atmospheric aging of particles

For the source apportionment of the different particle classes, we divided our complete single-particle measurement data from CLACE-1 into three episodes, from 17 March at 9 AM to 18 March at 10 PM, from 21 March at 11 PM to 23 March at midnight and from 24 March at 5 AM to 24 March at 7 PM. The temperature during the whole measurement campaign ranged from −24.3 to −7.7 °C. Figure 5a shows the total particle composition based on 8 selected particle classes in two-hour intervals. The number of particles was normalized to the respective interval. A total of 8 classes were selected. From the cluster analysis of the aged particles with 24 classes, 6 classes were used, which represent aged sand particles (calcium rich iron), aged rock particles (calcium poor iron), river sediment particles (calcium sediment), titanium oxide particles (TiO_2-rich), carbonaceous particles (Carbonaceous), and organic particles (organic NOx/SOA + CN-rich organic + HOA/SOA). From a classification with unaged sand and rock sum spectra, the less-aged sand (less-aged calcium rich) and rock particle (less-aged igneous rock) classes were included.

The presented results show only a small section of the particles actually present at the measurement location. Especially during some intervals, as for example on 21 March between 11 PM and 3 PM and on 24 March around noon, either the number of particles measured was too low for a statical evaluation or the LAMPAS 2 instrument was in a maintenance phase. The lower number of particles detected on these days could also be a result of the limited sampling efficiency of the LAMPAS 2 inlet system, which is in the range of 10^{-3} for particles with 800 nm diameter (Trimborn, Hinz, and Spengler 2000). The results for these periods should therefore be interpreted carefully. The statistical significance of the remaining measurement days is higher and more reliable, especially for the mineral particles examined here. The data points in Figure 5b show the mean particle sizes recorded by the LAMPAS 2 device for two-hour intervals of data recording. In addition, the sum of measured particles in one-hour intervals is shown as red columns. All findings are supported by either 180-h (Figure 5c) or 72-h back trajectories (Figures 5d–e).

In our measurement period, two Sahara sandstorm events were recorded, reaching from 16 March in the evening until 18 March and on 23 March and 24 March. In a previous study by Hinz et al., based on the same online data set, two episodes were observed during this period of time in which the number of super-micron particles (particle diameter >1 µm) measured by an optical particle counter (OPC) increased significantly (Hinz et al. 2005). Both events had an above-average influence on the particle

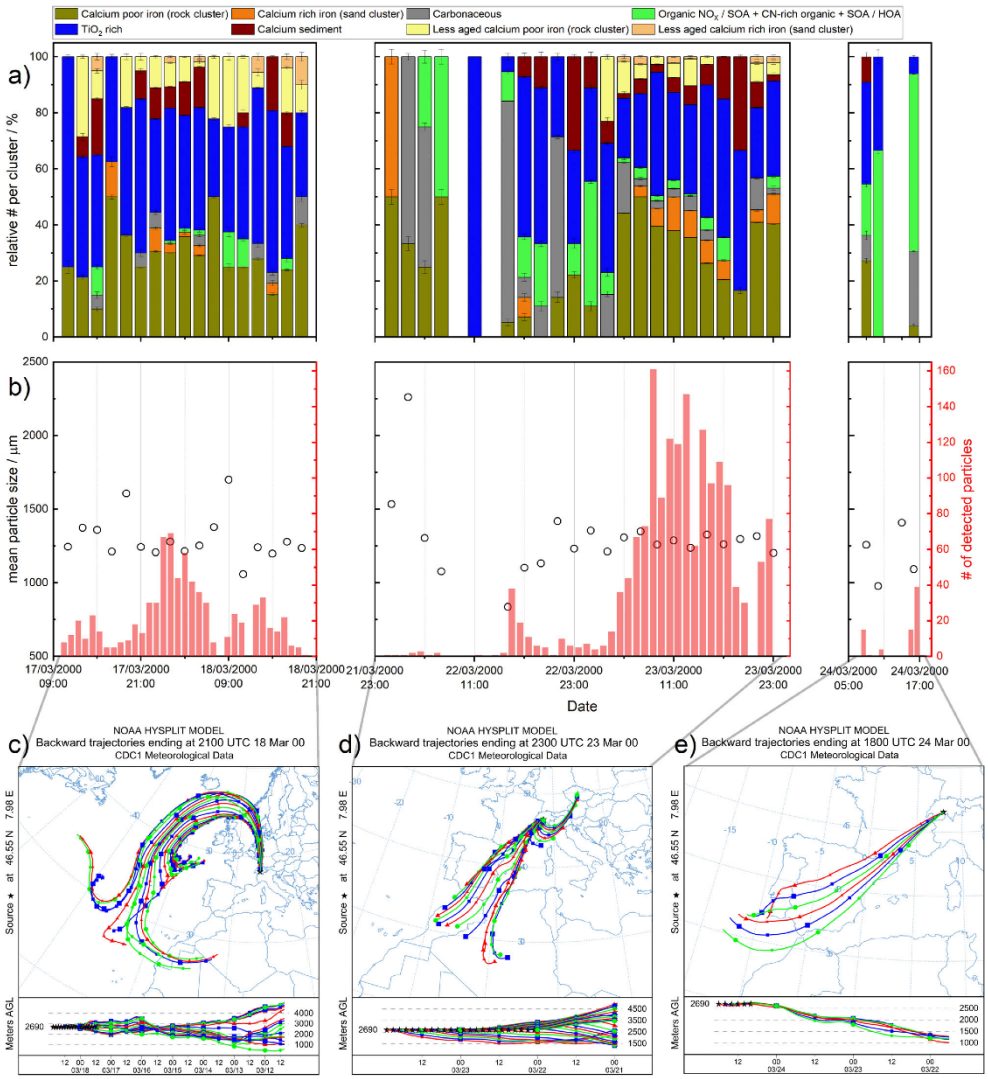

Figure 5. Relative number of particles per cluster in 2-h intervals (a), from 8 out of a 24/21 clusters. Particle groups were created based on two different classifications. First, the 24 clusters with artificially aged particles and second, a classification into 21 clusters with the unaltered sum spectra from rock and sand particles. The second classification was used for comparison to identify fresh mineral particles within the populations from Jungfraujoch and snow water. Particle sizes determined by LAMPAS 2 during the measurement period as mean of two hours of recording (black dots) and numbers of detected particles in one hour intervals shown as red bars (b). 180 h (c) and 72 h back trajectories (d, e), computed by HYSPLIT for the three measurement periods. The colors correspond to the trajectories simulated every two hours as shown in the time-altitude diagram below.

composition. Their effect on various particle classes is examined in more detail below.

At times with no or less desert-sand influence, TiO_2-rich, carbonaceous, organic, aged-rock, and calcium-sediment particles prevailed. The calcium-sediment-like and TiO_2-rich particles were found on all measurement days, except 22 March until 3 PM, where the total number of detected particles was the

lowest during the complete measurement period. On 22 and 24 March, the carbonaceous and organic particles contributed most to the total particle count, suggesting the influence of local traffic and industrial emissions (Hinz et al. 2005). Especially on 22 March, this was accompanied by a strong reduction in particle size over the course of the day, as can be seen in Figure 5b. The increase of the fraction of organic particles on 24 March is far above all other clusters and most probably originated from natural organic sources. On both days, the trajectories mainly showed the influence of continental particle sources, since the wind came from the east on 22 March, while on 23 March (Figure 5d) in the evening and 24 March (Figure 5e), mainly air masses from lower altitudes on the Spanish mainland reached the measuring station. Particularly within these periods, on 22 March around 11 PM and 23 March at 7 PM, the proportion of calcium-sediment particles was highest. Typically, the bottom rock in the alpine region consists of calcium-sediment mineral which is comparably soft, and erosion due to wind and weather is more likely than for other minerals. Such particles are found in atmospheric aerosols more frequently if their source is close to the measurement site. Those particles make up 4.1% of the total number of particles measured. On 23 March in the evening, the calcium sediment particles most likely originated from the Helvetic nappes, which surrounds the Aar Massif from the southwest to the north on the edges of the Alps, while on 22 March, air masses crossed the Dolomites. Both geological formations consist of calcareous sedimentary rocks and are located exactly in the directions of the air currents on the respective days. Due to the lower altitude, most of these regions are no longer snow-covered in spring, which makes it easy to blow up the eroded sediment. It can be assumed that the particle populations measured on 22 and 24 March reflect the typical composition of the aerosol at the Jungfraujoch site. This is supported by measurements of Cozic et al., showing a similar trend with organic matter as the main component in the fine mode for the measurement period in February, March, July and August 2005 at the Jungfraujoch (Cozic et al. 2008).

On all other measurement days, the effect of mineral dust transport from desert storm events prevailed. In total, higher ratios of sand and rock (aged and less aged), aged TiO_2 and calcium sediment particles were observed during 17/18 March (period 1) and 23 March (period 2) compared to 21/22 March and 24 March, suggesting the strong influence of desert sand for both periods. Especially the 4 sand and rock clusters were found to correlate reasonably well with the two Sahara desert storm events in the year 2000. Their share on the total population was about 25%. The main differences between the two events were the direction of the wind that transported the Sahara sand particles to the measuring station and their residence time in the atmosphere. When the first particles during these events arrived (March 17 at 1 PM and 7 PM, March 18 at 7 AM and March 23 at 3 AM), an elevated contribution of less-aged calcium-poor iron particles (rock) to the total population was observed, while the percentage of aged calcium-poor iron particles (rock) and less-aged calcium-rich iron particles (sand) increased with a two- to four-hour delay. Especially the less-aged particle types occurred exclusively on 17/18 March and 23 March and accounted for 4.2% of the total number of particles measured. This indicates that the fresh particles stemmed predominately from desert sand, transported to the measurement site without undergoing extensive alterations in the atmosphere. Another two to four hours later, the first aged sand particles (calcium rich iron) were detected (17 March at 5 PM and 11 PM and on 23 March at 7 AM), while the proportion of aged and less-aged rock particles slowly decreased (23 March between 1 and 9 PM).

For the first event, the back trajectories in Figure 5c show the influence of air, reaching the measurement site from northern directions. For those particles, an increase in size on 17 March at 7 PM and 18 March from 5 to 9 AM, due to coating effects, was observed (Figure 5b). This effect is most likely due to increased air pollution in urban areas north of the Alps and longer transportation times of up to 180 h, as no such increase in size was observed for the second Sahara dust event, where transportation times were in the range of 72 h (Figure 5d). Due to longer transportation times for the first event, a stronger removal of particles by sedimentation and scavenging was obtained, resulting in lower total particle numbers. This is especially true for the aged sand particles. Increased mixing of different particle sources, as some of the air masses came from high altitudes above the Atlantic, was also expected.

The development from fresh to aged particles becomes particularly clear during the second event on 23 March between 3 AM and 19 PM, which was almost exclusively influenced by Sahara sand, transported from southwest directions, as can be seen in Figure 5d. We saw a strong increase of TiO_2-rich and calcium sediment particle proportions when the source of the trajectories changed from Africa to the

European mainland during evening of 23 March. The TiO_2-rich particles were most likely exposed to a higher level of industrial or traffic pollution, which occurs mainly in lower altitude. They can be hardly addressed to a certain particle source but are typically transported in the atmosphere over a longer period of time, resulting in high nitrate and chloride fractions. This type of particles can be considered as strongly aged. The low amount of TiO_2 in most minerals (<1 *wt*%), together with its chemical stability and high UV absorption, promotes intense Ti^+ and TiO^+ signals in this particle class. Especially the TiO_2-rich and aged rock particles (calcium-poor iron) can also originate from local sources, where they were eroded and processed over a longer period of time and then transported to the measurement site by up winds. These particles, due to their strong aging features, can no longer be identified as coming from local sources.

A combination of different phenomena contributed to the observed effects of the successive mineral cluster appearance during both sandstorm events. The iron-rich particles of the resuspended Saharan sand consisted mainly of silicates and calcium carbonate. Especially the calcium cations react with the inorganic acids present in the atmosphere and thus significantly cause the aging of the particles. Model calculations show that due to the large number of emitted particles, a complete neutralization of the gaseous acids in the area of the dust outflow is probable (Abdelkader et al. 2017). Due to the hygroscopic properties of the salts formed, the aged particles were washed out of the atmosphere much more efficiently, while less-aged particles remained. Especially the silicate-rich particles are very stable, both chemically and physically, and were the first to arrive at the measuring station. Typically a few hours later during the sandstorm events, however, the proportion of aged sand and rock particles increased, compared to other particle classes. A similar effect was observed by Kandler et al. during single-particle measurements of sand storm events in the Moroccan desert (Kandler et al. 2009). The proportion of less-aged calcium-rich particles (sand cluster) was very low due to their fast conversion to aged particles, followed by scavenging during atmospheric transport.

In addition to the study by Hinz et al. in 2005, we were now able to correlate different stages of particle aging with particle sources and transport times. Anthropogenic influences were found predominately for particles transported in higher altitude over longer distances, as on 17 and 18 March, or for particles transported at lower altitudes, even if their transport is comparably fast. In the latter case it is very likely that a high amount of $CaCO_3$ in the original particles is responsible for the high proportion of age-related signals, even if they were only shortly exposed to anthropogenic influences (Henning et al. 2003).

4. Conclusion

With the LAMPAS 3 instrument, four different groups of mineral particles (rock, sand, sediment and snow water residues) were measured in the lab and compared to data from a measurement campaign at the Jungfraujoch in the Swiss Alps between 17 March, 2000 and 24 March, 2000. From the laboratory measurements, typical representative bipolar mineral particle spectra patterns were generated. Patterns from rock and sand particles provided information about fresh mineral particles, only slightly influenced by further anthropogenic or natural factors. The Rhine river sediment and snow water residue samples showed enhanced modifications and alterations due to mechanical erosion, mixing and solvation. The snow water residues were directly compared to the field-measured atmospherically aged particles from the Jungfraujoch. Source apportionment of mineral particles within the Jungfraujoch population was realized by using a HCA clustering approach with fresh as well as artificially aged sum spectra from sand and rock by only using a very limited number of descriptive ions, found for each population. A distinction into different particle classes as well as different stages of particle aging was possible. Due to the fast conversion of $CaCO_3$ to $Ca(NO_3)_2$ in the presence of HNO_3 in the atmosphere, particle spectra containing low nitrate signals at *m/z* 46 and 62 are expected to arise either from local sources or from remote locations only if they are chemically persistent or if their transport is fast. A determination of the percentage of particles arising from local and remote locations at different time points during the measurement period was achieved. It was found that the composition of the Jungfraujoch particles measured during the investigation period strongly diverged from the snow-water distribution due to temporal Sahara sandstorm events. At the beginning of these events, elevated fractions of fresh mineral particles were found that correlated nicely with the lab-measured Sahara-desert sand and rock particle populations. With increasing duration of the sandstorm events, a change from fresh to aged particles was observed, while during the periods between the sandstorm events only aged mineral and calcium sediment particles were found.

The fresh and lowly soluble mineral particles during the sandstorm events as well as the carbonaceous particles on the snow layer at the top regions of the Alps enhance the surface warming effect in this region. For the carbonaceous particles this is particularly important throughout the year, whereas the fresh particles only play a greater role at the beginning of the sandstorm events. Although the sandstorm events are very short, the mass concentrations of mineral dust are expected to be many times higher than the continuous sedimentation of BC particles over the year. Therefore, the reflectivity of snow, especially in the visible wavelength range, is much more influenced by mineral dust than by BC. Yasunari et al. could show a decrease in albedo of 20 to 40% by mineral dust versus 15 to 20% by BC (Yasunari et al. 2011). Especially in spring, where less fresh snowfall is expected, this results in faster snow melting. After sedimentation of the fresh particles, the increased amount of hygroscopic, aged particles in the air additionally supports light scattering and cloud formation. Titanium oxide and calcium sediment-like particles were observed during all measurement days in very similar ratios. While the first ones are thought to result from remote sources due to their high extent of atmospheric aging, the latter ones more likely stem from local sources, like the typical bottom rock of the Alpine region.

Funding

Financial support by the Deutsche Forschungsgemeinschaft (DFG), Germany, Grant No. HI 857/4-1, by the research program "Landes-Offensive zur Entwicklung Wissenschaftlich-oekonomischer Exzellenz – LOEWE," research focus "AmbiProbe," State of Hesse, Germany and by TransMIT GmbH, Giessen, Germany is gratefully acknowledged. We thank Rolf Alexander Düring and Elke Schneidenwind of the Institute of Soil Science and Soil Conservation, Justus Liebig University Giessen, for providing help in ICP-MS measurements.

References

Abdelkader, M., S. Metzger, B. Steil, K. Klingmüller, H. Tost, A. Pozzer, G. L. Stenchikov, L. Barrie, and J. Lelieveld. 2017. Sensitivity of transatlantic dust transport to chemical aging and related atmospheric processes. *Atmos. Chem. Phys.* 17 (6):3799–821. doi:10.5194/acp-17-3799-2017.

Abrecht, J., and U. Schaltegger. 1988. Aplitic intrusions in the central aar massif basement - geology, petrography and rb-sr data. *Eclogae Geol. Helv.* 81:227–39.

Albrecht, B. A. 1989. Aerosols, cloud microphysics, and fractional cloudiness. *Science* 245 (4923):1227–30. doi:10.1126/science.245.4923.1227.

Allen, R. J., W. Landuyt, and S. T. Rumbold. 2016. An increase in aerosol burden and radiative effects in a warmer world. *Nature Clim. Change* 6 (3):269–74. doi:10.1038/nclimate2827.

Andreae, M. O., and A. Gelencser. 2006. Black carbon or brown carbon? The nature of light-absorbing carbonaceous aerosols. *Atmos. Chem. Phys.* 6 (10):3131–48. doi:10.5194/acp-6-3131-2006.

Azar, A. T., S. A. El-Said, and A. E. Hassanien. 2013. Fuzzy and hard clustering analysis for thyroid disease. *Comput Methods Programs Biomed.* 111 (1):1–16. doi:10.1016/j.cmpb.2013.01.002.

Bi, X. H., G. H. Zhang, L. Li, X. M. Wang, M. Li, G. Y. Sheng, J. M. Fu, and Z. Zhou. 2011. Mixing state of biomass burning particles by single particle aerosol mass spectrometer in the urban area of prd, china. *Atmos. Environ.* 45 (20):3447–53. doi:10.1016/j.atmosenv.2011.03.034.

Brauer, M., P. Koutrakis, and J. D. Spengler. 1989. Personal exposures to acidic aerosols and gases. *Environ. Sci. Technol.* 23 (11):1408–12. doi:10.1021/es00069a013.

Cai, Y., A. Zelenyuk, and D. Imre. 2006. A high resolution study of the effect of morphology on the mass spectra of single psl particles with na-containing layers and nodules. *Aerosol Sci. Technol.* 40 (12):1111–22. doi:10.1080/02786820601001677.

Castro, A. L., P. J. A. Madeira, M. R. Nunes, F. M. Costa, and M. H. Florêncio. 2008. Titanium dioxide anatase as matrix for matrix-assisted laser desorption/ionization analysis of small molecules. *Rapid Commun Mass Spectrom* 22 (23):3761–6. doi:10.1002/rcm.3795.

Charlson, R. J., J. Langner, H. Rodhe, C. B. Leovy, and S. G. Warren. 1991. Perturbation of the northern-hemisphere radiative balance by backscattering from anthropogenic sulfate aerosols. *Tellus Series a-Dynamic Meteorology and Oceanography* 43 (4):152–63. doi:10.1034/j.1600-0870.1991.00013.x.

Chary, V. N., C. D. Kumar, M. Vairamani, and S. Prabhakar. 2012. Characterization of amino acid-derived betaines by electrospray ionization tandem mass spectrometry. *J Mass Spectrom.* 47 (1):79–88. doi:10.1002/jms.2029.

Cozic, J., B. Verheggen, E. Weingartner, J. Crosier, K. N. Bower, M. Flynn, H. Coe, S. Henning, M. Steinbacher, S. Henne, et al. 2008. Chemical composition of free tropospheric aerosol for pm1 and coarse mode at the high alpine site jungfraujoch. *Atmos. Chem. Phys.* 8 (2):407–23. doi:10.5194/acp-8-407-2008.

Cross, E. S., T. B. Onasch, M. Canagaratna, J. T. Jayne, J. Kimmel, X. Y. Yu, M. L. Alexander, D. R. Worsnop, and P. Davidovits. 2009. Single particle characterization using a light scattering module coupled to a time-of-flight aerosol mass spectrometer. *Atmos. Chem. Phys.* 9 (20):7769–93. doi:10.5194/acp-9-7769-2009.

Dall'Osto, M., and R. M. Harrison. 2012. Urban organic aerosols measured by single particle mass spectrometry in the megacity of london. *Atmos. Chem. Phys.* 12 (9):4127–42. doi:10.5194/acp-12-4127-2012.

El Asri, S., A. Laghzizil, A. Alaoui, A. Saoiabi, R. M'Hamdi, K. El Abbassi, and A. Hakam. 2009. Structure and thermal behaviors of moroccan phosphate rock (bengurir). *J. Therm. Anal. Calorim.* 95 (1):15–9. doi:10.1007/s10973-008-9114-z.

Gallavardin, S., U. Lohmann, and D. Cziczo. 2008. Analysis and differentiation of mineral dust by single particle laser mass spectrometry. *Int. J. Mass Spectrom.* 274 (1-3): 56–63. doi:10.1016/j.ijms.2008.04.031.

Gautam, R., N. C. Hsu, W. K. M. Lau, and T. J. Yasunari. 2013. Satellite observations of desert dust-induced himalayan snow darkening. *Geophys. Res. Lett.* 40 (5):988–93. doi:10.1002/grl.50226.

Hansen, J., and L. Nazarenko. 2004. Soot climate forcing via snow and ice albedos. *Proc Natl Acad Sci U S A ...* 101 (2):423–8. doi:10.1073/pnas.2237157100.

Haywood, J. M., and K. P. Shine. 1995. The effect of anthropogenic sulfate and soot aerosol on the clear-sky planetary radiation budget. *Geophys. Res. Lett.* 22 (5): 603–6. doi:10.1029/95GL00075.

Henning, S., E. Weingartner, M. Schwikowski, H. W. Gaggeler, R. Gehrig, K. P. Hinz, A. Trimborn, B. Spengler, and U. Baltensperger. 2003. Seasonal variation of water-soluble ions of the aerosol at the high-alpine site jungfraujoch (3580 m asl). *J. Geophys. Res* 108 (D1):10. doi:10.1029/2002JD002439.

Hinz, K. P., N. Erdmann, C. Gruning, and B. Spengler. 2006. Comparative parallel characterization of particle populations with two mass spectrometric systems lampas 2 and spass. *Int. J. Mass Spectrom.* 258 (1-3):151–66. doi: 10.1016/j.ijms.2006.09.008.

Hinz, K.-P., E. Gelhausen, K.-C. Schäfer, Z. Takats, and B. Spengler. 2011. Characterization of surgical aerosols by the compact single-particle mass spectrometer lampas 3. *Anal. Bioanal. Chem.* 401 (10):3165–72. doi:10.1007/s00216-011-5465-6.

Hinz, K. P., M. Greweling, F. Drews, and B. Spengler. 1999. Data processing in on-line laser mass spectrometry of inorganic, organic, or biological airborne particles. *J. Am. Soc. Mass Spectrom.* 10 (7):648–60. doi:10.1016/S1044-0305(99)00028-8.

Hinz, K. P., R. Kaufmann, and B. Spengler. 1996. Simultaneous detection of positive and negative ions from single airborne particles by real-time laser mass spectrometry. *Aerosol Sci. Technol.* 24 (4):233–42. doi:10.1080/02786829608965368.

Hinz, K. P., and B. Spengler. 2007. Instrumentation, data evaluation and quantification in on-line aerosol mass spectrometry. *J Mass Spectrom.* 42 (7):843–60. doi:10.1002/jms.1262.

Hinz, K. P., A. Trimborn, E. Weingartner, S. Henning, U. Baltensperger, and B. Spengler. 2005. Aerosol single particle composition at the jungfraujoch. *J. Aerosol Sci.* 36 (1):123–45. doi:10.1016/j.jaerosci.2004.08.001.

Isaksen, I. S. A., C. Granier, G. Myhre, T. K. Berntsen, S. B. Dalsoren, M. Gauss, Z. Klimont, R. Benestad, P. Bousquet, W. Collins, et al. 2009. Atmospheric composition change: Climate-chemistry interactions. *Atmos. Environ.* 43 (33):5138–92. doi:10.1016/j.atmosenv.2009.08.003.

Kahnt, A., Y. Iinuma, F. Blockhuys, A. Mutzel, R. Vermeylen, T. E. Kleindienst, M. Jaoui, J. H. Offenberg, M. Lewandowski, O. Boge, et al. 2014. 2-hydroxyterpenylic acid: An oxygenated marker compound for α-pinene secondary organic aerosol in ambient fine aerosol . *Environ. Sci. Technol.* 48 (9):4901–8. doi:10.1021/es500377d.

Kamphus, M., M. Ettner-Mahl, T. Klimach, F. Drewnick, L. Keller, D. J. Cziczo, S. Mertes, S. Borrmann, and J. Curtius. 2010. Chemical composition of ambient aerosol, ice residues and cloud droplet residues in mixed-phase clouds: Single particle analysis during the cloud and aerosol characterization experiment (clace 6). *Atmos. Chem. Phys.* 10 (16):8077–95. doi:10.5194/acp-10-8077-2010.

Kandler, K.,. L. Schutz, C. Deutscher, M. Ebert, H. Hofmann, S. Jackel, R. Jaenicke, P. Knippertz, K. Lieke, A. Massling, et al. 2009. Size distribution, mass concentration, chemical and mineralogical composition and derived optical parameters of the boundary layer aerosol at tinfou, morocco, during samum 2006. *Tellus Series B-Chemical and Physical Meteorology* 61 (1):32–50. doi:10.1111/j.1600-0889.2008.00385.x.

Koch, D., S. Menon, A. Del Genio, R. Ruedy, I. Alienov, and G. A. Schmidt. 2009. Distinguishing aerosol impacts on climate over the past century. *Journal of Climate* 22 (10):2659–77. doi:10.1175/2008JCLI2573.1.

Laskin, A., M. J. Iedema, A. Ichkovich, E. R. Graber, I. Taraniuk, and Y. Rudich. 2005. Direct observation of completely processed calcium carbonate dust particles. *Faraday Discuss.* 130:453–68. doi:10.1039/b417366j.

Liou, K. N., Y. Takano, C. He, P. Yang, L. R. Leung, Y. Gu, and W. L. Lee. 2014. Stochastic parameterization for light absorption by internally mixed bc/dust in snow grains for application to climate models. *J. Geophys. Res. Atmos.* 119 (12):7616–32. doi:10.1002/2014JD021665.

Matschullat, J., W. Maenhaut, F. Zimmermann, and J. Fiebig. 2000. Aerosol and bulk deposition trends in the 1990's, eastern erzgebirge, central europe. *Atmospheric Environment* 34:3213–21. doi:10.1016/S1352-2310(99)00516-6.

Ming, J., H. Cachier, C. Xiao, D. Qin, S. Kang, S. Hou, and J. Xu. 2008. Black carbon record based on a shallow himalayan ice core and its climatic implications. *Atmos. Chem. Phys.* 8 (5):1343–52. doi:10.5194/acp-8-1343-2008.

Murphy, D. M., D. J. Cziczo, K. D. Froyd, P. K. Hudson, B. M. Matthew, A. M. Middlebrook, R. E. Peltier, A. Sullivan, D. S. Thomson, and R. J. Weber. 2006. Single-particle mass spectrometry of tropospheric aerosol particles. *Journal of Geophysical Research-Atmospheres* 111 (D23):1–15. doi:10.1029/2006jd007340.

Nabat, P., S. Somot, M. Mallet, F. Sevault, M. Chiacchio, and M. Wild. 2015. Direct and semi-direct aerosol radiative effect on the mediterranean climate variability using a coupled regional climate system model. *Clim. Dyn.* 44 (3–4):1127–55. doi:10.1007/s00382-014-2205-6.

Qin, X. Y., K. A. Pratt, L. G. Shields, S. M. Toner, and K. A. Prather. 2012. Seasonal comparisons of single-particle chemical mixing state in riverside, ca. *Atmos. Environ.* 59:587–96. doi:10.1016/j.atmosenv.2012.05.032.

Ramanathan, V., and G. Carmichael. 2008. Global and regional climate changes due to black carbon. *Nature Geosci.* 1 (4):221–7. doi:10.1038/ngeo156.

Reilly, P. T. A., A. C. Lazar, R. A. Gieray, W. B. Whitten, and J. M. Ramsey. 2000. The elucidation of charge-

transfer-induced matrix effects in environmental aerosols via real-time aerosol mass spectral analysis of individual airborne particles. *Aerosol Sci. Technol.* 33 (1–2):135–52. doi:10.1080/027868200410895.

Rolph, G., A. Stein, and B. Stunder. 2017. Real-time environmental applications and display system: Ready. *Environmental Modelling & Software* 95:210–28. doi:10.1016/j.envsoft.2017.06.025.

Russell, A. G., G. R. Cass, and J. H. Seinfeld. 1986. On some aspects of nighttime atmospheric chemistry. *Environ. Sci. Technol.* 20 (11):1167–72. doi:10.1021/es00153a013.

Schmidt, S.,. J. Schneider, T. Klimach, S. Mertes, L. P. Schenk, P. Kupiszewski, J. Curtius, and S. Borrmann. 2017. Online single particle analysis of ice particle residuals from mountain-top mixed-phase clouds using laboratory derived particle type assignment. *Atmos. Chem. Phys.* 17 (1):575–94. doi:10.5194/acp-17-575-2017.

Shen, X., H. Saathoff, W. Huang, C. Mohr, R. Ramisetty, and T. Leisner. 2019. Understanding atmospheric aerosol particles with improved particle identification and quantification by single-particle mass spectrometry. *Atmos. Meas. Tech.* 12 (4):2219–40. doi:10.5194/amt-12-2219-2019.

Shindell, D. T., G. Faluvegi, D. M. Koch, G. A. Schmidt, N. Unger, and S. E. Bauer. 2009. Improved attribution of climate forcing to emissions. *Science* 326 (5953):716–8. doi:10.1126/science.1174760.

Sierau, B., R. Y. W. Chang, C. Leck, J. Paatero, and U. Lohmann. 2014. Single-particle characterization of the high-arctic summertime aerosol. *Atmos. Chem. Phys.* 14 (14):7409–30. doi:10.5194/acp-14-7409-2014.

Silva, P. J., and K. A. Prather. 2000. Interpretation of mass spectra from organic compounds in aerosol time-of-flight mass spectrometry. *Anal. Chem.* 72 (15):3553–62. doi:10.1021/ac9910132.

Sokolik, I. N., and O. B. Toon. 1999. Incorporation of mineralogical composition into models of the radiative properties of mineral aerosol from uv to ir wavelengths. *J. Geophys. Res.* 104 (D8):9423–44. doi:10.1029/1998JD200048.

Song, C. H., and G. R. Carmichael. 1999. The aging process of naturally emitted aerosol (sea-salt and mineral aerosol) during long range transport. *Atmos. Environ.* 33 (14):2203–18. doi:10.1016/S1352-2310(98)00301-X.

Stein, A. F., R. R. Draxler, G. D. Rolph, B. J. B. Stunder, M. D. Cohen, and F. Ngan. 2015. Noaa's hysplit atmospheric transport and dispersion modeling system. *Bulletin of the American Meteorological Society* 96 (12):2059–77. doi:10.1175/BAMS-D-14-00110.1.

Tegen, I., A. A. Lacis, and I. Fung. 1996. The influence on climate forcing of mineral aerosols from disturbed soils. *Nature* 380 (6573):419–22. doi:10.1038/380419a0.

Tobo, Y., D. Z. Zhang, A. Matsuki, and Y. Iwasaka. 2010. Asian dust particles converted into aqueous droplets under remote marine atmospheric conditions. *Pnas.* 107 (42):17905–10. doi:10.1073/pnas.1008235107.

Trimborn, A., K. P. Hinz, and B. Spengler. 2000. Online analysis of atmospheric particles with a transportable laser mass spectrometer. *Aerosol Sci. Technol.* 33 (1–2):191–201. doi:10.1080/027868200410921.

Twomey, S. 1977. The influence of pollution on the shortwave albedo of clouds. *J. Atmos. Sci.* 34 (7):1149–52. doi:10.1175/1520-0469(1977)034<1149:TIOPOT.

Tyanova, S., T. Temu, P. Sinitcyn, A. Carlson, M. Y. Hein, T. Geiger, M. Mann, and J. Cox. 2016. The perseus computational platform for comprehensive analysis of (prote)omics data. *Nat. Methods.* 13 (9):731–40. doi:10.1038/nmeth.3901.

Ulbrich, I. M., M. R. Canagaratna, Q. Zhang, D. R. Worsnop, and J. L. Jimenez. 2009. Interpretation of organic components from positive matrix factorization of aerosol mass spectrometric data. *Atmos. Chem. Phys.* 9 (9):2891–918. doi:10.5194/acp-9-2891-2009.

Ward, J. H. 1963. Hierarchical grouping to optimize an objective function. *J. Am. Stat. Assoc.* 58 (301):236–44. doi:10.2307/2282967.

Yasunari, T. J., R. D. Koster, K.-M. Lau, T. Aoki, Y. C. Sud, T. Yamazaki, H. Motoyoshi, and Y. Kodama. 2011. Influence of dust and black carbon on the snow albedo in the nasa goddard earth observing system version 5 land surface model. *J. Geophys. Res* 116 (D2):1–15. doi:10.1029/2010JD014861.

Zauscher, M. D., Y. Wang, M. J. K. Moore, C. J. Gaston, and K. A. Prather. 2013. Air quality impact and physicochemical aging of biomass burning aerosols during the 2007 san diego wildfires. *Environ. Sci. Technol.* 47 (14):7633–43. doi:10.1021/es4004137.

Zheng, M., L. G. Salmon, J. J. Schauer, L. M. Zeng, C. S. Kiang, Y. H. Zhang, and G. R. Cass. 2005. Seasonal trends in pm2.5 source contributions in beijing, china. *Atmos. Environ.* 39 (22):3967–76. doi:10.1016/j.atmosenv.2005.03.036.

4 Publication 2

Particle characterization and quantification of organic and inorganic compounds from Chinese and Iranian aerosol filter samples using scanning laser desorption/ionization mass spectrometry

Christof Barth, Klaus-Peter Hinz, and Bernhard Spengler

Institute of Inorganic and Analytical Chemistry, Justus Liebig University Giessen, Giessen, Germany

Analytical and Bioanalytical Chemistry **2022**, 414, pp 7223-7241

DOI: https://doi.org/10.1007/s00216-022-04275-1

Analytical and Bioanalytical Chemistry (2022) 414:7223–7241
https://doi.org/10.1007/s00216-022-04275-1

RESEARCH PAPER

Particle characterization and quantification of organic and inorganic compounds from Chinese and Iranian aerosol filter samples using scanning laser desorption/ionization mass spectrometry

Christof Barth[1] · Klaus-Peter Hinz[1] · Bernhard Spengler[1]

Received: 17 May 2022 / Revised: 4 August 2022 / Accepted: 9 August 2022 / Published online: 1 September 2022

Abstract
Besides their influence on climate and cloud formation, many organic and inorganic substances in aerosol particles pose a risk to human health. Namely, polycyclic aromatic hydrocarbons (PAH) and heavy metals are suspected to be carcinogenic or acutely toxic. The detection and quantification of such compounds is difficult if only small amounts of particulate matter (PM) are available. In addition, filter samples are often complex and time-consuming to prepare for chromatographic measurements and elemental analysis. Here, we present a method based on high-resolution atmospheric pressure laser desorption ionization mass spectrometry imaging (AP-LDI-MSI) and statistical analysis which allows the analysis and characterization of very small sample quantities (< 30 µg) without any sample preparation. The power and simplicity of the method is demonstrated by two filter samples from heavily polluted mega cities. The samples were collected in Tehran (Iran) and Hangzhou (China) in February 2018. In the course of the measurement, more than 3200 sum formulae were assigned, which allowed a statistical evaluation of colocalized substances within the particles on the filter samples. This resulted in a classification of the different particle types on the filters. Finally, both megacities could be distinguished based on characteristic compounds. In the samples from Tehran, the number of sulphur-containing organic compounds was up to 6 times as high as the samples from Hangzhou, possibly due to the increasing efforts of the Chinese government to reduce sulphur emissions in recent years. Additionally, quantification of 13 PAH species was carried out via standard addition. Especially, the samples from Tehran showed elevated concentrations of PAHs, which in the case of higher-molecular-weight species ($> m/z$ 228) were mostly more than twice as high as in Hangzhou. Both cities showed high levels of heavy metals and potentially harmful organic compounds, although their share of total particulate matter was significantly higher in the samples from Tehran. The pretreatment of the samples was reduced to a minimum with this method, and only small amounts of particles were required to obtain a comprehensive picture for a specific filter sample. The described method provides faster and better control of air pollution in heavily polluted megacities.

Keywords Aerosol composition · Laser desorption ionization mass spectrometry · Pollution · Inorganic particles · Organic particles · Megacities

Introduction

Increasing air pollution through the emission of gases and particles is becoming a major problem in many heavily populated regions of the world [1]. Urban aerosols, especially in heavily polluted megacities, are complex mixtures of organic and inorganic substances which, in addition to their effect on the climate, are of particular relevance because of their harmful effects on human health. Their emission leads to an increase in mortality among the population of many megacities around the world through lung cancer, chronic obstructive pulmonary diseases, ischemic heart disease, stroke and respiratory tract infections [2–4]. Calculations show that about 3.3 million premature deaths worldwide can be attributed to outdoor air pollution [5]. Emissions from industry, traffic and private households dominate the air pollution in larger cities [6]. Some megacities, for example on the Arabian Peninsula or in China, are an exception, as the

✉ Bernhard Spengler
Bernhard.spengler@anorg.chemie.uni-giessen.de

[1] Institute of Inorganic and Analytical Chemistry, Justus Liebig University Giessen, 35392 Giessen, Hessen, Germany

strong seasonal influence of desert sand transport, and thus the proportion of mineral dust, can become dominant here. At times, the proportion of mineral dust can exceed 40% of the total particle mass with industrial pollutants adding to mineral components [7, 8].

Globally, about 82% of the population is exposed to annual mean levels of $PM_{2.5}$ or PM_{10} that exceed World Health Organization (WHO) guidelines [5, 9]. The most polluted cities worldwide, like for example Varanasi (India), Shijiazhuang (China) and Peshawar (Pakistan), are located in East Asia and on the Arabian Peninsula [9]. In many countries such as China, India, Pakistan and some Arab countries, the focus is on increasing productivity at low cost rather than on air pollution control through expensive and complex filter technologies and low-emission processes [10–12]. The most important factors affecting an increase in air pollution and the emission of climate-damaging gases are the coal-dominated energy sector and traffic emissions [13]. Both are a direct consequence of population increase, rising urbanisation and the desire for more technology and prosperity [14]. However, while China and India are trying to reduce emissions of industrial waste, heavy metals in exhaust gases or sulphates in the flue gas of power plants through emission control measures, there is a lack of such regulations in Iran [11].

Commonly used methods for characterizing air quality are based on measuring particle number concentrations with condensation nucleus counters (CNC), optical particle counters (OPC), total particulate mass concentrations by using particle filter samples or impactors or measurements of black carbon concentrations by an aethalometer [15–19]. However, these methods only provide information on how many particles of a certain type or a certain size are present in the air and whether they can penetrate deep into the lungs to cause damage. It is not possible to make statements about the toxicity of the particles with these methods. For more detailed statements on air quality, it is therefore essential to know the chemical composition of atmospheric particles [20]. This allows for a better understanding of the danger of the particles, their origin and possible chemical changes caused by reactions in the atmosphere. Nowadays, the detection and identification of various inorganic and organic compounds is usually carried out using mass spectrometric techniques. Numerous methods based on mass spectrometry (MS), typically coupled with chromatographic separation techniques, are available. These allow a comprehensive chemical characterization of particle samples. Among others, high-performance liquid chromatography–mass spectrometry (HPLC–MS), gas chromatography–mass spectrometry (GC–MS), inductively coupled plasma–mass spectrometry (ICP-MS) and ion chromatography–mass spectrometry (IC-MS) offer the possibility to analyze aerosol compounds with high quantitative accuracy [21–24]. However, these methods go along with comprehensive and time-consuming filter preparation steps and pre-separation of the substances or substance classes prior to mass analysis [25, 26]. On the other hand, it is not possible to attribute the measured chemical properties to individual particles with these methods. Furthermore, it is possible that the particles on the filter surface are modified during sampling, transport, storage and processing of the sample, effects known as sampling artifacts [27]. Extraction and digestion of the filter samples typically takes hours and is associated with a high consumption of chemicals and often low recovery rates, about 20% for resolvable organic compounds [28].

More meaningful is the measurement of the particle composition in its natural environment, preferably at the single-particle level [29–31]. These real-time measurements allow particle-based characterization without any particle modification, but are typically not quantitative and suffer from poor mass resolution and mass accuracy in the case of mass spectrometry [32]. Both factors make the exact identification of the detected substances difficult and do not allow a detailed statement about the original amount of the often highly fragmented compounds.

The aim of this study was to combine the advantages of both methods, high-resolution atmospheric pressure laser desorption/ionization mass spectrometry and single-particle measurement, in order to identify as many substances as possible in the sample and to correctly assign them nearly on the level of individual particles. Another aspect was to reduce sample preparation compared to common analytical methods or to avoid it completely if possible. This was made possible by using a high-resolution mass spectrometer with an autofocusing imaging laser ablation source combined with a statistical evaluation of the image data. An approach for quantification of polycyclic aromatic hydrocarbons (PAH) with very low sample preparation via standard addition calibration is also shown. The samples were taken during winter at two heavily polluted megacities, Tehran and Hangzhou in Iran and China. Both cities are among the 500 most polluted cities in the world in 2018 according to the WHO [9].

Materials and methods

Particle sampling

Particles were sampled in Tehran (Iran) and in Hangzhou (China) on quartz filters in February 2018 for 2 days. The four samples were named as follows, FPI17B0807 and FPI17B0811 for Hangzhou on days 1 and 2, and 287 and 289 for Tehran on days 1 and 2. Sampling in Tehran took place at the Sharif University which is 500 m away from Sheikh Fazl-allah Nouri Expressway and 300 m from Yadegar-e-Emam Expressway, both heavily trafficked main roads in

downtown. Sampling was done with a low-volume sampling device at 20 L/min for 24 h each. In Hangzhou, the filters were also sampled on consecutive days for 23 h at 16.67 L/min. The location of the sampling was on the rooftop of a company headquarters in a business park, a few kilometres south of Hangzhou downtown. The filters were weighed until a constant mass was obtained (< 0.04 mg). Filters were stored in a fridge at 5 °C and protected from light until the measurements took place (January 2019–July 2019).

Filter measurements

Filters were cut into pieces, and particulate matter on the filters was directly measured with an AP-SMALDI5 AF imaging ion source (TransMIT GmbH, Giessen, Germany) on a Q Exactive HF mass spectrometer (Thermo Fisher Scientific GmbH, Bremen, Germany) at 50 µm pixel resolution in a mass range of *m/z* 50–750. For laser desorption and ionization, a diode-pumped solid-state laser at a wavelength of 343 nm with 50 pulses per pixel at 100 Hz was used. High-resolution MS imaging data of the filter surfaces at a mass resolution (R) of 240,000 in positive- and negative-ion mode were employed by using the autofocusing function of the ion source. The measured sample area for each filter was 37.5 mm^2 for each polarity, corresponding to 150 × 100 pixels. Microscopic images of the measured versus unmeasured filter area and height information of the filter surface are shown in SI Fig. 1. For the quantification of PAHs, a dilution series of EPA 525 PAH mix A from Sigma-Aldrich (St. Louis, MO, USA), containing acenaphthylene (AcPy) at *m/z* 152.062; fluorene (Flu) at *m/z* 166.078; phenanthrene (PA), anthracene (Ant) at *m/z* 178.078; pyrene (Pyr) at m/z 202.078; benz[a]anthracene (BaA), chrysene (Chr) at m/z 228.094; benzo(b)fluoranthene (BbF), benzo[k]fluoranthene (BkF), benzo(a)pyrene (BaP) at *m/z* 252.094; benzo(g,h,i) perylene (BghiP), indeno(1,2,3-cd)pyrene (IND) at *m/z* 276.094 and dibenz(a,h)anthracene (DBA) at *m/z* 278.109 in dichloromethane, was prepared with concentrations of 43.03, 19.60, 3.90 and 0.37 µg/mL. Dried droplet application of 1 µL of each dilution, followed by drying for 1 h and consecutive mass measurement with the same ion source in a mass window of *m/z* 150–500 was carried out for the complete spotted area and additional area without a spotted standard for blank measurement.

Data evaluation

For characterization of the filter samples, selection of *m/z* signals from the imaging raw data was conducted by our in-house developed software package MIRION at a bin size of 0.003 Da with a minimum image coverage of 0.05% [33]. A list of mass spectrometric features with maximum intensities for each *m/z* bin in each sample and for both polarities was extracted and filtered for signals above a relative threshold of 0.1% for negative ions and 0.4% for positive ions. Not all signals detected using the threshold criteria could be assigned to sum formulae based on mass deviation, Kendrick mass defect and isotope patterns. The signals that could not be assigned, mostly had intensities that were too low to detect corresponding isotope patterns and thus to use mass defects as criteria for assignment. Furthermore, the signals with very low intensities often showed strong variances in their mass deviation. The proportion of unassignable signals ranged from 1.4% for positively charged ions in Hangzhou to 6.6% for negatively charged ions in Tehran. Extraction of pixelwise intensities for the selected *m/z* signals was carried out by MSiReader at a mass window of ± 2.5 ppm [34]. Sum formula assignments for each signal were done manually via the XCalibur software (Thermo Fisher Scientific, San Jose, CA) based on measured mass, mass error and isotopic patterns (if available). For validation of mass assignments, additional criteria were used, such as Kendrick mass defect of CH_2 and colocalization of sum formulas. A statistical approach was used to find colocalized signals that help to identify particles within the ablation area by correlating *m/z* signals. A hierarchical clustering (HCA) algorithm with *k*-means preprocessing within the Perseus software package (Version 1.6.14.0) allowed us to group signals that are found at the same positions on the filter surface [35]. Intensities were *z*-normalized for each assigned sum formula. The HCA was run 5 times to give a maximum of 50 data clusters for each filter and for positive- and negative-ion modes using complete linkage between the original data clusters. HCA was also used to find compounds that were statistically significant for each measurement location and independent of the sampling date. Therefore, a two-sample test was applied in positive- and negative-ion mode and the resulting compounds with ρ-values (probability that the means of two sample sets are significantly different) below 0.05 were used for clustering. Normalized mean intensities were used in this approach for each signal. To better illustrate the differences between cities, *Z*-score values were plotted based on the median for each significant *m/z* signal.

For quantification of the PAHs, the raw data was converted into imzml files and a region of interest (ROI) was selected manually for each deposited PAH concentration and one additional area was selected to determine the zero value and identify chemical noise signals. Total ion count (TIC) normalized intensities were extracted and calibration curves were calculated and evaluated using the standard addition technique. Results for each PAH signal were obtained by using the total particle mass and occupied area per filter relative to the ROI area. The ROI corresponded to only fractions of the total particle mass per filter, allowing quantification with less than 30 µg particle mass.

Results

Number and composition of compounds

A total of 3258 m/*z* signals, excluding isotopic features of assigned signals, were assigned to all four filter samples collected on 2 days each in Hangzhou (China) and Tehran (Iran), 1981 in positive- and 1277 in negative-ion mode. Results are represented by Venn diagrams in Fig. 1. The particle mass concentrations were 43.1 µg/m^3 and 37.5 µg/m^3 for Tehran on days 1 (287) and 2 (289), respectively. Significantly higher concentrations were found in the Chinese samples with 174.7 µg/m^3 and 106.5 µg/m^3 on days 1 (FPI17B0807) and 2 (FPI17B0811). The annual mean value in Iran has been decreasing since 2012 and was 72 µg/m^3 per year according to the WHO database [9]. Thus, the mass concentrations on our sampling days were significantly below the average. There are several possibilities why these concentrations might have been lower than the actual concentrations during sampling in Tehran. One possible reason is the time lag of several weeks between sampling and the final weighing in Germany. Another possible reason is the lower relative humidity in February in Tehran (57%) compared to Hangzhou (66%), which most probably led to a strong loss of volatile ammonium nitrate during the initial sampling [36, 37]. The significantly higher average humidity in Hangzhou combined with the direct weighing of the filters after sampling indicate that the measured concentrations were not subject to major changes during and after sampling and were thus close to the actual particle concentrations in the air. Studies show that the highest losses of ammonium nitrate occur below 60% relative humidity, while no loss is expected close to 100% [38]. Furthermore, a significant reduction of NO_3^- ions from particulate nitrate in the presence of acid sulphates and ammonia in the collected particles can be expected, since the formed nitrate compounds are volatile. In the later course of this study, it becomes clear that due to strongly increased sulphate contents in the Tehran samples, this can lead to significant differences in nitrate content between the Chinese and Iranian samples. The annual mean concentration in Hangzhou fluctuated between 85 and 150 µg/m^3 between 2013 and 2016, which is in the range of the concentrations measured in this study [9]. These particle mass concentrations indicate that particle pollution was higher in Hangzhou than in Tehran during the sampling period. This is also in line with the 27% higher number of detected signals and assigned sum formulas in the Chinese samples. In particular, 2522 sum formulas were assigned for both Chinese filters and 1987 for both Iranian filters. The Chinese samples showed a higher number of signals in the positive-ion mode (918, 1176) than in the negative-ion mode (690, 600), whereas for both Iranian samples the number of assigned sum formulae in the positive-ion mode (826, 568) was lower than in the negative-ion mode (892, 778). This was somewhat surprising, because LDI MS typically results in higher yields of positively charged than negatively charged ions, depending on the particle composition [39, 40]. The higher number of negatively charged ions in Tehran may have two reasons, most likely related to acidity and availability of anions. Negative charges arise mainly from capturing free electrons of photoionized analyte molecules in the plume or by the presence of substances with a high gas-phase basicity acting as a matrix that deprotonates inorganic and organic acids [41]. The second case is more likely and indicates that the samples from Tehran contain a higher amount of acidic compounds which can be easily deprotonated. The presence of these compounds is expected due to reactions

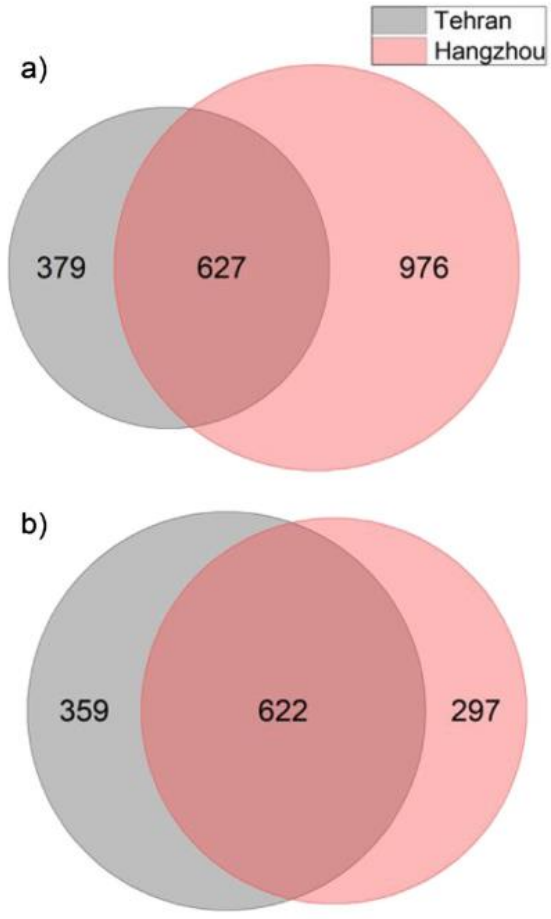

Fig. 1 Total number of assigned sum formulae features represented in Venn diagrams for positive (**a**) and negative (**b**) ion mode

of primary aerosols with sulphur dioxide and dimethyl sulphide, resulting in sulphuric acid–containing particles.

Figure 2 provides an overview of all assigned sum formulae in positive- and negative-ion mode, divided into 11 categories, for both cities on the two sampling days. Here, we used the number of assigned signals instead of using intensity or peak abundance due to high uncertainties in ionization yield and behaviour of the different ions and classes of ions. The categories can be roughly separated into organic (CHO, CHON, CH, CHN, CHOS, PAH, CHNS, CHS, CHONS) and inorganic compounds (carbon, inorganic). Sum formulae containing carbon and hydrogen atoms were more frequently found in positive-ion mode, whereas negative-ion mode was more sensitive for heavy-metal-containing ions and acidic sulphate species. Deprotonation is known to favour the formation of carboxylate anions; thus, they are also found more frequently within the negatively charged ions. Although a similar amount of carbon black is found for all samples, its content within the negatively charged ions is much higher. The smallest variations within one polarity for both sampling locations were found in the carbon black content with relative numbers between 18 and 25% for the negatively charged ions (Fig. 2a–d) and significantly lower 3 to 5% (Fig. 2e–h) for the positively charged ions. If one takes the sum of the shares of these compounds (23 to 29%) for both polarities, the fluctuations between cities and sampling times were even smaller.

The most significant difference between the two cities was found in the amount of sulphur-containing organic compounds in negative-ion mode, which were very prominent in Tehran (11 and 11%) and almost absent in the samples from Hangzhou (3 and 2%). Since more than 90% of SO_2 emissions in urban areas are caused by industrial processes, power generation and transportation, this dramatic difference can be attributed mainly to the SO_2 air pollution control policy in China that strongly regulates sulphur dioxide emissions since 2000 [42]. After the first implementations of filter systems in the year 2006, the SO_2 emissions declined until the recent years as shown by van der A et al. [43]. Larger differences were also found for CHON and CHN compounds in positive-ion mode, which seems to be more sensitive for those nitrogen-containing compound classes. Here too, the shares in Tehran with 30% and 31% relative assigned sum formulae number were more than double of those in Hangzhou with 13% and 12%. We assume that mainly traffic-related sources are responsible for these nitrogenous organic compounds, because the sampling in Tehran was carried out near a heavily frequented highway [44, 45].

As Fig. 2 illustrates, the inorganic compounds are responsible for more than 12% of all signals in the respective sample and polarity. This is the case in both positive- and negative-ion mode, whereas the proportion in negative-ion mode is higher with 23 to 38% compared to 12 to 19% in positive-ion mode. All inorganic species that have been assigned are characterized by the absence of carbon and hydrogen species in their respective molecular formulae. The majority of this ion class consists of alkali and alkaline earth metals, but a large number of heavy-metal-containing molecular formulae also belong to this group, which includes iron, copper,

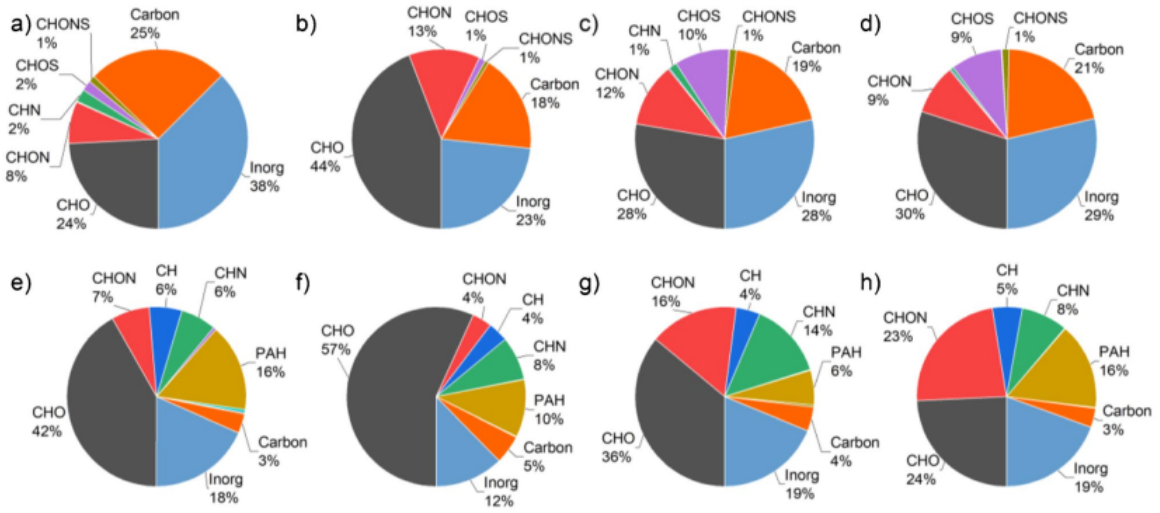

Fig. 2 Assigned sum formulae grouped into 11 classes in negative- (**a–d**) and positive-ion mode (**e–h**). Measurements of the Chinese filters on day 1 (FPI17B0807, **a**, **e**) and day 2 (FPI17B0811, **b**, **f**) as well as for the Iranian filters on day 1 (287, **c**, **g**) and day 2 (289, **d**, **h**) exhibit characteristic features for each sampling location

manganese, zinc, titanium, lead, chromium, nickel, arsenic, tin, cadmium, silver and cerium in decreasing order of relative content. Among them, only tin, silver and cerium have been detected as positively charged ions, while arsenic and cadmium in particular have been detected as negatively charged ions. Despite the overall lower number of assigned sum formulas in Tehran compared to Hangzhou, the number of assigned heavy metal species was higher in Iranian compared to Chinese samples by a factor of 1.2 and 1.7 for positively and negatively charged ions, respectively.

The total share of CHO-containing sum formulae ranges from 24 to 44% among the negatively charged ions and from 24 to 57% among the positively charged ions for both cities. The differences in aerosol composition between both sampling days, especially concerning CHO and inorganic species in positive-ion mode, were particularly remarkable in Hangzhou, whereas only minor differences were found in both samples from Tehran in all compound groups. In Hangzhou, a drastic change in particle composition was observed between days 1 and 2, especially for the negatively charged ions, starting from a strongly inorganic aerosol on day 1 (carbon + inorganic = 63%) to an organic-dominated aerosol on day 2 (carbon + inorganic = 41%). The relative number of CHO-containing species found in our study is in good agreement with other studies measured in south China and Singapore [46, 47]. Since we are able to detect and report other classes of compounds in addition to CHO compounds, such as large carbon fragments, inorganic compounds and PAHs, the relative proportion of CHO compounds is reduced compared to other studies [48]. If we count only organic compounds, the relative percentage of CHO-containing compounds rises to levels between 53 and 75%, as found in other studies [49].

In positive-ion mode, ion formation involves cationization and direct photoionization, leading to the formation of positively charged metal adduct and radical cations, respectively. It has been shown that PAH detection on carbonaceous compounds is supported by the higher UV absorption of elemental carbon. Due to the laser wavelength of 343 nm, unselective REMPI processes, in addition to the previously mentioned ion formation mechanisms, may also be responsible for the high number of PAH compounds detected in the positive-ion mode [50].

A large proportion of the polycyclic aromatic hydrocarbons (PAH) was detected in positive-ion mode and values for all samples ranged from 6 to 16%. Assigned substances belonging to this class included not only carbon- and hydrogen-based PAHs, but also those containing nitrogen (amino PAHs) and oxygen atoms (oxy-PAHs). While precursor PAHs from industrial processes, coal combustion and vehicle exhaust are mostly emitted as primary particles, their oxidation products provide evidence of aerosol ageing by photochemical processes or reactions with nitrate radicals, OH radicals and ozone [51]. Prominent representatives of these oxidation products are oxy-PAHs. To form oxy-PAHs from precursor PAHs, two conditions must be met: a sufficient time (typically a few hours) for the reaction to run its course and the presence of ozone or OH radicals [52, 53]. For fresh particles, the number of PAHs is expected to be higher than that of oxy-PAHs [54]. As an example, we chose benzo(a)pyrene (B[*a*]P, *m*/*z* 252.093), benz[a]anthracene (*m*/*z* 228.093) and pentacene (*m*/*z* 278.109) and their oxy-PAHs B[*a*]P-dione ($[M+H]^+$ at *m*/*z* 283.075), benz[a]anthracenedione ($[M]^{\bullet+}$ at *m*/*z* 258.068) and pentacenedione ($[M]^{\bullet+}$ at *m*/*z* 308.083). All three PAHs were found in the Chinese and Iranian samples, but the corresponding oxy-PAHs could only be detected in the Chinese samples. This indicates that the Iranian samples were exposed to oxidizing compounds in the atmosphere for a limited time only, as these reactions are typically fast and occur within minutes to a few hours [55]. Reactions during sampling, storage and ionization can thus also be ruled out. Subdividing the PAHs into precursor and oxy-PAHs shows that the difference between Tehran and Hangzhou is mainly caused by the number of oxidized species, which is by a factor of 3.6 higher in the Hangzhou samples. Many of the detected CHN and CHON compounds are also potential PAH species, but have not been explicitly identified as PAHs. Since we found that the total particle concentration of the sample FPI17B0807 is 1.6 times higher than that of the sample FPI17B0811, despite the larger number of assigned sum formulae in the latter compared to the former, we assume that the high content of inorganic compounds contributes to the larger mass.

Most studies using ESI or other soft ionization techniques either for analysis of filter extracts or direct chemical characterization of aerosol particles on filters focus on protonated or deprotonated organic compounds [56, 57]. Here, we were able to detect inorganic molecules, inorganic carbon fragments and organic substances, which were either not detected within measurements using only a single analytical method in other studies or were not considered, but which are of great importance for the comprehensive interpretation of aerosol filter mass spectra. The increased number of nitrogenous and sulphur compounds in Tehran compared to Hangzhou is in line with regional particle sources such as traffic in the first case, and the overall increased pollution from unfiltered industrial waste gases in the second case. This shows that, when measuring with only one ion polarity, an extremely large number of compounds, including PAHs, certain heavy metal species, sulphates and CHN compounds can only be determined partially or not at all.

Double-bond equivalents of detected organic compounds

The double-bond equivalents (DBEs) of organic molecules is a structural descriptor that helps to separate compounds

into groups. For example, oxidized compounds or aromatics group together based on DBEs. From this, the ageing behaviour of particles can be assessed, among other things. Figure 3 shows DBEs for each associated molecule categorized as CHO, CHON, CH, CHN, CHOS, PAH, CHNS, CHS or CHONS. The number of carbon atoms is plotted against the number of DBEs and the number of matching molecular formulae is indicated by the area of the data points. In general, the number of DBEs of all compounds was higher in the Hangzhou samples compared to the Tehran samples.

Especially, the samples from Tehran showed very similar horizontal and vertical distributions for the same ion classes in the negative-ion mode (Fig. 3c and d). Primarily, sulphur-containing compounds in the form of CHOS were observed in the two Tehran samples, but mostly for DBEs below 7. In the same carbon number and DBE regions, mainly CHO compounds were detected in the samples from Hangzhou, but in lower relative quantities than the sulphur compounds in Tehran. The class of CHO compounds was predominantly grouped above a DBE of 5 for the negatively charged ions and below 10 for the positively charged ions. Apart from this, the patterns of negatively charged molecules were similar in both cities, except for sample FPI17B0807 in Fig. 3a. Here, we found lower relative numbers of all compounds, especially in the region between 9 and 13 carbon atoms. The positively charged ions were somewhat more meaningful, mainly due to the assigned PAHs. These showed the highest number of DBEs.

An average DBE was calculated for the different classes, from which the unsaturation could be estimated and compared between the two megacities. Only the most prominent classes with more than 10 compounds were used for comparison in order to obtain appropriate statistics. The evaluation was performed for positive-ion mode. For CHO compounds, the average DBEs of both cities were similar, with DBE_{avg}(Hangzhou) = 1.9 and 3.5 and DBE_{avg}(Tehran) = 2.1 and 3.5 for days 1 and 2, respectively. Differences were found for the class of CHON compounds, with increased unsaturation observed in Tehran (DBE_{avg} = 6.3 and 6.4) compared to Hangzhou (DBEavg = 3.0 and 6.5), indicating higher oxidation of nitrogenous compounds, implying a contribution from car exhaust gases.

For the more hydrocarbon-based structures such as PAH and CH compounds, the situation changed due to the higher unsaturation of both classes in Hangzhou compared to Tehran. Especially, the PAHs from Hangzhou were found to

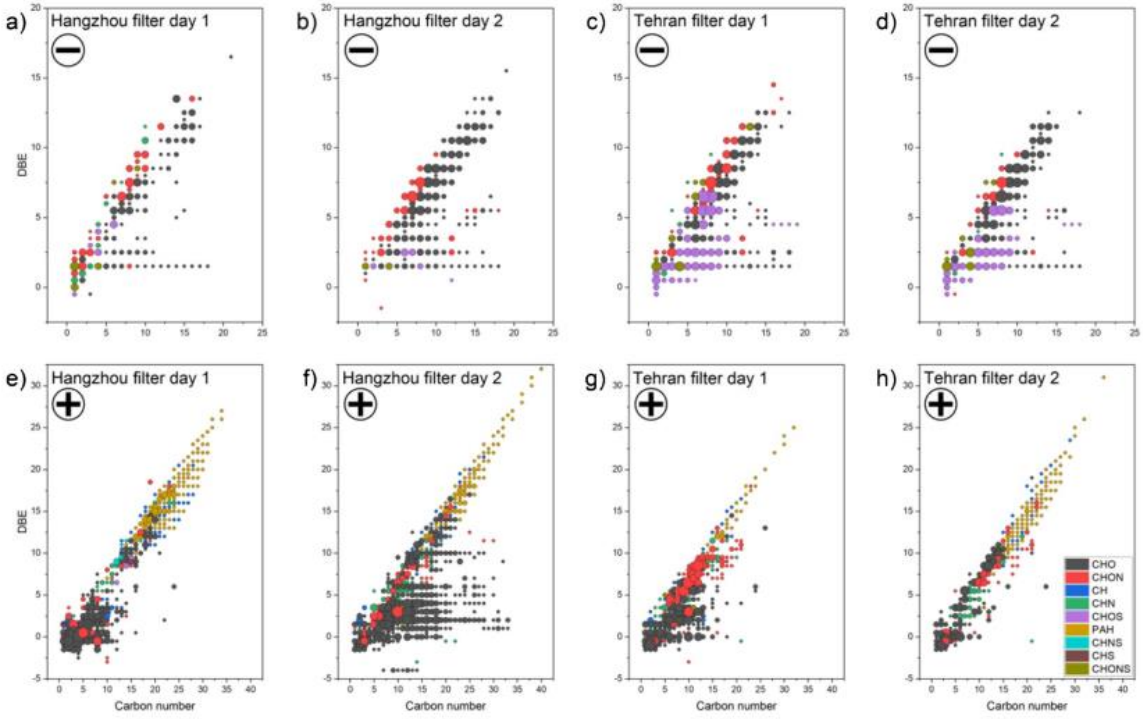

Fig. 3 Plots showing the number of double-bond equivalents for 9 classes of organic molecules in negative- (**a–d**) and positive-ion mode (**e–h**). The Chinese filters on day 1 (FPI17B0807, **a**, **e**) and day 2 (FPI17B0811, **b**, **f**) as well as the Iranian filters on day 1 (287, **c**, **g**) and day 2 (289, **d**, **h**) are shown. The area of each data point corresponds to the number of compounds

have significantly higher DBEs (DBE_{avg}(Hangzhou) = 16.1 and 16.5, DBE_{avg}(Tehran) = 13.0 and 14.2). This may be a consequence of a longer transport of the PAHs in the atmosphere. It has been shown that with the higher molecular weight of the PAHs and higher unsaturation, stronger adsorption to the particle phase is associated, which allows these compounds to remain longer in the atmosphere [58, 59]. This observation is in good agreement with the higher oxidation observed for the Hangzhou PAH fraction. As a result, the PAHs found in Hangzhou may come from more distant sources like coal combustion, remote traffic and other industry. Sample FPI17B0811 (Fig. 3b and f) also showed that there is a trend towards higher DBE if the number of CHO compounds rises. The lower-molecular-weight PAHs in Tehran may have different sources, but these were confined to the immediate vicinity of the sampling point, and were thus mainly restricted to car exhaust. The gap between DBE 5 and 8 of the Chinese sample from day 1 is mainly due to the lack of CHO and CHON species with corresponding DBEs.

Distinguishing between Tehran and Hangzhou on the basis of characteristic compounds

The samples from Tehran and Hangzhou were distinguished by statistical evaluation of *m/z* signal identities and intensities, as shown in SI Fig. 3. For this purpose, 168 and 186 significant compounds were identified for negative- and positive-ion mode by means of a Student t-test and clustered using HCA, respectively. SI Fig. 3 shows that by using these significant compounds, both cities can be easily separated, due to either very low or zero compound intensities (blue colour) or high compound intensities (red colour). The individual sum formulas are not easily readable due to their large number and are therefore listed in detail in SI Table 3.

In the case of the negatively charged ions in SI Fig. 3a, few compounds were found that were characteristic for the Hangzhou samples. These few compounds included mainly inorganic nitrate clusters with 3 to 5 nitrogen and 9 to 15 oxygen atoms. These compounds can be associated with NO_x emissions from traffic-related sources, but may also result from the reduced SO_2 emissions in China [60, 61]. Low SO_2 conditions favour the formation of secondary inorganic aerosols (SIAs) with high nitrate content. This is typically observed when the gaseous nitrate is converted to HNO_3 and neutralized by atmospheric ammonia NH_4^+ [62]. These secondary inorganic nitrate particles are found several kilometres from their source due to their long atmospheric lifetime and small size [63]. Furthermore, NH_4NO_3 evaporates significantly (> 80% at 35 °C and 18% rel. humidity) by sampling in a dry and warm environment as in Tehran, and can additionally react with sulphuric acid to form HNO_3 (g) [64, 65]. In both cases, the nitrogen content in the particle phase in Tehran will consequently be reduced and significantly lower amounts were detected, while the conditions in China would lead to much lower losses of particulate nitrate.

The characteristic negatively charged ions from Tehran samples included a large variety of different inorganic and organic species. From these, 76 out of 159 compounds contained sulphur atoms which makes the sulphur content the best distinguishing feature between Tehran and Hangzhou. Some silicates, organic nitrates as well as inorganic copper, iron and zinc compounds were found as well.

For the positively charged ions in SI Fig. 3b, mainly high molecular PAHs and oxy-PAHs, some CHN species and inorganic calcium were found to be characteristic for Hangzhou, while Tehran samples were dominated by lower-molecular-weight PAHs, CHON species and inorganic chromium compounds. Until now, the data allows for a differentiation of the two cities based on the bulk particle composition of the whole filter. However, by looking at a very restricted area on the filter surface and extracting the chemical information for this area, as shown in the following chapter, the characterization of individual particles can be approached.

Particle-based classification

LDI imaging as a technique for untargeted analysis of aerosol filter samples under atmospheric pressure is not only capable of characterizing filter samples as bulk material but also allows for the characterization of small communities of particles. This is necessary to evaluate the composition of single particles or particle groups in terms of source apportionment and mixing state. For this approach, the location and composition of each mass spectrum in the imaging data set is correlated with each other on a statistical basis. Sum formulae on the filter surface are grouped based on their location and signal intensity. As a result, different particle classes (data clusters) within groups of particles were identified. These identifications of particle classes on filter samples have so far been possible mainly on the basis of classes of molecules with structurally similar properties, such as lipid species with different head groups, carbohydrates, alkanes and terpene compounds, determined by chromatographic MS techniques. Identification, based on the association of structurally very different compounds in the same particle, such as those occurring in highly internally mixed aerosol particles, has been rather challenging [66]. A major advantage of the method is that both inorganic and organic compounds can be detected and that both can occur in the same data cluster and, thus, in a small group of particles. Conclusions about the mixing of different chemical components in the particles, their ageing or the composition of the underlying primary particles (mineral, black carbon or organic) are thus possible.

In addition, the distribution of single particles on the filter surface, agglomeration effects and the shape of larger particles is also accessible with the method. Since the laser focus diameter was about 50 µm, there were certainly several particles assembled within this ablation area, which were ionized simultaneously and thus produced a mass spectrum corresponding to a small group of particles and not to a single particle. If, however, very specific *m/z* signals repeatedly occur together in certain spectra, the probability that these signals belong to individual particles rather than to particle agglomerates increases with the number of spectra measured.

The size and composition of a data cluster was one criterion to explain particle transport, composition and source. Overall, there was a larger number of small clusters (< 10 compounds) observed in the negative-ion mode compared to the positive-ion mode. From a chemical point of view, the smaller data clusters in negative-ion mode mostly consist of inorganic compounds containing elements such as iron, titanium, copper, silicon, phosphate and sulphate while in positive-ion mode, smaller CHO, CHON and CHN clusters were found more frequently. The smaller inorganic data clusters are mainly due to metal abrasion and mineral fragments, as there is little mixing of different metal species with organic compounds. The organic components that were found in such small data clusters are often linked by consecutive losses of C, H and/or O from a parent compound.

Larger data clusters indicate internally mixed particle groups or primary particles consisting of mixtures of different substances. For example, PAH particles, which generally contain a larger number of different low- and high-molecular-weight PAH species, are more common in positive-ion mode. It is expected that during the chemical conversion of compounds and the adsorption of new compounds, larger data clusters containing a larger number of signals will be formed. From these larger data clusters, the evolution of the underlying particles can be traced, so that an assignment of the particle source, the particle age and its transformation in the atmosphere is possible. For larger data clusters (> 30 compounds), representative spectral patterns were obtained for the sample FPI17B0807 from Hangzhou (Fig. 4) and the sample 287 from Tehran (Fig. 5). Both samples showed the highest particle concentrations and were selected on this basis. Shown are averaged intensities of signals that were assigned to the respective data cluster. The structure of the clusters was also used to verify the plausibility of individual sum formulae, for example if they contained the same atoms or molecular fragments as other ions of the same cluster. This helped to identify the data clusters and name them according to the assigned compound classes.

All measured samples had a number of specific data clusters in common. Prominent representatives here are mainly black carbon, mineral clusters and PAHs. Black carbon, which is produced by the incomplete combustion of fossil fuels, biomass and biofuels is largely found in both cities. The data clusters in Fig. 4i, l and n as well as in Fig. 5e, o and s show typical patterns of carbon fragments, divided into data clusters with low-molecular-weight (C_4–C_{22}) and higher-molecular-weight (C_{13}–C_{34}) species. This suggests that the carbon chains of different lengths are grouped together in different particles and subsequently may come from different sources. Mineral clusters in Figs. 4j and 5b, r mostly contain a mixture of the elements Al, Ca, Fe, Mn, Mg, Si and Ti. Data clusters of PAHs were found in both the Hangzhou sample and the Tehran sample but patterns of PAHs in the spectra differ. Whereas the clusters in Figs. 4g and 5d contain only PAHs, the data clusters in Fig. 5a and f show mixtures of PAHs with amines and plant compounds. Mainly high-molecular-weight species of PAHs were found in Hangzhou and low-molecular-weight species in Tehran. The data cluster with aromatic amines in Fig. 5a is of particular interest, because these compounds are very often classified as carcinogens and arise mainly from coal combustion activities in the respective region, but can also be attributed to cigarette smoke [67, 68]. Therefore, low-molecular-weight PAH compounds found in this data cluster can also be derived from these kinds of sources but are typically present in traffic emissions as well [69]. Especially, smaller ions like $C_9H_7^+$ may also be fragments of larger PAH species like substituted naphthalenes, which was shown by Koptyug et al. [70]. Mixed clusters of heavy metals and sulphate (Fig. 5l), as well as zinc and sulphate (Fig. 5k) are also likely to be due to the combustion of coal. These observations are in good agreement with the higher number of heavy-metal-containing clusters (esp. sulphates and chlorides in negative-ion mode) in Tehran in general (Fig. 5j, k, l, m, n and p). None of the larger data clusters in Hangzhou in Fig. 4 are dominated by heavy metals such as Zn, Pb, Ni, Cr and As, associated with strong adverse health effects [71, 72]. These toxic elements only play a minor role in data clusters 4 d and 5 o. Figure 4d also shows intensive signals of phthalates, which are ubiquitous and cannot be assigned to any specific source.

Plant materials such as sugars (Fig. 4a), alkaloids (Fig. 5i), fatty acids (Figs. 4m and 5p, t) and other biogenic volatile organic compounds (Fig. 4k and 5f, j) were found as components of a variety of data clusters. While in Hangzhou there were only three data clusters associated with plant material, which also showed little mixing with other substances, in Tehran plant material was found in five data clusters and usually highly internally mixed. Secondary organic aerosols (SOA) were often part of these data clusters, but in both Hangzhou and Tehran samples, they were usually mixed with black carbon (Fig. 4i), fatty and other organic acids (Figs. 4m and 5t) and heavy metals (Fig. 5j, m, n). SOA were characterized by a number of oxidized

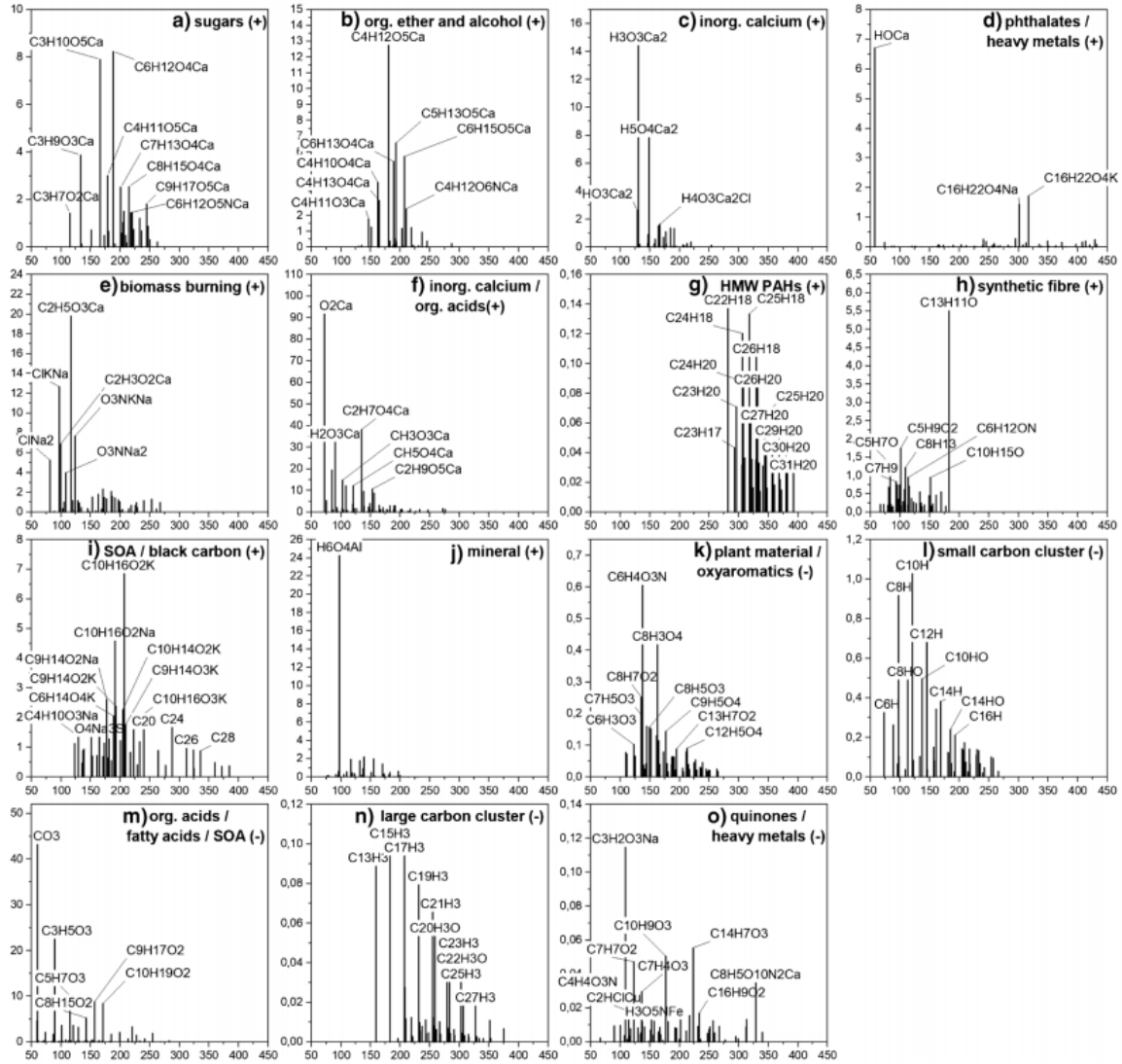

Fig. 4 Representative mass spectral patterns for larger data clusters (> 30 sum formulas) for the Hangzhou sample FPI17B0807. A total of 15 data clusters, 10 for positively charged ions (**a–j**) and 5 for the negatively charged ions (**k–o**) were found and assigned to different particle types

terpenes and ketoaldehydes like camphoric acid ($C_{10}H_{16}O_4$), 2.3-dihydroxy-4-oxopentanoic acid ($C_5H_8O_5$), phthalic acid ($C_8H_6O_4$), 4-methyl-5-nitrocatechol ($C_7H_7NO_4$), succinic acid ($C_4H_6O_4$), cis-pinonic acid ($C_{10}H_{16}O_3$) and pinic acid ($C_9H_{14}O_4$), all of them identified as markers of SOA in numerous in-situ and smog chamber studies, in both ozone and OH oxidation reactions [73–77]. All these compounds were found as $[M\text{-}H]^-$ ions, except pinonic acid, which was also detected as $[M+K]^+$ in the data cluster in Fig. 4i.

Calcium was one of the main components found in the Hangzhou sample, it occurred in inorganic and organic compounds and generally favored the formation of positively charged ions. Since calcium was also the main component responsible for the high inorganic content of this sample, we assume that a large proportion of mineral dust in the form of calcium carbonate particles specifically contributed to the formation of this aerosol. Typical sources of calcium carbonate are desert sand particles and sea spray aerosols [78, 79]. Two data clusters dominated by calcium compounds are shown in Fig. 4c, consisting of pure inorganic calcium and Fig. 4f, with a mixture of small organic acids and calcium. One data cluster from Tehran in Fig. 5h was likewise

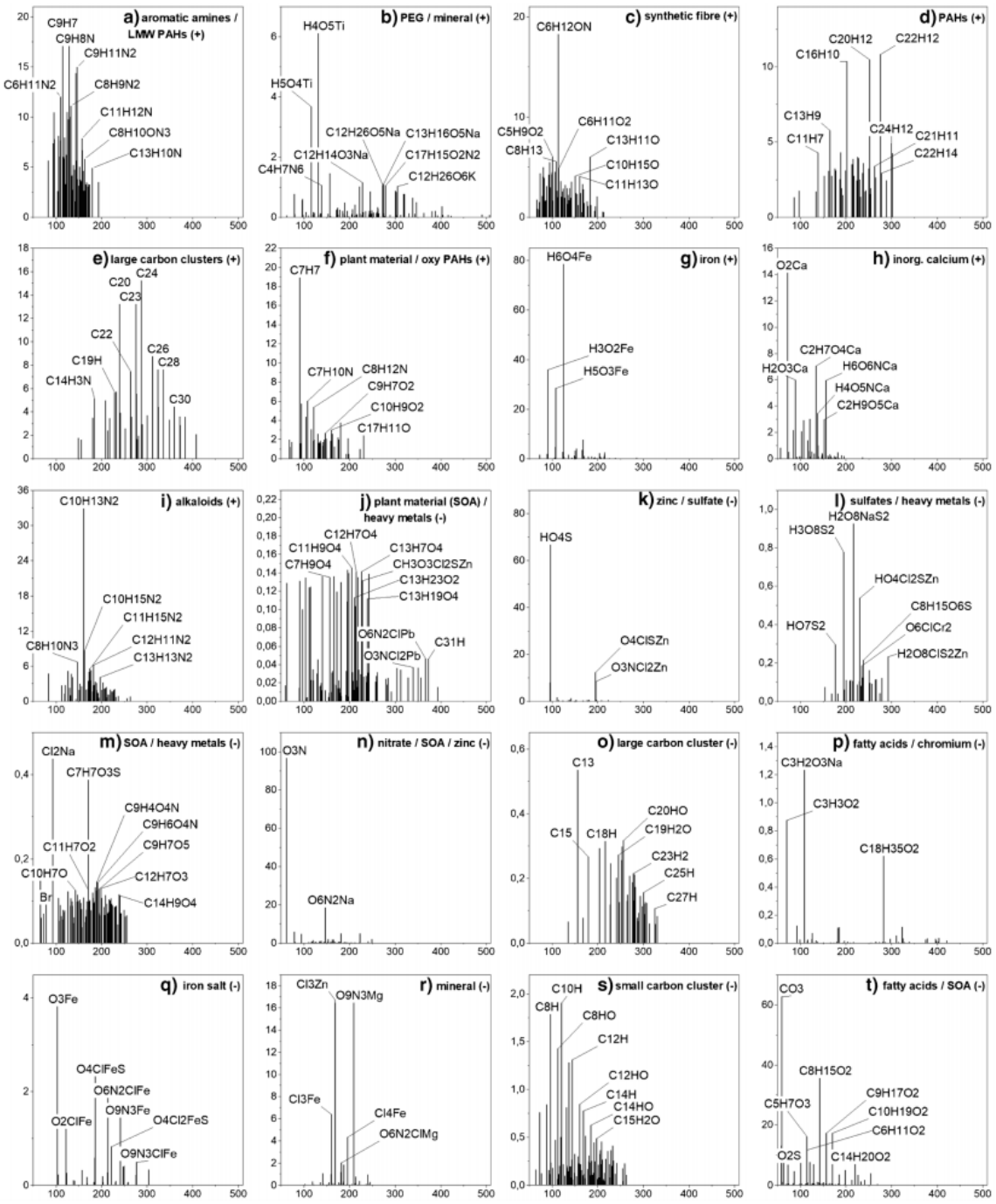

Fig. 5 Representative mass spectral patterns for larger data clusters (> 30 sum formulas) for the Tehran sample 287. A total of 20 data clusters, 9 for positively charged ions (**a–i**) and 11 for the negatively charged ions (**j–t**) were found and assigned to different particle types

composed of inorganic calcium, but the remaining data clusters showed only few calcium-based compounds.

A very interesting feature in both cities were two data clusters (Figs. 4h and 5c), which contained a number of compounds whose molecular formulas can be assigned to caprolactam ($C_6H_{11}ON$) and methyl methacrylate ($C_5H_8O_2$). These two prominent compounds are mainly associated with synthetic fibres, such as nylon and other plastics. Despite their use as synthetic fibres, caprolactam is used in many industrial manufacturing activities and has been found in $PM_{2.5}$ aerosols in a Canadian study in significant levels as well [80].

Some data clusters were found to be specific for the respective city. Among the calcium-rich clusters in Hangzhou and the heavy-metal-containing clusters in Tehran, the data clusters in Fig. 4b and e are particularly noteworthy for the Chinese location. While the former consists mainly of smaller organic compounds such as ethers and alcohols and has no specific characteristics, the latter is clearly characterized by sum formulas associated with levoglucosan ($C_6H_{10}O_5$), mannose and mannitol ($C_6H_{14}O_6$), all markers of biomass combustion. Levoglucosan was found in the sample from Tehran as well, but mixed with SOA and heavy metals in data cluster m. Levoglucosan ions were detected as $[M+K]^+$, $[M+Na]^+$ and also $[M\text{-}H]^-$.

In Tehran, we found two data clusters, one in positive- (Fig. 5g) and one in negative-ion mode (Fig. 5q), that included mainly inorganic iron in the form of water clusters as positive ions and in the form of nitrates, sulphates and chlorides as negative ions. Both were likely arising from combustion processes emitting iron oxide particles which are transformed in the presence of SO_2, HCl and NO_x to form the observed compounds. Weber et al. [81] identified iron emissions from waste incineration and coal power plants.

Many of the identified data clusters are in good agreement with organic aerosol classes found for the Chinese megacity Nanjing [66]. Some studies show that it is possible to differentiate between different stages of oxygenation and carbon numbers, for example by aerosol mass spectrometers, but their interpretations are restricted to mainly fragments of compounds rather than intact parent ions [82, 83]. Rivellini et al. [47] differentiated less oxidized oxygenated organic aerosol and more oxidized oxygenated organic aerosol by ratios of $C_2H_3O^+$ plus CO_2^+ to CO_2^+ on a quantitative basis. They also pointed out that by measuring additional refractory metals, attributing particle sources becomes more reliable compared to our approach. Using mixtures of metal ions and organic parent compounds grouped together in our data clusters allowed us to differentiate more easily between different sources. This was particularly meaningful in the case of terpenes for secondary biogenic organic aerosol, or levoglucosan mixed with small sodium and potassium ions in case of biomass burning. Especially, the occurrence of heavy metals mixed with PAHs and SOA in the samples from Tehran is of concern. A larger number of signals containing chromium, lead and arsenic were found in the majority of data clusters from Tehran. Especially, zinc and chromium, which were both data clustered together with the majority of CHOS compounds in Fig. 5k and l, clearly show that the emission of organic sulphur compounds is accompanied by an increased amount of toxic heavy metals. Some of the substances alone are already harmful to health, while a mixture of different sources was found here. The high quantities of harmful substances found show that negative health consequences can be expected, especially on days with very high particle loads. For some of the PAHs, we implemented a quantification approach, which is shown in the following section.

Quantification of PAH species

Concentration series of 13 PAH compounds in dichloromethane were prepared and 1 µL of each dilution was spotted on the sample surface using the dried droplet method. Rasterizing the surface, followed by normalization to TIC allowed us to retrieve calibration curves with accuracies $R^2 \geq 0.85$ in 63% of all measurements as shown in Fig. 6 and SI Fig. 2. A few assumptions were made for the calculations. Since a standard solution suitable for LC or GC was used, containing also several PAHs with identical masses that can be separated chromatographically but not mass spectrometrically, it was assumed that each species with identical mass contributed equally to the intensity of the mass signal, meaning that these species have the same ionization and desorption properties on the filters. Due to this assumption, we list total concentrations of PAHs per mass and not per PAH species. Calibrations curves are shown in Fig. 6. Differences in ionization yields and signal intensities between the PAH species are expected due to their different vapour pressures, since the main reason for the ablation and desorption process is the explosive thermal decomposition of the carbon particles due to overheating [84]. However, this is true for all PAHs to the same extent, since the conditions and the substrate are homogeneously distributed.

Using the standard addition method, determined concentrations of low-molecular-weight PAHs (SI Fig. 2) were partly above 5000 µg/g and were thus significantly higher than high-molecular-weight species (181.5 to 1235 µg/g) (Fig. 6) for the Hangzhou and Tehran samples (Table 1). This effect is probably due to generally lower ion yields of low-molecular-weight compounds causing higher inaccuracies for the calibration curves but may also be the result of a calibration artifact, caused by the higher vapour pressure of the low-molecular-weight PAH species combined with a higher specific surface area of small particles: lowly

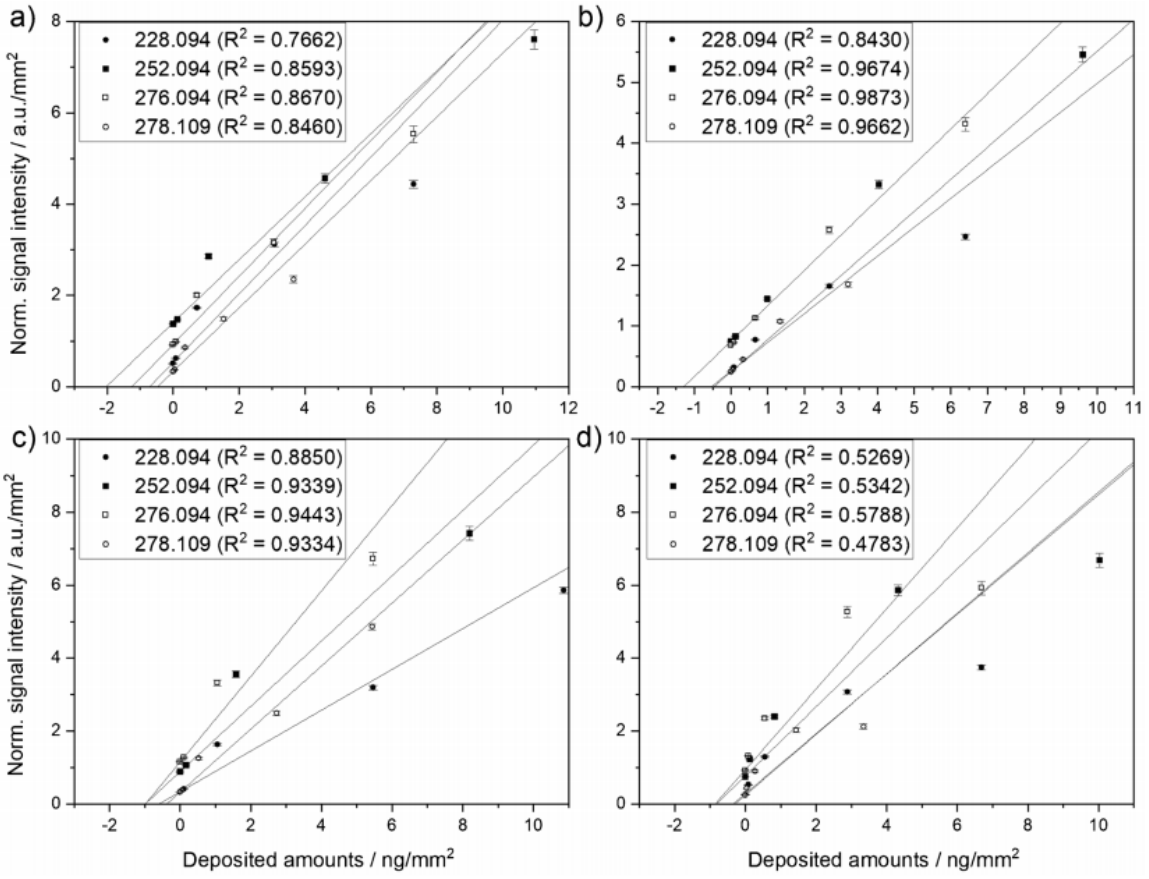

Fig. 6 Calibration curves for dried droplet standard addition method on Hangzhou samples FPI17B0807 (**a**), FPI17B0811 (**b**) and Tehran samples 287 (**c**) and 289 (**d**). Calibration curves are shown for high-molecular-weight PAHs

concentrated solutions of low-molecular-weight PAHs will adsorb on the high specific surface area of the small particles and only a small fraction will thus evaporate from the filter surface. With rising concentrations, a higher fraction of the low-molecular-weight PAHs will escape into the gas phase as non-surface-bound volatile substances. As a result, the lowly concentrated solutions of the highly volatile PAHs are found to have higher levels in the particulate phase than the higher concentrated solutions, as most of them have already entered the gas phase. This effect reduces the slope and linas these are present in the gas phase to about 4 to 50%, while the proportion of PAHs in the gas phase in species with more than 5 rings is less than 1%. For our study, the vapour pressures of the measured PAHs rise significantly between the three PAHs BaA and Chr at *m/z* 228.094 and Pyr at *m/z* 202.078 by one to three orders of magnitude, as can be seen from literature values ($P_{BaA} = 2.1 \times 10^{-7}$ mm Hg, $P_{Chr} = 6.23 \times 10^{-9}$ mm Hg and $P_{Pyr} = 4.5 \times 10^{-6}$ mm Hg) [85, 86]. Therefore, it is not surprising that for all PAHs heavier than *m/z* 202.078, we obtained values that are very


Inscribed form left (epiploic) section.

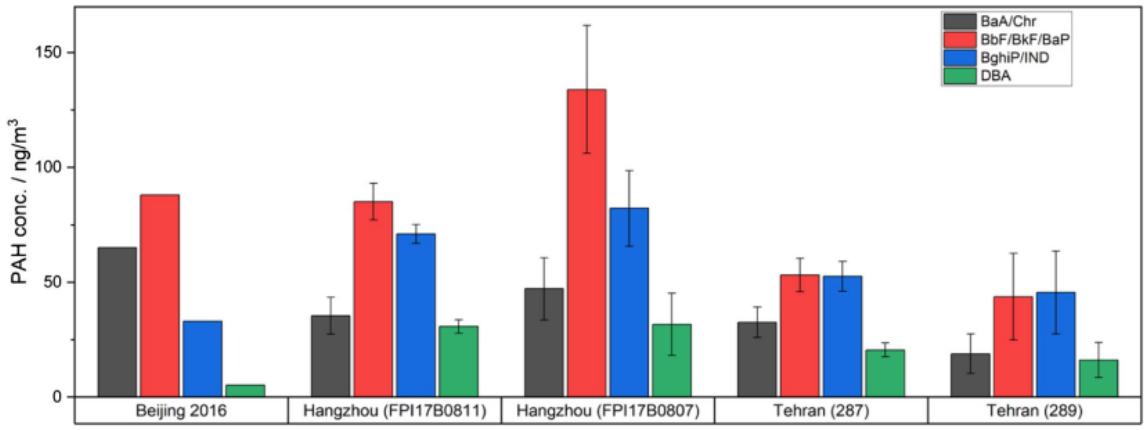

Fig. 7 Calculated concentrations of 4 selected PAH groups BaA/Chr, BbF/BkF/BaP, BghiP/IND and DBA for each Tehran and Hangzhou sample compared to values measured in Beijing during winter 2016 [88]

small organic and soot particles that contribute to the significantly high pollution of the air with carcinogenic and toxic substances in Tehran.

Conclusion and discussion

Ambient LDI MSI was used for the first time to unravel the chemical composition of aerosol particles collected on quartz fibre filters. An autofocusing MALDI MSI source was used to compensate for the extensive surface roughness of the filter and allowed for constant and high ion signals throughout the whole ablated area. An ultrahigh-resolution orbital trapping mass analyzer was used to differentiate very small differences in *m/z* values and to assign more than 3200 m/*z* signals with chemical sum formulas in positive- and negative-ion mode for two filters from Iran and China, respectively, quite a number of them as intact molecular compounds instead of fragments, as would be expected based on the ionization method. The addition of a matrix as in MALDI experiments was not necessary, as particle absorbances were sufficiently high in general and particularly PAH ionization was supported by the higher UV absorption of elemental carbon present on the filters [89]. Since our approach, using scanning laser desorption/ionization mass spectrometry, is an offline technique where particles are collected, stored and brought to the laboratory, particle compositions may change by chemical reactions or evaporation before analysis.

The lower number of sulphur compounds detected in Hangzhou may indicate a successful Chinese sulphur dioxide emission policy. This led to a significant reduction of sulphuric acid contents in the particles. As the proportion of nitrogen oxide compounds was also lower in our measurements, it can be assumed that the exposure to nitric acid and its reaction products was also reduced. Since it has been shown that the influence of acidic sulphur compounds can lead to a reduction in the number and concentration of nitrate-containing compounds on filter samples, the actual difference is probably even larger [38]. It is alarming that, despite the mass loadings of the filters from Tehran were by a factor of 3 or more lower than in Hangzhou, the number of heavy-metal-containing compounds was up to 1.7 times higher and PAHs showed nearly double the concentrations as in Hangzhou. This raises concerns about the exposure of the population in Tehran to toxic pollutants, especially during periods of very high particulate matter concentrations. PAH concentrations determined by a standard addition method on the filter surface allowed quantification of these harmful substances. However, we were able to show that this method is only suitable for higher-molecular-weight PAHs with low vapour pressure, as measurement artifacts occur due to the application of the solutions and delayed measurements. Nevertheless, the total number of assigned sum formulae and especially of assigned CHO and PAH species was higher in Hangzhou than in Tehran.

As can be seen from our data, there are realistic concerns about a major influence of air pollution in both countries on the environment as well as on the health of the population [90]. The improvement of efficiency in the energy-producing sector and the use of modern filter systems are essential points that can contribute to the reduction of the quantity and danger of harmful particles. China is leading the way in this respect with its restrictive measures, resulting in a reduction of atmospheric pollutants. Our results show a reduced number of sulphates, nitrogen oxides, heavy metals and PAHs in the measured particles from China, while in Iran, despite a significantly lower quantity of particles during our sampling

period, the risk potential can be estimated to be much higher due to stronger pollution by heavy metals, PAHs and higher-oxidized nitrogen-containing compounds.

The presented method offers the possibility to quickly and easily access a variety of organic or inorganic molecular information in aerosol particles collected on filter samples. Reliable source apportionment enables the identification of emitters of certain particle populations and can be used as a tool to reduce the emission of selected pollutants.

Supplementary Information The online version contains supplementary material available at https://doi.org/10.1007/s00216-022-04275-1.

Acknowledgements We thank Focused Photonics Inc., Hangzhou, China, and Yousef Rashidi, Shahid Beheshti University, Tehran, Iran, for collecting the filter samples.

Funding Open Access funding enabled and organized by Projekt DEAL. Financial support by the Deutsche Forschungsgemeinschaft (DFG), Germany, Grant No. HI 857/4–1, by the research program "Landes-Offensive zur Entwicklung Wissenschaftlich-oekonomischer Exzellenz – LOEWE", research focus "AmbiProbe", State of Hesse, Germany and technical support by TransMIT GmbH, Giessen, Germany, is received.

Declarations

Conflict of interest B. Spengler and K.-P. Hinz are consultants of TransMIT GmbH, Giessen, Germany. C. Barth declares to have no conflicts of interest.

References

1. World Health Organization. Ambient air pollution: a global assessment of exposure and burden of disease. Geneva: World Health Organization; 2016.
2. Mannucci PM, Franchini M. Health effects of ambient air pollution in developing countries. Int J Environ Res Public Health. 2017;14(9):1048. https://doi.org/10.3390/ijerph14091048.
3. Bourdrel T, Bind M-A, Béjot Y, Morel O, Argacha J-F. Cardiovascular effects of air pollution. Arch Cardiovasc Dis. 2017;110(11):634–42. https://doi.org/10.1016/j.acvd.2017.05.003.
4. Ko FWS, Hui DSC. Air pollution and chronic obstructive pulmonary disease. Respirology. 2012;17(3):395–401. https://doi.org/10.1111/j.1440-1843.2011.02112.x.
5. Lelieveld J, Klingmüller K, Pozzer A, Pöschl U, Fnais M, Daiber A, Münzel T. Cardiovascular disease burden from ambient air pollution in Europe reassessed using novel hazard ratio functions. Eur Heart J. 2019;40(20):1590–6. https://doi.org/10.1093/eurheartj/ehz135.
6. Tao J, Gao J, Zhang L, Zhang R, Che H, Zhang Z, Lin Z, Jing J, Cao J, Hsu S-C. PM 2.5 pollution in a megacity of southwest China: source apportionment and implication. Atmos Chem Phys. 2014;14(16):8679–99. https://doi.org/10.5194/acp-14-8679-2014.
7. Yang F, Tan J, Zhao Q, Du Z, He K, Ma Y, Duan F, Chen G. Characteristics of PM 2.5 speciation in representative megacities and across China. Atmos Chem Phys. 2011;11(11):5207–19. https://doi.org/10.5194/acp-11-5207-2011.
8. Rodríguez S, Alastuey A, Alonso-Pérez S, Querol X, Cuevas E, Abreu-Afonso J, Viana M, Pérez N, Pandolfi M, de La Rosa J. Transport of desert dust mixed with North African industrial pollutants in the subtropical Saharan air layer. Atmos Chem Phys. 2011;11(13):6663–85. https://doi.org/10.5194/acp-11-6663-2011.
9. World Health Organization (WHO). WHO global ambient air quality database: update 2018. Geneva: WHO; 2018.
10. Fujii H, Managi S, Kaneko S. Decomposition analysis of air pollution abatement in China: empirical study for ten industrial sectors from 1998 to 2009. J Clean Prod. 2013;59:22–31. https://doi.org/10.1016/j.jclepro.2013.06.059.
11. Lu Z, Zhang Q, Streets DG. Sulfur dioxide and primary carbonaceous aerosol emissions in China and India, 1996–2010. Atmos Chem Phys. 2011;11(18):9839–64. https://doi.org/10.5194/acp-11-9839-2011.
12. Farahat A. Air pollution in the Arabian Peninsula (Saudi Arabia, the United Arab Emirates, Kuwait, Qatar, Bahrain, and Oman): causes, effects, and aerosol categorization. Arab J Geosci. 2016;9(3):1–17. https://doi.org/10.1007/s12517-015-2203-y.
13. Li W, Sun S. Air pollution driving factors analysis: evidence from economically developed area in China. Environ Prog Sustainable Energy. 2016;35(4):1231–9. https://doi.org/10.1002/ep.12316.
14 Cheng Z, Li L, Liu J. Identifying the spatial effects and driving factors of urban PM2.5 pollution in China. Ecological Indicators. 2017;82:61–75. https://doi.org/10.1016/j.ecolind.2017.06.043.
15. Takegawa N, Sakurai H. Laboratory evaluation of a TSI condensation particle counter (model 3771) under airborne measurement conditions. Aerosol Sci Technol. 2011;45(2):272–83. https://doi.org/10.1080/02786826.2010.532839.
16. Belosi F, Santachiara G, Prodi F. Performance evaluation of four commercial optical particle counters. ACS. 2013;03(01):41–6. https://doi.org/10.4236/acs.2013.31006.
17. Park K, Kittelson DB, McMurry PH. A closure study of aerosol mass concentration measurements: comparison of values obtained with filters and by direct measurements of mass distributions. Atmos Environ. 2003;37(9–10):1223–30. https://doi.org/10.1016/S1352-2310(02)01016-6.
18. Peters TM, Chein H, Lundgren DA, Keady PB. Comparison and combination of aerosol size distributions measured with a low pressure impactor, differential mobility particle sizer, electrical aerosol analyzer, and aerodynamic particle sizer. Aerosol Sci Technol. 1993;19(3):396–405. https://doi.org/10.1080/02786829308959647.
19. Zhang XY, Wang YQ, Zhang XC, Guo W, Niu T, Gong SL, Yin Y, Zhao P, Jin JL, Yu M. Aerosol monitoring at multiple locations in China: contributions of EC and dust to aerosol light absorption. Tellus B Chem Phys Meteorol. 2008;60(4):647–56. https://doi.org/10.1111/j.1600-0889.2008.00359.x.
20. Nozière B, Kalberer M, Claeys M, Allan J, D'Anna B, Decesari S, Finessi E, Glasius M, Grgić I, Hamilton JF, Hoffmann T, Iinuma Y, Jaoui M, Kahnt A, Kampf CJ, Kourtchev I, Maenhaut W, Marsden N, Saarikoski S, Schnelle-Kreis J, Surratt JD, Szidat S, Szmigielski R, Wisthaler A. The molecular identification of organic compounds

in the atmosphere: state of the art and challenges. Chem Rev. 2015;115(10):3919–83. https://doi.org/10.1021/cr5003485.
21. Odabasi M, Ongan O, Cetin E. Quantitative analysis of volatile organic compounds (VOCs) in atmospheric particles. Atmos Environ. 2005;39(20):3763–70. https://doi.org/10.1016/j.atmosenv.2005.02.048.
22. Wan ECH, Yu JZ. Determination of sugar compounds in atmospheric aerosols by liquid chromatography combined with positive electrospray ionization mass spectrometry. J Chromatogr A. 2006;1107(1–2):175–81. https://doi.org/10.1016/j.chroma.2005.12.062.
23. Chandra Mouli P, Venkata Mohan S, Balaram V, Praveen Kumar M, Jayarama RS. A study on trace elemental composition of atmospheric aerosols at a semi-arid urban site using ICP-MS technique. Atmos Environ. 2006;40(1):136–46. https://doi.org/10.1016/j.atmosenv.2005.09.028.
24. Henning S. Seasonal variation of water-soluble ions of the aerosol at the high-alpine site Jungfraujoch (3580 m asl). J Geophys Res. 2003;108(D1). https://doi.org/10.1029/2002JD002439
25. Kiss G. Sample preparation of atmospheric aerosol for the determination of carbonyl compounds. Talanta. 1999;48(4):755–62. https://doi.org/10.1016/S0039-9140(98)00092-7.
26. Aldabe J, Santamaría C, Elustondo D, Lasheras E, Santamaría JM. Application of microwave digestion and ICP-MS to simultaneous analysis of major and trace elements in aerosol samples collected on quartz filters. Anal Methods. 2013;5(2):554–9. https://doi.org/10.1039/C2AY25724F.
27. Chow JC. Measurement methods to determine compliance with ambient air quality standards for suspended particles. J Air Waste Manag Assoc. 1995;45(5):320–82. https://doi.org/10.1080/10473289.1995.10467369.
28. Akyüz M. Simultaneous determination of aliphatic and aromatic amines in ambient air and airborne particulate matters by gas chromatography-mass spectrometry. Atmos Environ. 2008;42(16):3809–19. https://doi.org/10.1016/j.atmosenv.2007.12.057.
29. Hinz K-P, Kaufmann R, Spengler B. Laser-induced mass analysis of single particles in the airborne state. Anal Chem. 1994;66(13):2071–6. https://doi.org/10.1021/ac00085a023.
30. Sinha MP. Laser-induced volatilization and ionization of microparticles. Rev Sci Instrum. 1984;55(6):886–91. https://doi.org/10.1063/1.1137851.
31. Hinz K-P, Spengler B. Instrumentation, data evaluation and quantification in on-line aerosol mass spectrometry. J Mass Spectrom. 2007;42(7):843–60. https://doi.org/10.1002/jms.1262.
32. Li L, Liu L, Xu L, Li M, Li X, Gao W, Huang Z, Cheng P. Improvement in the mass resolution of single particle mass spectrometry using delayed ion extraction. J Am Soc Mass Spectrom. 2018;29(10):2105–9. https://doi.org/10.1007/s13361-018-2037-4.
33. Paschke C, Leisner A, Hester A, Maass K, Guenther S, Bouschen W, Spengler B. Mirion–a software package for automatic processing of mass spectrometric images. J Am Soc Mass Spectrom. 2013;24(8):1296–306. https://doi.org/10.1007/s13361-013-0667-0.
34. Robichaud G, Garrard KP, Barry JA, Muddiman DC. MSiReader: an open-source interface to view and analyze high resolving power MS imaging files on Matlab platform. J Am Soc Mass Spectrom. 2013;24(5):718–21. https://doi.org/10.1007/s13361-013-0607-z.
35. Tyanova S, Temu T, Sinitcyn P, Carlson A, Hein MY, Geiger T, Mann M, Cox J. The Perseus computational platform for comprehensive analysis of (prote)omics data. Nat Methods. 2016;13(9):731–40. https://doi.org/10.1038/nmeth.3901.
36. WorldWeatherOnline.com. Hangzhou monthly climate averages. 2020. https://www.worldweatheronline.com/lang/de/hangzhou-weather-averages/zhejiang/cn.aspx. Accessed 27 Aug 2020.
37. WorldWeatherOnline.com. Teheran monthly climate averages. 2020. https://www.worldweatheronline.com/teheran-weather-averages/tehran/ir.aspx. Accessed 27 Aug 2020.
38. Forrest J, Tanner RL, Spandau D, D'uttavio T, Newman L. Determination of total inorganic nitrate utilizing collection of nitric acid on NaCl—impregnated filters. Atmos Environ (1967). 1980;14(1):137–44. https://doi.org/10.1016/0004-6981(80)90117-1.
39. Reinard MS, Johnston MV. Ion formation mechanism in laser desorption ionization of individual nanoparticles. J Am Soc Mass Spectrom. 2008;19(3):389–99. https://doi.org/10.1016/j.jasms.2007.11.017.
40. Kane DB, Wang J, Frost K, Johnston MV. Detection of negative ions from individual ultrafine particles. Anal Chem. 2002;74(9):2092–6. https://doi.org/10.1021/ac011126x.
41. Dashtiev M, Wäfler E, Röhling U, Gorshkov M, Hillenkamp F, Zenobi R. Positive and negative analyte ion yield in matrix-assisted laser desorption/ionization. Int J Mass Spectrom. 2007;268(2–3):122–30. https://doi.org/10.1016/j.ijms.2007.07.001.
42. Zhong Q, Shen H, Yun X, Chen Y, Ren Y, Xu H, Shen G, Du W, Meng J, Li W, Ma J, Tao S. Global sulfur dioxide emissions and the driving forces. Environ Sci Technol. 2020;54(11):6508–17. https://doi.org/10.1021/acs.est.9b07696.
43. van der A RJ, Mijling B, Ding J, Koukouli ME, Liu F, Li Q, Mao H, Theys N. Cleaning up the air: effectiveness of air quality policy for SO 2 and NO x emissions in China. Atmos Chem Phys. 2017;17(3):1775–89. https://doi.org/10.5194/acp-17-1775-2017.
44. DeWitt HL, Hellebust S, Temime-Roussel B, Ravier S, Polo L, Jacob V, Buisson C, Charron A, André M, Pasquier A, Besombes JL, Jaffrezo JL, Wortham H, Marchand N. Near-highway aerosol and gas-phase measurements in a high-diesel environment. Atmos Chem Phys. 2015;15(8):4373–87. https://doi.org/10.5194/acp-15-4373-2015.
45. Dall'Osto M, Beddows DCS, McGillicuddy EJ, Esser-Gietl JK, Harrison RM, Wenger JC. On the simultaneous deployment of two single-particle mass spectrometers at an urban background and a roadside site during SAPUSS. Atmos Chem Phys. 2016;16(15):9693–710. https://doi.org/10.5194/acp-16-9693-2016.
46. He L-Y, Huang X-F, Xue L, Hu M, Lin Y, Zheng J, Zhang R, Zhang Y-H. Submicron aerosol analysis and organic source apportionment in an urban atmosphere in Pearl River Delta of China using high-resolution aerosol mass spectrometry. J Geophys Res. 2011;116(D12). https://doi.org/10.1029/2010JD014566.
47. Rivellini L-H, Adam MG, Kasthuriarachchi N, Lee AKY. Characterization of carbonaceous aerosols in Singapore: insight from black carbon fragments and trace metal ions detected by a soot particle aerosol mass spectrometer. Atmos Chem Phys. 2020;20(10):5977–93. https://doi.org/10.5194/acp-20-5977-2020.
48. Wang K, Huang R-J, Brüggemann M, Zhang Y, Yang L, Ni H, Guo J, Wang M, Han J, Bilde M, Glasius M, Hoffmann T. Urban organic aerosol composition in Eastern China differs from North to South: molecular insight from a liquid chromatography-Orbitrap mass spectrometry study. Atmos Chem Phys. 2021;21:9089–104.
49. Zuth C, Vogel AL, Ockenfeld S, Huesmann R, Hoffmann T. Ultrahigh-resolution mass spectrometry in real time: atmospheric pressure chemical ionization orbitrap mass spectrometry of atmospheric organic aerosol. Anal Chem. 2018;90(15):8816–23. https://doi.org/10.1021/acs.analchem.8b00671.
50. Gittins CM, Castaldi MJ, Senkan SM, Rohlfing EA. Real-time quantitative analysis of combustion-generated polycyclic aromatic hydrocarbons by resonance-enhanced multiphoton ionization time-of-flight mass spectrometry. Anal Chem. 1997;69(3):286–93. https://doi.org/10.1021/ac960969z.
51. Eagar JD, Ervens B, Herckes P. Impact of partitioning and oxidative processing of PAH in fogs and clouds on atmospheric lifetimes of PAH. Atmos Environ. 2017;160:132–41. https://doi.org/10.1016/j.atmosenv.2017.04.016.

52. National Research Council (US) Committee on pyrene and selected analogues. Atmospheric transformations of polycyclic aromatic hydrocarbons. In: Analogues, national research council committee on pyrene and selected (Hg.) 1983 – polycyclic aromatic hydrocarbons. https://doi.org/10.5194/acp-21-9089-2021.
53. Keyte IJ, Harrison RM, Lammel G. Chemical reactivity and long-range transport potential of polycyclic aromatic hydrocarbons–a review. Chem Soc Rev. 2013;42(24):9333–91. https://doi.org/10.1039/c3cs60147a.
54. Koeber R, Bayona JM, Niessner R. Determination of benzo[a] pyrene diones in air particulate matter with liquid chromatography mass spectrometry. Environ Sci Technol. 1999;33(10):1552–8. https://doi.org/10.1021/es9805627.
55. Shrivastava M, Lou S, Zelenyuk A, Easter RC, Corley RA, Thrall BD, Rasch PJ, Fast JD, Massey Simonich SL, Shen H, Tao S. Global long-range transport and lung cancer risk from polycyclic aromatic hydrocarbons shielded by coatings of organic aerosol. Proc Natl Acad Sci U S A. 2017;114(6):1246–51. https://doi.org/10.1073/pnas.1618475114.
56. Laskin J, Laskin A, Roach PJ, Slysz GW, Anderson GA, Nizkorodov SA, Bones DL, Nguyen LQ. High-resolution desorption electrospray ionization mass spectrometry for chemical characterization of organic aerosols. Anal Chem. 2010;82(5):2048–58. https://doi.org/10.1021/ac902801f.
57. Roach PJ, Laskin J, Laskin A. Molecular characterization of organic aerosols using nanospray-desorption/electrospray ionization-mass spectrometry. Anal Chem. 2010;82(19):7979–86. https://doi.org/10.1021/ac101449p.
58. Lv Y, Li X, Xu TT, Cheng TT, Yang X, Chen JM, Iinuma Y, Herrmann H. Size distributions of polycyclic aromatic hydrocarbons in urban atmosphere: sorption mechanism and source contributions to respiratory deposition. Atmos Chem Phys. 2016;16(5):2971–83. https://doi.org/10.5194/acp-16-2971-2016.
59. Sheu H-L, Lee W-J, Lin SJ, Fang G-C, Chang H-C, You W-C. Particle-bound PAH content in ambient air. Environ Pollut. 1997;96(3):369–82. https://doi.org/10.1016/S0269-7491(97)00044-4.
60. Qin YM, Tan HB, Li YJ, Schurman MI, Li F, Canonaco F, Prévôt ASH, Chan CK. Impacts of traffic emissions on atmospheric particulate nitrate and organics at a downwind site on the periphery of Guangzhou, China. Atmos Chem Phys. 2017;17(17):10245–58. https://doi.org/10.5194/acp-17-10245-2017.
61. Fan M-Y, Zhang Y-L, Lin Y-C, Cao F, Zhao Z-Y, Sun Y, Qiu Y, Fu P, Wang Y. Changes of emission sources to nitrate aerosols in Beijing after the clean air actions: Evidence from dual isotope compositions. J Geophys Res. 2020;125(12). https://doi.org/10.1029/2019JD031998
62. Squizzato S, Masiol M, Brunelli A, Pistollato S, Tarabotti E, Rampazzo G, Pavoni B. Factors determining the formation of secondary inorganic aerosol: a case study in the Po Valley (Italy). Atmos Chem Phys. 2013;13(4):1927–39. https://doi.org/10.5194/acp-13-1927-2013.
63 Chou CC-K, Lee CT, Yuan CS, Hsu WC, Lin C-Y, Hsu S-C, Liu SC. Implications of the chemical transformation of Asian outflow aerosols for the long-range transport of inorganic nitrogen species. Atmos Environ. 2008;42(32):7508–19. https://doi.org/10.1016/j.atmosenv.2008.05.049.
64. Wang H-C, John W. Characteristics of the Berner impactor for sampling inorganic ions. Aerosol Sci Technol. 1988;8(2):157–72. https://doi.org/10.1080/02786828808959179.
65. Appel BR, Tokiwa Y. Atmospheric particulate nitrate sampling errors due to reactions with particulate and gaseous strong acids. Atmos Environ (1967). 1981;15(6):1087–9. https://doi.org/10.1016/0004-6981(81)90110-4.
66. Haque MM, Kawamura K, Deshmukh DK, Fang C, Song W, Mengying B, Zhang Y-L. Characterization of organic aerosols from a Chinese megacity during winter: predominance of fossil fuel combustion. Atmos Chem Phys. 2019;19(7):5147–64. https://doi.org/10.5194/acp-19-5147-2019.
67. Baxter LL, Mitchell RE, Fletcher TH, Hurt RH. Nitrogen release during coal combustion. Energy Fuels. 1996;10(1):188–96. https://doi.org/10.1021/ef9500797.
68. Forehand J, Dooly G, Moldoveanu S. Analysis of polycyclic aromatic hydrocarbons, phenols and aromatic amines in particulate phase cigarette smoke using simultaneous distillation and extraction as a sole sample clean-up step. J Chromatogr A. 2000;898(1):111–24. https://doi.org/10.1016/S0021-9673(00)00827-X.
69. Tobiszewski M, Namieśnik J. PAH diagnostic ratios for the identification of pollution emission sources. Environ Pollut. 2012;162:110–9. https://doi.org/10.1016/j.envpol.2011.10.025.
70. Tormyshev VM, Kur SY, Koptyug VA. Formation of c9h7 + ions in the mass spectra of 2-methyl-, 2-chloromethyl-, and 2-hydroxymethylnaphthalenes. Russ Chem Bull. 1977;26(5):968–72. https://doi.org/10.1007/BF01152695.
71 Onishi K, Otani S, Yoshida A, Mu H, Kurozawa Y. Adverse health effects of Asian dust particles and heavy metals in Japan. Asia Pac J Public Health. 2015;27(2):NP1719-26. https://doi.org/10.1177/1010539511428667.
72. Jaishankar M, Tseten T, Anbalagan N, Mathew BB, Beeregowda KN. Toxicity, mechanism and health effects of some heavy metals. Interdiscip Toxicol. 2014;7(2):60–72. https://doi.org/10.2478/intox-2014-0009.
73. Yu J, Cocker DR III, Griffin RJ, Flagan RC, Seinfeld JH. Gas-phase ozone oxidation of monoterpenes: gaseous and particulate products. J Atmos Chem. 1999;34(2):207–58. https://doi.org/10.1023/A:1006254930583.
74. Larsen BR, Di Bella D, Glasius M, Winterhalter R, Jensen NR, Hjorth J. Gas-phase OH oxidation of monoterpenes: gaseous and particulate products. J Atmos Chem. 2001;38(3):231–76. https://doi.org/10.1023/A:1006487530903.
75. Meng J, Wang G, Li J, Cheng C, Ren Y, Huang Y, Cheng Y, Cao J, Zhang T. Seasonal characteristics of oxalic acid and related SOA in the free troposphere of Mt. Hua, central China: implications for sources and formation mechanisms. Sci Total Environ. 2014;493:1088–97. https://doi.org/10.1016/j.scitotenv.2014.04.086.
76. Iinuma Y, Böge O, Gräfe R, Herrmann H. Methyl-nitrocatechols: atmospheric tracer compounds for biomass burning secondary organic aerosols. Environ Sci Technol. 2010;44(22):8453–9. https://doi.org/10.1021/es102938a.
77. Al-Naiema IM, Stone EA. Evaluation of anthropogenic secondary organic aerosol tracers from aromatic hydrocarbons. Atmos Chem Phys. 2017;17(3):2053–65. https://doi.org/10.5194/acp-17-2053-2017.
78. Laskin A, Iedema MJ, Ichkovich A, Graber ER, Taraniuk I, Rudich Y. Direct observation of completely processed calcium carbonate dust particles. Faraday Discuss. 2005;130:453–68. https://doi.org/10.1039/b417366j.
79. Salter ME, Hamacher-Barth E, Leck C, Werner J, Johnson CM, Riipinen I, Nilsson ED, Zieger P. Calcium enrichment in sea spray aerosol particles. Geophys Res Lett. 2016;43(15):8277–85. https://doi.org/10.1002/2016GL070275.
80 Cheng Y, Li S-M, Leithead A. Chemical characteristics and origins of nitrogen-containing organic compounds in PM2.5 aerosols in the Lower Fraser Valley. Environ Sci Technol. 2006;40(19):5846–52. https://doi.org/10.1021/es0603857.
81. Weber S, Hoffmann P, Ensling J, Dedik AN, Weinbruch S, Miehe G, Gütlich P, Ortner HM. Characterization of iron compounds from urban and rural aerosol sources. J Aerosol Sci. 2000;31(8):987–97. https://doi.org/10.1016/S0021-8502(99)00564-9.
82. Russell LM, Bahadur R, Hawkins LN, Allan J, Baumgardner D, Quinn PK, Bates TS. Organic aerosol characterization by complementary measurements of chemical bonds and molecular

fragments. Atmos Environ. 2009;43(38):6100–5. https://doi.org/10.1016/j.atmosenv.2009.09.036.
83. Mohr C, Huffman A, Cubison MJ, Aiken AC, Docherty KS, Kimmel JR, Ulbrich IM, Hannigan M, Jimenez JL. Characterization of primary organic aerosol emissions from meat cooking, trash burning, and motor vehicles with high-resolution aerosol mass spectrometry and comparison with ambient and chamber observations. Environ Sci Technol. 2009;43(7):2443–9. https://doi.org/10.1021/es8011518.
84. Zhigilei LV, Garrison BJ. Computer simulation study of damage and ablation of submicron particles from short-pulse laser irradiation. Appl Surf Sci. 1998;127–129:142–50. https://doi.org/10.1016/S0169-4332(97)00624-7.
85. Sonnefeld WJ, Zoller WH, May WE. Dynamic coupled-column liquid-chromatographic determination of ambient-temperature vapor pressures of polynuclear aromatic hydrocarbons. Anal Chem. 1983;55(2):275–80. https://doi.org/10.1021/ac00253a022.
86. Hoyer H, Peperle W. Dampfdruckmessungen an organischen Substanzen und ihre Sublimationswärmen. Z Elektrochem Ber Bunsenges Phys Chem. 1958;62(1):61–6. https://doi.org/10.1002/bbpc.19580620109.
87. Li M, Chen H, Wang B-F, Yang X, Lian J-J, Chen J-M. Direct quantification of PAHs in biomass burning aerosols by desorption electrospray ionization mass spectrometry. Int J Mass Spectrom. 2009;281(1–2):31–6. https://doi.org/10.1016/j.ijms.2008.11.013.
88. Elzein A, Dunmore RE, Ward MW, Hamilton JF, Lewis AC. Variability of polycyclic aromatic hydrocarbons and their oxidative derivatives in wintertime Beijing, China. Atmos Chem Phys. 2019;19(13):8741–58. https://doi.org/10.5194/acp-19-8741-2019.
89. Carré V, Vernex-Loset L, Krier G, Manuelli P, Muller J-F. Laser desorption/ionization mass spectrometry of diesel particulate matter with charge-transfer complexes. Anal Chem. 2004;76(14):3979–87. https://doi.org/10.1021/ac049875c.
90. Holme JA, Brinchmann BC, Refsnes M, Låg M, Øvrevik J. Potential role of polycyclic aromatic hydrocarbons as mediators of cardiovascular effects from combustion particles. Environ Health. 2019;18(1):74. https://doi.org/10.1186/s12940-019-0514-2.

Danksagung

Diese Arbeit wäre ohne die Unterstützung und das Engagement vieler Menschen nicht möglich gewesen. Ich möchte diese Gelegenheit nutzen, um meinen Dank an alle auszudrücken, die zu ihrem Erfolg beigetragen haben. Zunächst gilt mein Dank meinem Betreuer Prof. Dr. Bernhard Spengler, der mir während des gesamten Prozesses mit Rat, Tat als auch finanziell zur Seite stand. Seine Expertise und sein Enthusiasmus haben mich stets motiviert und inspiriert. Ich danke auch meinen Kommilitonen und den Kollegen aus dem Institut für analytische Chemie für die angenehme Atmosphäre und die wertvollen Diskussionen. Die Zusammenarbeit mit euch hat mir sehr viel Spaß gemacht und meine Arbeit bereichert. Ein besonderer Dank gilt meinen Freunden und meiner Familie, die mich in schwierigen Zeiten unterstützt und mir immer wieder Mut gemacht haben. Eure Freundschaft und euer Zuspruch sind mir sehr wichtig. Ich möchte auch allen Förderern danken, die meine Forschung finanziell unterstützt haben. Ohne ihre Hilfe wäre diese Arbeit nicht möglich gewesen. Zu guter Letzt danke ich allen, die ich hier nicht namentlich erwähnt habe, aber die dennoch einen Beitrag zu meiner Dissertation geleistet haben. Eure Unterstützung und euer Interesse an meiner Arbeit haben mich sehr gefreut.

Vielen Dank euch allen!